

A Review of Inorganic Photoelectrode Developments and Reactor Scale-Up Challenges for Solar Hydrogen Production

Benjamin Moss, Oytun Babacan, Andreas Kafizas, and Anna Hankin*

Green hydrogen, produced using solar energy, is a promising means of reducing greenhouse gas emissions. Photoelectrochemical (PEC) water splitting devices can produce hydrogen using sunlight and integrate the distinct functions of photovoltaics and electrolyzers in a single device. There is flexibility in the degree of integration between these electrical and chemical energy generating components, and so a plethora of archetypal PEC device designs has emerged. Although some materials have effectively been ruled out for use in commercial PEC devices, many principles of material design and synthesis have been learned. Here, the fundamental requirements of PEC materials, the top performances of the most widely studied inorganic photoelectrode materials, and reactor structures reported for unassisted solar water splitting are revisited. The main phenomena limiting the performance of up-scaled PEC devices are discussed, showing that engineering must be considered in parallel with material development for the future piloting of PEC water splitting systems. To establish the future commercial viability of this technology, more accurate techno-economic analyses should be carried out using data from larger scale demonstrations, and hence more durable and efficient PEC systems need to be developed that meet the challenges imposed from both material and engineering perspectives.

1. Introduction

The excessive use of fossil fuels and accompanying release of carbon dioxide (CO_2) and other greenhouse gases into the atmosphere has resulted in global warming.^[1,2] Since 1880, the CO_2 concentration in the atmosphere has risen from ≈ 290 to

above 410 ppm, resulting in a global temperature increase of at least $1\text{ }^\circ\text{C}$.^[1] To put this into context, the last time CO_2 levels were this high was during the Pliocene epoch. This was around 3 million years ago, when the Earth had a very different climate, with sea levels almost 15 m higher than they are today and forestry present in the Arctic and Antarctic.^[2,3] To prevent the dramatic and potentially catastrophic impacts of climate change, the Intergovernmental Panel on Climate Change had set the target of restricting global warming to $2\text{ }^\circ\text{C}$ above preindustrial revolution temperatures, which was signed by 195 countries in the landmark Paris Agreement. Importantly, to restrict any level of warming requires a global transition to net-zero CO_2 emissions.^[4] Such a transition can only be achieved if new technologies are implemented in a number of sectors – including electrical power generation, transportation and heating – that exploit carbon-neutral and ideally, renewable sources of energy. Yet, given the intermittency of renewables, there is a need to

develop energy storage carriers that can be coupled to renewables, and one such highly promising carrier is hydrogen.^[5]

A growing body of evidence shows that hydrogen can play a major role alongside electricity in the future low-carbon world. A review of hydrogen pathways in global energy models reveals that hydrogen is capable of delivering emission reductions in

Dr. B. Moss, Dr. A. Kafizas
Department of Chemistry
Imperial College London
Molecular Sciences Research Hub
White City Campus, London W12 0BZ, UK

Dr. O. Babacan
Department of Physics
Imperial College London
South Kensington Campus, London SW7 2AZ, UK

Dr. O. Babacan, Dr. A. Kafizas
Grantham Institute
Imperial College London
South Kensington Campus, London SW7 2AZ, UK

Dr. A. Kafizas
London Centre for Nanotechnology
Imperial College London
London SW7 2AZ, UK

Dr. A. Hankin
Department of Chemical Engineering
Imperial College London
South Kensington Campus, London SW7 2AZ, UK
E-mail: anna.hankin@imperial.ac.uk

Dr. A. Hankin
Institute for Molecular Science and Engineering
South Kensington Campus
Imperial College London
London SW7 2AZ, UK

 The ORCID identification number(s) for the author(s) of this article can be found under <https://doi.org/10.1002/aenm.202003286>.

DOI: 10.1002/aenm.202003286

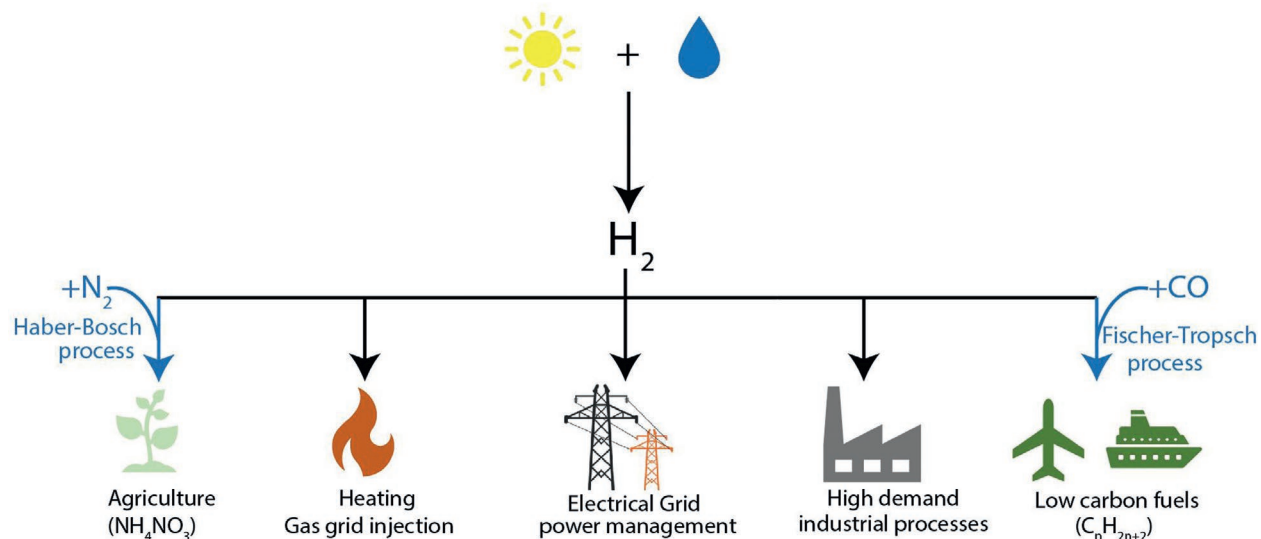


Figure 1. Potential uses of hydrogen produced by solar-powered water splitting, including agriculture (when reacted with N_2 to produce NH_3), heating, power management (as an energy storage medium), industrial processes (such as steel production), and the renewable production of fuels for freight (when reacted with CO to produce hydrocarbons).

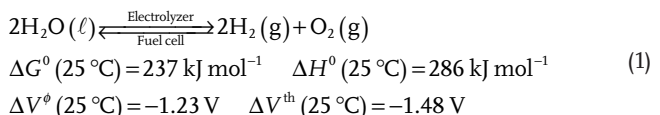
various sectors and enabling a deeper decarbonization.^[6] It has also been argued that without the production and utilization of hydrogen at large scale, European Union (EU) nations cannot meet their decarbonization objectives.^[7] The results from the JRC-EU-TIMES model, a bottom-up model of the EU28 energy system, indicate that hydrogen and its related technologies could become a viable option as early as 2030 with policy support.^[8] The European Commission has recently released the first-ever hydrogen strategy that could support building hydrogen infrastructure in the coming decades.^[9–11] Currently, however, hydrogen is produced primarily using natural gas, oil, and coal^[12,13] with ~96% of the world's hydrogen produced by steam reformation which carries a large carbon footprint (~6 kg of CO_2 released per kg of hydrogen produced).^[14] The resulting emissions exceed 0.83 Gt of CO_2 per year, which accounts for more than 2% of global emissions.^[15] Thus, in order to limit the rise in global temperature, carbon-neutral methods for producing hydrogen must be developed.

Figure 1 provides a schematic summary of the many uses of hydrogen, including transport, heat, industry, and electricity sectors.^[9] While the electricity sector has been the main focus in decarbonization efforts to date, there are sectors that are not as easy to decarbonize, such as heating, and long-distance and heavy-duty transport.^[10] For heating, there are ongoing trials showing that low-carbon hydrogen can be successfully blended into the gas supply.^[11] In some applications, hydrogen is also envisaged as a direct replacement of natural gas, and has featured prominently in recent transition pathways for the decarbonization of heat across sectors.^[12] In transportation, there are several companies currently designing and manufacturing long-range commercial trucks powered by hydrogen.^[13] There are also ongoing demonstrations like H2-Share for hydrogen trucks in retail logistics to provide last mile delivery solutions.^[16] Finally, hydrogen is essential in the production of certain chemicals and fuels, as well as being a fuel in its own right.^[17] If solar energy could be harvested and stored in

hydrogen – in a cost-effective manner – this hydrogen could then be transported and used on demand and enable a secure and flexible energy system without fossil fuel dependence. One possible mechanism of converting solar energy into hydrogen is by solar water splitting, as shown in Figure 1.

1.1. Hydrogen Production by Water Electrolysis

Hydrogen production by water electrolysis has no direct CO_2 emissions associated with it. The same is true for the reverse process, where hydrogen is reacted to generate electrical energy in fuel cells or combusted for heat generation. Equation (1) appears beautifully simple and the use of hydrogen as a fuel is most attractive, especially when we imagine moving vehicles expelling water without the usual accompaniment of fumes comprising carbon monoxide, nitrogen oxides, sulfur oxides, benzene, CO_2 , and other unsavory compounds



However, water electrolysis fundamentally requires a significant electrical energy input and this input becomes yet larger for practical up-scaled devices, which operate at >1.65 V with liquid water.^[18–20] Hence, optimization of electrolyzer materials and engineering designs are the subjects of ongoing research, and are leading to gradual decreases in the specific electrical energy consumptions and costs in all types of water electrolyzers.^[21,22] The source of electrical energy for powering electrolysis ultimately impacts on both the cost of hydrogen production and the net CO_2 emissions associated with it.^[23,24]

In all commercial electrolyzers, hydrogen and oxygen are evolved on two physically separated electrodes: the cathode and

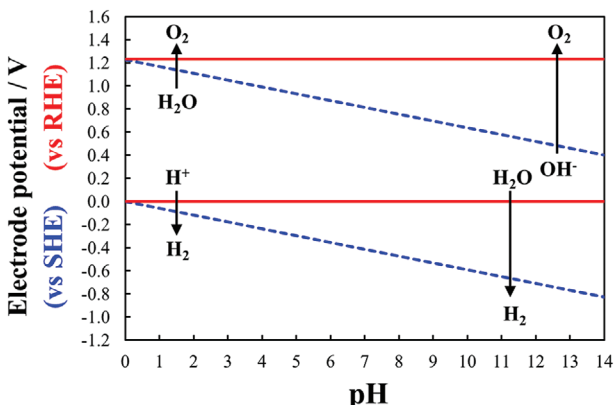


Figure 2. Pourbaix diagram of the water splitting half reactions under standard conditions, generated using thermodynamic data in ref. [30]. SHE is the standard hydrogen electrode and RHE is the reversible hydrogen electrode.

the anode. **Figure 2** shows the Pourbaix diagram for these half reactions under standard conditions ($25\text{ }^{\circ}\text{C}$ and atmospheric pressure). This diagram is helpful for visualizing why **cathodic hydrogen production is more thermodynamically favorable at lower pH while anodic oxygen production is thermodynamically favorable under alkaline conditions**, and yet at any pH the minimum cell potential difference remains 1.23 V. Both acidic and alkaline regimes are being employed practically, but have their respective trade-offs.

The higher electron stoichiometry of water oxidation (4e^-), compared with reduction (2e^-), results in a higher overall activation barrier and renders oxygen evolution the kinetically limiting half reaction.^[25] This limitation has historically been partially compensated by adopting alkaline conditions, leading to the alkaline water electrolysis being the most mature of all electrolyzer technologies.^[26]

The electrolyte pH dictates the suitability of various materials for use as catalysts, catalyst supports, ion permeable membranes, or microporous separators and various other components that are exposed to the electrolyte under either oxidizing or reducing conditions. Acidic environments promote corrosion of catalysts that are based on reasonably cheap transition metals such as nickel, iron, and copper; Pourbaix diagrams of these metals in an aqueous environment show why this is the case.^[27] To a significant degree, the stability of many materials can be predicted from their Pourbaix diagrams, though these often exclude vital compounds and do not provide kinetic information; poor kinetics have often been found to overcome thermodynamically predicted instabilities. For example, although nickel is predicted to decompose at anodic potentials in alkaline solutions, this process is sufficiently slow to enable the use of nickel and its alloys as anodes, as well as cathodes, in alkaline electrolysis.^[28,29] Noble metals from the platinum group are resistant to corrosion in acidic solutions and platinum and iridium/ruthenium oxide in particular have demonstrated excellent catalytic properties for water splitting in polymer electrolyte membrane (PEM) electrolyzers.

The unsurpassed catalytic properties of platinum have led to it being the sole, “archetypal” proton reduction catalyst used in commercial PEM electrolyzers, but this has naturally led

to concerns not only regarding cost but also about it lacking Earth abundance for supporting a hydrogen economy, the latter point being met with counterarguments.^[31,32] Exchange current densities, which determine the kinetics of electrochemical reactions, can be found in the literature for a wealth of materials and conditions.^[33–35] Besides the intrinsic properties of the catalysts, their mechanical properties, geometry, and micro- as well as macrostructure play an integral role in the overall performance and stability of water electrolyzers.

The component around which electrolyzer engineering designs have been based is the gas separator. It is the development of this separator that has led to the original alkaline and more recent PEM designs to be different. The role of the separator is vital since all commercial liquid water electrolyzers operate at high current densities, typically above 200 mA cm^{-2} , generating a froth of buoyant bubbles. Without a gas separator, the oxygen and hydrogen will recombine explosively, the obvious drawbacks of which are the safety hazard, loss of valuable H_2 product, and damage to the reactor. Furthermore, without separation, bubbles of each gas will cross over to the opposing electrode and will be partially consumed in a reverse reaction, leading to loss of product and overall process efficiency. Original gas separators were microporous structures and are referred to in the literature as diaphragms.^[18,36] Microporous separators provide a physical barrier to bubbles, but do not impede the flow of ions or solution supersaturated with dissolved gases. Hence, in electrolyzers using such separators, the electrodes are physically distanced from the membrane by a flow channel, through which reactant flows and through which the generated bubbles are removed, as shown in **Figure 3a**. The size of the electrode-to-membrane separation is critically important as its increase leads to increased Ohmic losses via the electrolyte but, on the other hand, excessive narrowness will promote the buildup of bubbles and result in even greater Ohmic losses as well as nonuniformities in reaction rate along the electrode length.^[37,38] The optimum spacing is a function of the operating current density.^[39]

The development of cation permeable membranes has enabled more effective separation of gases, as well as control over

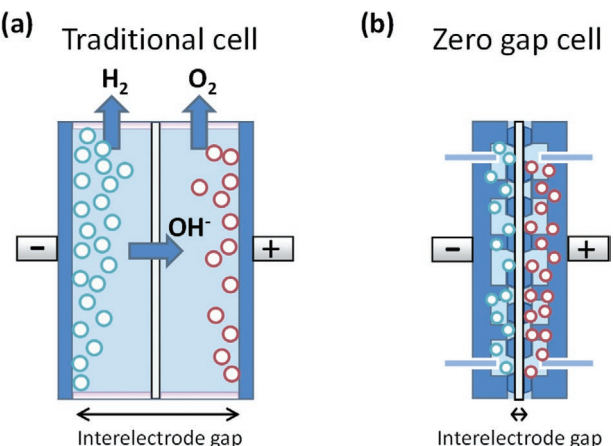


Figure 3. Electrode and membrane arrangements in a) traditional alkaline electrolyzer and b) a membrane electrode assembly (also known as the zero gap cell). Reproduced with permission.^[40] Copyright 2016, Royal Society of Chemistry.

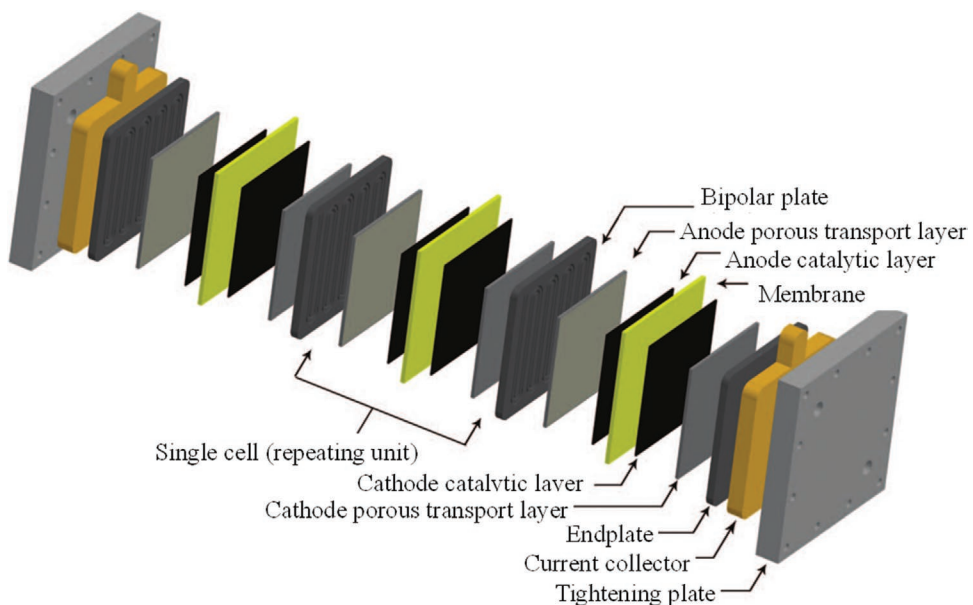


Figure 4. Schematic representation of a three-cell PEM electrolyzer stack with the main components. Reproduced with permission.^[20] Copyright 2020, The Royal Society of Chemistry.

ion crossover, and has opened up the possibility of using the membrane electrode assemblies (MEAs) now deployed in PEM, where the catalysts are in direct contact with the membrane.^[20] Figure 3b shows this arrangement, in which Ohmic losses due to electrolyte conductivity and bubble buildup are decreased relative to the arrangement in label (a); furthermore these systems are able to operate using only deionized water that needs to be supplied to the anode side alone. However, besides requiring platinum group metal catalysts, these systems are also not immune to losses. During operation, the water has to percolate through a porous layer to the boundary between the membrane and the catalyst, where the electrochemical reaction takes place; the exiting fluid is a multiphase flow comprising water and the gaseous product. Effects of mass transport, namely the distribution of fluids and different behavior of bubbles as a function of position in the reactor still have a profound impact on PEM performance and affect the scale-up of PEM cells in a stack.^[41–43]

The relatively recent development of anion exchange membranes (AEMs) has opened up a possibility of using MEAs for

alkaline electrolysis. Alas, while PEMs operate successfully with deionized water as the reactant, AEMs tend to require the addition of caustic soda or potash to the electrolyte due to insufficient membrane conductivity.^[44,45] The ambition with AEM-based electrolyzers is for their performance to match those of PEM, but with decreased capital cost; however, significant improvements to the conductivity and stability of the membranes are still required.^[46–48]

Modern alkaline and PEM electrolyzers are very compact devices, mostly operated in a bipolar arrangement, which is shown schematically in Figures 4 and 5. Their structure and appearance, as well as the arrangement of the complete unit, of which examples are shown in Figure 6, bear no resemblance to textbook depictions of pieces of metal freely dipped into a water bath. The purpose of their compactness is to minimize Ohmic losses, enable internal pressurization (which reduces requirements for H₂ compression post electrolysis), and to decrease

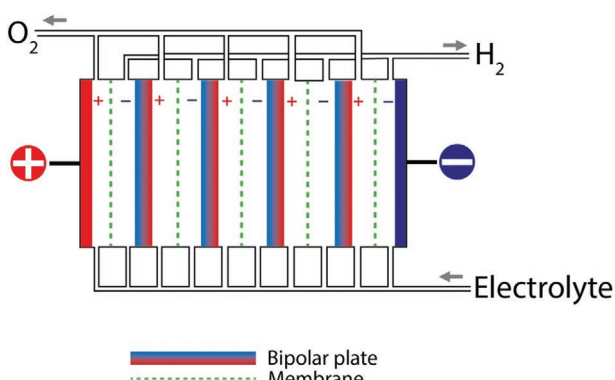


Figure 5. Operating principle of a bipolar electrolyzer stack and its main components.

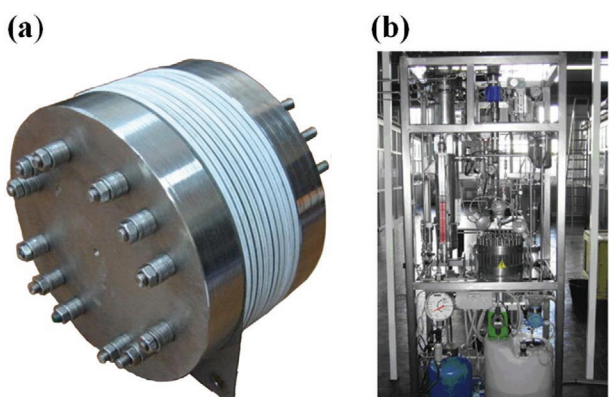


Figure 6. Photographic images of a) 10 cell PEM stack and b) electrolyzer system unit. (a) Reproduced with permission.^[49] Copyright 2008, Elsevier Ltd.; (b) Reproduced with permission.^[50] Copyright 2011, Elsevier Ltd.

the device footprint. In the bipolar arrangement, only two end plate electrodes are connected to the DC power supply. Metal plates provide series connection between adjacent electrolysis cells and each metal plate becomes polarized during operation, acting as a cathode and anode feeder plate on each of its sides (hence bipolar). Current flows through the electrolyte, connecting the electronic components.

The size of the electrodes and their electroactive areas varies significantly between systems, depending on their output hydrogen flow rate. Reviews report that electrode dimensions in alkaline and PEM electrolyzers are limited to <4 and $<3\text{ m}^2$, respectively.^[44] As electrodes are typically either circular or square in shape, it follows that 4 m^2 corresponds to either $2\text{ m} \times 2\text{ m}$ for square, or 2.3 m diameter for circular electrodes. However, these upper limit dimensions appear atypically large. For example, a compendium on the characteristics of several commercial PEM electrolyzers,^[19] reports: i) $\approx 4.5\text{ kg h}^{-1}\text{ H}_2$ production system with 250 kW input system, utilizing a stack of 100 cells with an active electrode area of 680 cm^2 ($\approx 0.26\text{ m} \times 0.26\text{ m}$) and ii) $\approx 4.2\text{ kg h}^{-1}\text{ H}_2$ production system with 225 kW input, utilizing a stack of 140 cells with an active electrode area of 450 cm^2 ($\approx 0.21\text{ m} \times 0.21\text{ m}$). The tanks of passenger hydrogen fuel cell vehicles (FCEVs) typically hold $2.5\text{--}6\text{ kg}$ of H_2 , so 250 kW electrolyzers with small electrodes would support a small refuelling station.

Electrolyzer installation is accompanied by a balance of plant (BoP), which includes all the necessary auxiliary components. The electrolyzer cell stacks typically contribute 50–60% of the overall system cost, depending on the type of electrolyzer.^[24] The auxiliary components are arranged in close proximity to the electrolyzer in a manner that minimizes the system footprint, as can be seen from Figure 6b.

The BoP includes: 1) a water purification unit – a prerequisite for maintenance of long-term electrolyzer efficiency, 2) a water circulation unit, 3) heat exchanger (not always), 4) gas–liquid separators, 5) gas conditioning unit, 6) the necessary power electronics to balance loads, 7) process monitoring unit – for continuous operation and automated monitoring, and 8) pumps to prevent the system from freezing while not being operated and also to enable a short start-up time.^[19] The energy consumption of the water purification unit depends on the quality of water supply, which determines the optimum deionization mechanism, but it cannot be neglected as electrolyzers typically require the order of 10 kg of H_2O to make 1 kg of H_2 .^[51] Pressurized operation is often preferred when hydrogen is required at high pressure (e.g., for FCEV refueling), as it can reduce or eliminate the cost of an external compressor and the auxiliary components associated with it.^[24] However, modeling work suggests that operation at atmospheric pressure is certainly viable as parasitic energy consumption and loss of gaseous products is lower compared to pressurized operation.^[52]

For hydrogen produced by water electrolysis to be truly green, the electricity powering these systems must be generated with minimum associated $\text{kg}(\text{CO}_2)\text{ kWh}^{-1}$. Hence, a sensible way forward is to couple electrolyzers to electricity generators powered by renewable energy. One of the most promising solutions to address this issue is to store solar energy in the form of hydrogen^[53] via solar water splitting.^[54]

1.2. Considerations for Photovoltaic (PV) Installations: Lessons for Future Development of Solar-Powered (Photo)Electrolyzers

The primary purpose of photovoltaic installations is the harvesting of solar energy and its conversion to electricity that could then either be injected into a grid, used locally off-grid, or converted into another form of energy for storage. Sunlight is our largest energy source, ceaselessly providing $\approx 120\,000\text{ TW}$ of power to the Earth.^[55] If we compare this with total global power consumption of $\approx 18.1\text{ TW}$ in 2019,^[56] there is enough power in $\approx 1\frac{1}{2}\text{ h}$ of sunlight to meet current demands for an entire year. Consequently, photovoltaics is the fastest growing renewable technology,^[57] and will have a huge role in decarbonizing future economies.^[58]

The solar irradiance just outside the Earth's atmosphere (air mass AM 0) is on average 1370 W m^{-2} , varying by $\pm 50\text{ W m}^{-2}$ through the year due to the ellipticity of the Earth's orbit. Radiation undergoes absorption and scatter in the atmosphere and only a fraction reaches ground level. AM 1.0 is the irradiance at ground level when the light takes the shortest path through the Earth's air mass, which happens at a solar elevation of 90° , when the sun is directly overhead; AM 1.5 corresponds to an elevation angle of 41.8° . Radiation reaching us has two components: direct and diffuse. Diffuse radiation is that which undergoes scatter in the atmosphere, and hence takes an indirect route to the Earth's surface. The two components add up to what is known as "global" radiation.^[59] Both the direct and diffuse components can be predicted geometrically based on the sun's position in the sky, but do not account for cloud cover, which decreases the ratio between direct and diffuse radiation.^[60–62]

Heat management aside, the PV output can be maximized by ensuring that the surface of the PV is normal to the impinging direct light. However, the optimal angle between solar rays and PV panels varies with time on daily and seasonal timescales. The daily variation is related to the elevation of the sun relative to the horizon, as it "moves" from East to West across the sky. Seasonal variation is caused by the declination of the Earth's equatorial plane relative to its orbital plane, meaning that the Southern and Northern hemispheres are closer to the sun at different times of the year. For example, the sketch in Figure 7a shows why in the Northern hemisphere this seasonal variation results in greater elevation angles and more sun hours in the summer, and hence more solar harvesting. Figure 7b confirms that there is no single angle at which any surface, such as that of a PV or any other light gathering device, can be installed so as to harvest the maximal amount of light at all times of year. However, for fixed systems, the angle (relative to the horizon) can be optimized based on the latitude of the installation.^[59,63]

To maximize light harvesting, PV panels can be mounted on axially mobile platforms, which can change position about one or two axes, as shown schematically in Figure 8. It should be noted that the representations in Figure 8b,c somewhat simplify the concept, because trackers can come in many varieties and employ different modes of rotation.^[64,65]

For these systems, the PV energy return follows the order: dual axes > single axis > fixed angle.^[64,66–68] This is because in dual axes systems, the PV panels are positioned normal to the sun's rays for the greatest portion of the day and their inclination is optimized for all times of year. These technological

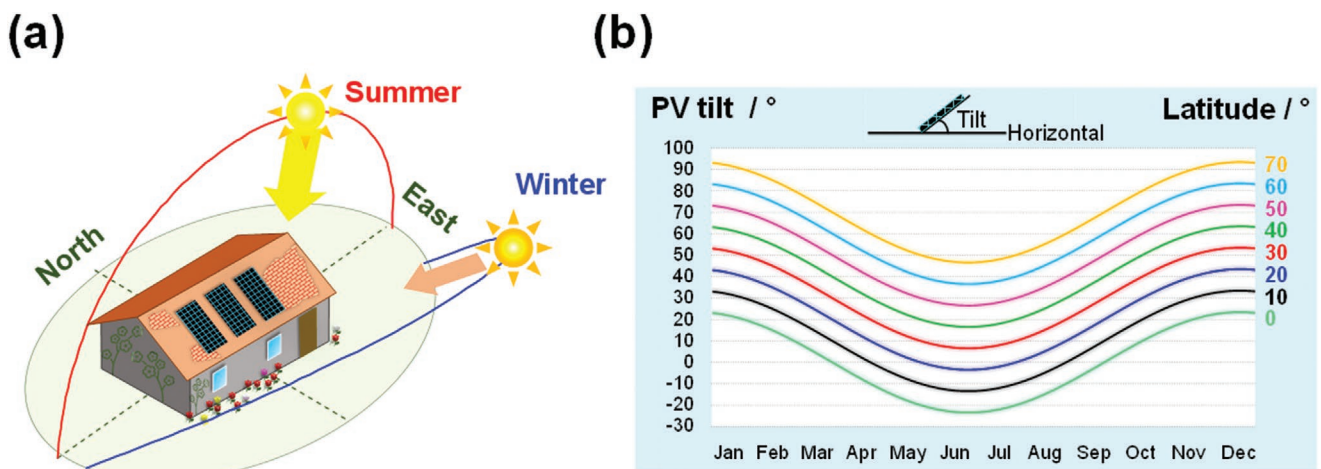


Figure 7. a) Relative difference in the sun's maximum elevation during Summer and Winter in the Northern hemisphere and b) predicted optimum tilt angles for a south facing PV installation, computed relative to the horizon as a function of latitude and the Earth's declination.

solutions are very important because, in spite of the sun being by far the largest source of renewable energy, the energy delivered to the Earth's surface is dilute; even in the hottest regions on the Earth, the available solar radiation flux rarely exceeds 1000 W m^{-2} .^[64] This can be verified via publicly available "solar calculator" and "solar radiation database" tools.^[69–71] Tracking of the Sun's position is generally acknowledged to significantly increase PV efficiency relative to fixed angle PV systems and is particularly beneficial on cloudy days. The reported increases are $\approx 25\%$ for single axis tracking systems and 40% for dual axis tracking systems relative to fixed systems, not accounting for energy losses incurred during operation.^[68] However, it is easily imagined that the more sophisticated the technology, the higher the capital and operating costs, as well as possible routes to system failure. These considerations are deciding factors for the choice of tracking system in any given location.

Solar tracking systems consist of the tracking device, tracking algorithm, control unit, positioning system, driving mechanism,

and sensing devices.^[72] Tracking devices and algorithms have different levels of sophistication and can enable active, passive, semipassive, manual, and chronological tracking. Over 76% of systems employ active tracking; the associated algorithms employ astronomical algorithms and real-time light intensity algorithms. The latter algorithm receives input from two light intensity measuring sensors on the system and adjusts the tracker position until the intensities are equal.^[65,73] Algorithms can also track the maximum power point (MPP) of the PV output and make positioning adjustments to obtain the highest MPP.

In addition to tracking, light collection can be enhanced by coupling a variety of optical components to individual PV cells or PV panels.^[74] Mirrors or lenses collect light over an area that is determined by their size, and concentrate it onto a smaller area; the concentration ratio is the fraction between the areas of the concentrator and the receiver (i.e., the PV). Concentration is particularly useful for reducing the area requirements of expensive

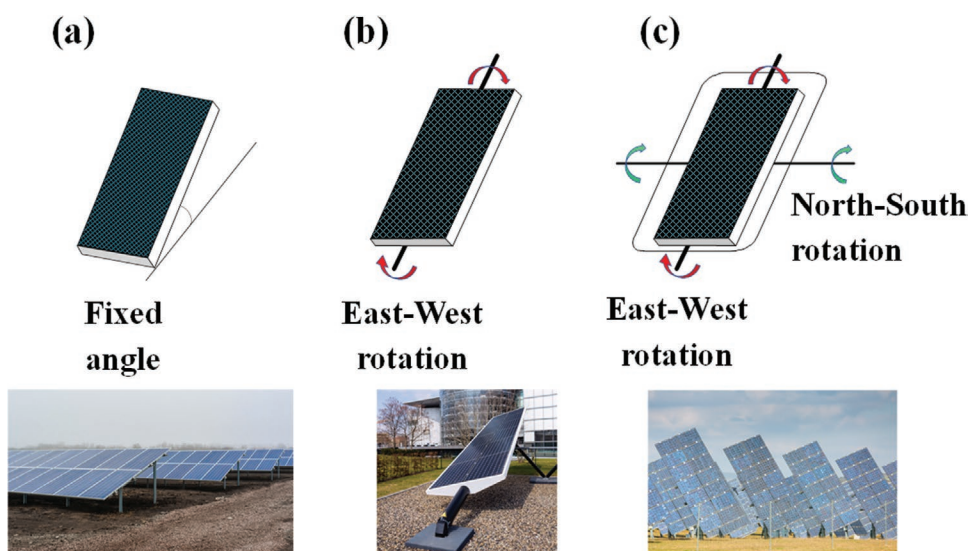


Figure 8. a) Fixed angle PV installation and solar tracking systems with rotational mobility relative to b) one or c) two axes.

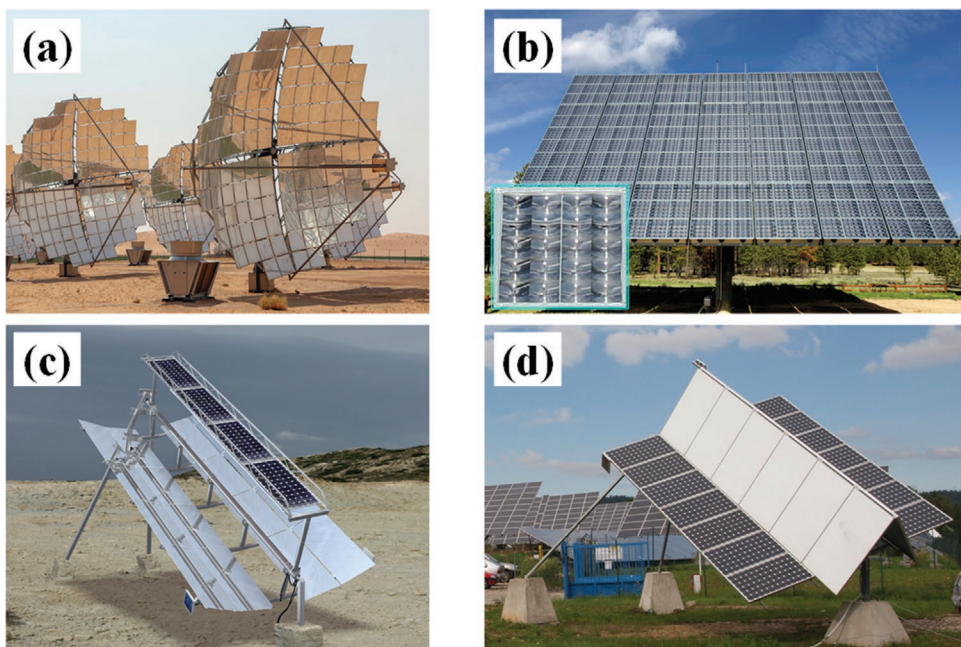


Figure 9. Four of the many varieties of solar concentrators: a) solar dish, b) Fresnel lens, c) pseudoparabolic concentrator, and d) V-trough. Permissions: (c) and (d) photographs courtesy of V. Poulek.

PV materials, such as III–V semiconductors. Some examples of concentrators are shown in **Figure 9**. Figure 9a shows a solar dish, which reflects the incoming light toward a focal point where PV cells are situated; high precision is required in this system and so two-axis tracking systems are used. The average dish diameters are between 5 and 10 m and their surface area ranges between 40 and 120 m², enabling concentration by a factor of up to 3000.^[75] Figure 9b shows modular grids of Fresnel lenses, concentrating light onto underlying solar cells.^[76–78] The lenses may be either flat or domed and can achieve concentration factors of 500 or more. The lenses are able to capture and convert both direct and diffuse light and are able to function with single-axis tracking (especially if linear) but benefit from two-axis tracking. Figure 9c shows a pseudoparabolic concentrator mounted on a single-axis tracking system, capable of concentrating light onto a downward facing PV module by a factor of ≈ 5 , while the upward facing panel receives unconcentrated light. Finally, Figure 9d shows a V-trough design, where one or two planar reflectors are positioned on either side of a PV panel to increase the overall irradiance and power output.^[79] A two mirror system can produce a concentration factor of ≈ 2 , which is higher than what can be achieved with a single mirror (shown in the figure). However, a single mirror installation can operate at a fixed angle and still produce a concentration factor > 1 , whereas the two mirror system always requires a tracker. Hence, a wide variety of optical options are available to suit different photovoltaic installations.

Concentrator photovoltaic (CPV) modules require either passive or active cooling to facilitate the dissipation of heat. If, for example, the PV is 40% efficient, then the majority of the remaining energy is converted to heat. The current output of PVs scales linearly with irradiance, but the build-up of heat tends to eventually compromise this linearity. Different PV materials have their own temperature coefficients, which quantify

the changes in current–voltage output as a function of temperature; colder conditions generally lead to improved performance. Without heat management, PVs may suffer permanent degradation due to excessive temperatures, with silicon solar cells being more susceptible to this than III–V solar cells. The cooling system needs to be chosen and designed appropriately in order to reliably maintain low and uniform cell temperatures, minimize parasitic power consumption, and, where possible, enable the use of extracted thermal heat; the optimum cooling solutions differ between single-cell arrangements and densely packed photovoltaic cells.^[80] Passive cooling involves a heat sink such as a finned metallic plate, made of aluminium or copper, positioned behind the solar cells.^[81] The area of the sink needs to be approximately equal to that of the concentrator. This cooling approach is sufficient for single-cell arrangements, such as with III–V solar cells. Active cooling is necessary for panels of densely packed cells, where heat is removed via a flow of water coolant through geometrically optimized channels.^[80]

The combinations of tracking systems and concentrator optics can complicate the installation of PVs and the net benefit depends on the overall solar energy conversion efficiency (location- and season-dependent), weight, material use, ease of manufacturing and maintenance, maximum heat removal, temperature uniformity, shading, and water pumping power. Undeniably, the highest photon to electrical energy conversions of $> 46\%$ have been achieved under concentrator light.^[82,83]

1.3. Demonstrations of Water Electrolysis Powered by Solar Energy

The feasibility of coupling arrays of photovoltaic modules to water electrolysis units to enable distributed solar hydrogen production has been demonstrated in several projects.^[84–86] A

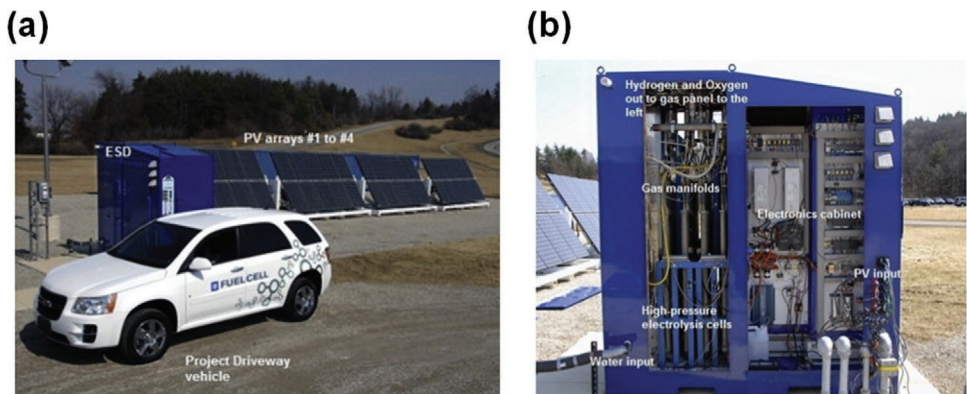


Figure 10. Photographs of: a) PV arrays and FCEV and b) alkaline electrolyzer system employed in a demonstration of solar hydrogen production.^[84] The PV system comprised 4 arrays of 10 Sanyo HIP-190BA3 PV modules. The modules were wired in parallel in each array and the arrays were wired in parallel to power the electrolyzer. An alkaline Avalence electrolyzer (Hydrofiller) employed a 28% KOH (by mass) electrolyte and operated at a pressure 13.8 MPa in both compartments. Reproduced with permission.^[84] Copyright 2011, Hydrogen Energy Publications, LLC (Elsevier Ltd.).

notable example is shown in **Figure 10**, where 40 monocrystalline silicon PV modules with a combined surface area of 47.2 m² and nominal module efficiency of 16.1% were coupled to a unipolar alkaline electrolyzer operating at an internal pressure of 13.8 MPa (~136 atm) without the use of power electronics.^[84] The size of the PV array was matched to the requirements of the electrolyzer to maximize the efficiency of the combined system. The average experimentally determined solar to hydrogen efficiency was ≈8.2%, which was a combined efficiency of the 13.7% efficiency of the solar to electrical step and the 59% efficiency (based on lower heating value) of the electrical to chemical step. A correlation from system operation and characterization over a 109 day period showed a clear relationship between the insolation and daily hydrogen output per unit area of PV for this system, averaging to 0.1 kg (H₂) (kW h)⁻¹ day⁻¹ m⁻², which shows the ballpark figure for the performance of such systems.

In general, the efficiency of the combined PV + electrolyzer system is a product of the individual PV and electrolyzer efficiencies, and the coupling factor between the two systems. The coupling factor, evaluated as the fraction between the real PV power output and its maximum power output, tends to be below unity since the PV efficiency is impacted by both the electrical load from the electrolyzer and changes in solar irradiance and temperature. While the irradiance is a natural factor and as such is beyond control, the PV and electrolyzer systems must be sized judiciously to maximize this coupling factor. Recently, efforts have been made to investigate the performance of both PEM and alkaline water electrolyzers directly coupled to multijunction III-V solar cells or silicon solar cells under concentrator or nonconcentrator natural sunlight, without the use of power electronics, and to examine the relative benefits between the up-scale of individual electrolyzers and series interconnection of smaller electrolysis units on the power point matching with the PVs.^[87,88]

1.4. The Concept of Integrating PVs and Electrolyzers into a Single Device

To date, PV and electrolyzer systems have undergone technical optimization and evaluation entirely independently of

one another. When the two systems become electronically integrated with each other, the electrolyzer is simply a downstream electrical load in the PV circuit. Unless the PV unit and electrolysis unit are sized optimally for integrated operation, power electronics become necessary, and these will contribute to the total energy loss. It is therefore unsurprising that the idea of morphing the photovoltaic and electrolysis components into one single device, namely a photoelectrochemical (PEC) reactor, has emerged and has become the subject of a vast body of research. Although the basic sequence of fundamental energy conversion steps, namely: i) solar to electrical energy conversion followed by ii) electrical to chemical energy conversion, remains the same, the requirements on the photoabsorbing and catalyst elements become immensely more complex and challenging to satisfy simultaneously. Consequently, the bulk of current research remains focused on material development. Nevertheless, the engineering considerations and challenges that currently apply to electrolyzer and PV systems will ultimately become important when the PEC systems evolve from the relatively rudimentary lab-scale devices into pilot plant scale systems.

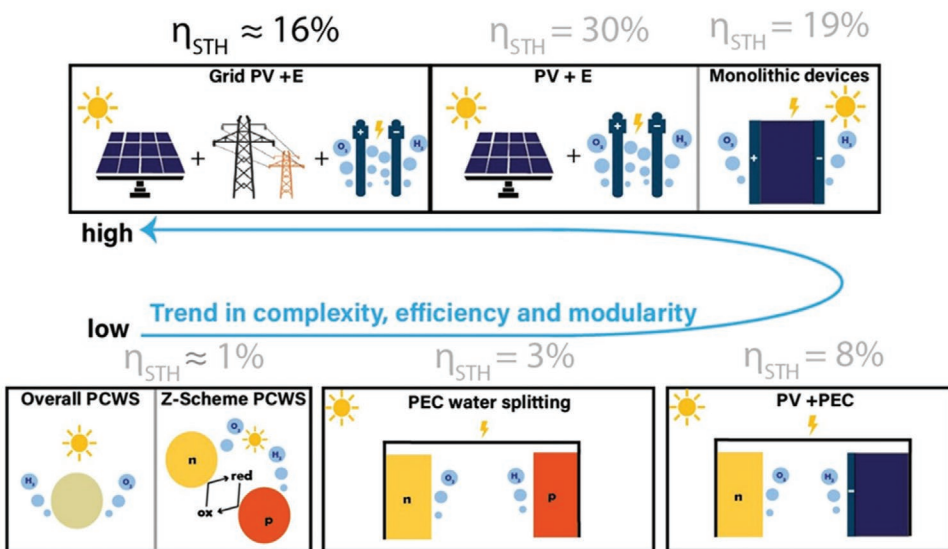
2. Principles of PEC Water Splitting

Solar-driven water splitting can be understood in terms of a series of distinct steps: i) photon absorption, leading to the formation of an excited state; ii) separation of the negatively charged electron and positively charged hole, which comprise the excited state, by an electric field or a potential step across an interface; iii) transportation of charges to a catalytic center; and iv) catalysis of the hydrogen evolution (HER) and oxygen evolution (OER) half reactions. Thus, the external quantum efficiency (EQE) of a solar-driven water splitting device can, broadly speaking, be divided into these distinct components^[89]

$$\text{EQE} = \phi_{\text{LH}}(\lambda) \times \phi_{\text{Sep}}(\lambda) \times \phi_{\text{Tr}} \times \phi_{\text{Cat}} \quad (2)$$

where the four terms on the right hand side correspond to the efficiencies of: $\phi_{\text{LH}}(\lambda)$ – light harvesting, $\phi_{\text{Sep}}(\lambda)$ – charge

Charge separating interface: p-n junction



Charge separating interface: semiconductor/electrolyte

Figure 11. A broad and simplified categorization of solar-driven water splitting device architectures based on modularity and efficiency. The efficiency of electrolysis is shown in black and assumes a 24% efficient solar cell, a transmission and distribution loss of 4%, and an electrolyzer efficiency of 70%. Efficiencies shown in gray represent record solar to hydrogen efficiencies (η_{STH}) for direct PV electrolysis,^[97] monolithic PV + E and PEC devices,^[98] which overlap with PV/PEC hybrid devices,^[96] PEC water splitting,^[91] and particle-based photocatalytic water splitting (PCWS) devices.^[99,100]

separation, ϕ_{Tr} – charge transport, and ϕ_{Cat} – efficiency of catalysis.

A simplified categorization of the most common methods of using solar energy to split water is shown in **Figure 11**. Here, water splitting devices are distinguished by the number of distinct components, modules, and/or interfaces given over to each term in Equation (2), as well as the nature of the charge-separating interface used to generate photovoltage. Typically, PEC systems utilize the potential drop across a semiconductor/electrolyte interface to separate charge and generate a photovoltage to drive reactions. By contrast, PV-based systems tend to use the potential drop across a buried p-n junction to generate a photovoltage and drive chemical reactions.^[90] This categorization should not be seen as totalizing or comprehensive, as many of the most effective and efficient systems reported to date utilize design elements from more than one of these categories,^[91–94] where additional PV modules can be added into PEC systems to directly drive a reaction or bias a device to boost efficiency (bottom right in Figure 11).^[95,96] In this section, we do not focus on a precise taxonomy for water splitting devices, which has been the subject of two detailed reviews;^[89,90] rather, we highlight the fact that moving across this technology spectrum leads to divergent strategies for material design and device engineering.

Overlaps, notwithstanding the distinctions shown in Figure 11, represent a trend of decreasing device modularity with efficiency. Grid-driven electrolysis represents one extreme of this spectrum, as each component in the system can be optimized independently of the other. At the other extreme, a dispersion of a single type of semiconducting particle is used to split water, namely, photocatalytic water splitting (PCWS).

Here, a single semiconductor/catalyst interface with electrolyte must mediate photon absorption, charge separation, transport, and catalysis.^[101] This simple device architecture cuts out many costly elements, and so holds the potential to produce hydrogen at lower cost due to a reduced balance of systems cost.^[102] This potential for reduced cost, however, tends to be counteracted by a trend of decreasing record efficiency, arising due to the terms in Equation (2) becoming coupled, as more demands are placed on a single material/interface. Here, modifying the semiconductor to improve one or more of these factors is more likely to affect the others. This makes improving simpler device architectures more challenging, as the interaction of, for example, a co-catalyst on charge separation and transport must be taken into account alongside any intended catalytic function.^[103,104]

Conversely, devices which contain separate modules for light absorption/charge separation and catalysis may be optimized individually to produce the highest efficiencies but only at (what are currently) unfeasibly high balance of system/capital costs.^[102] As a result of the different strengths and weaknesses across the technology spectrum, there is a divergent focus of research in these distinct fields, with an aim of bringing down costs through innovative fabrication procedures, concentration/heat management strategies, or by using lower cost photovoltaic materials in more modular devices, such as electrolyzers coupled to PV (PV + E),^[105–107] while greater focus on efficiency is found in the PEC and PCWS communities.^[108,109] These distinctions also lead to different barriers for device scale-up.^[109,110] To highlight the different challenges associated with each of these archetypal devices, we begin with a brief description of each.

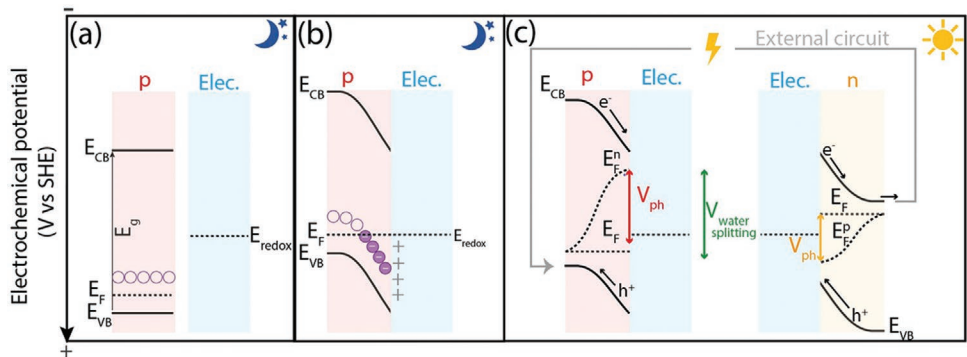


Figure 12. Principles of operation of an archetypal PEC device. a) The energy levels in the p-type semiconductor and the solution before the two phases come into contact are shown. b,c) The equilibrium condition between the Fermi level of the semiconductor and the redox potential of the electrolyte is depicted in the dark and under illumination, respectively.

2.1. Overview of Device Architectures

2.1.1. Direct PV-Powered Electrolysis and Monolithic Devices

The potential and challenges of directly connecting PV and electrolysis modules has been explored for over 40 years.^[111,112] However, in the mid-2000s, Lewis and Nocera popularized the concept of decoupling energy storage from the grid by co-locating PV and electrolysis units, and combining light harvesting and catalysis, into a single monolithic device.^[113,114] Here, one or more PV modules are typically encapsulated between two electrodes. A key distinction of the latter is that the semiconductors used in photovoltaics are immersed in the electrolyte and must be protected from photocorrosion, typically by coating the PV module with a transparent conducting oxide upon which an electrocatalyst is deposited. Unlike grid-powered or direct PV-powered electrolysis, the electric flux to the electrocatalysts in a monolithic cell is typically fixed by the surface area and operating current of the PV module.^[89] This coupling leads to lower current densities than would be obtained in wired PV + E or grid-powered electrolysis. Consequently, a lower cost electrocatalyst, optimized for operation at low current densities, is better suited to this application.^[115] The presence of an interlayer between the catalyst and semiconducting layers precludes complex interactions between the co-catalyst and semiconductor, enabling the “drop-in” use of a separately optimized electrocatalyst.

2.1.2. PEC Water Splitting

In an archetypal PEC water splitting device, the charge separating buried p-n junction is replaced by the interface between a doped semiconductor and electrolyte, as shown in Figure 12, leading to a single interfacial region driving charge separation and catalysis. Figure 12a shows that before contact is established between the two phases, a potential difference is present between the position of the Fermi level (E_F) of a doped (e.g., p-type) semiconductor and the redox potential of the electrolyte. Figure 12b illustrates that upon contact, the Fermi level of the semiconductor equilibrates with the redox potential of the electrolyte, leading to a flow of charge into

the semiconductor, resulting in the ionization (depletion) of acceptor states and a region of net negative charge. This region is known as the space charge layer (SCL) or the depletion region. The net negative charge of the SCL of a p-type material is balanced by a region of net positive charge in the electrolyte, created by a preponderance of positive ions near the surface of the semiconductor. Finally, Figure 12c shows that upon excitation with a photon of energy greater than the bandgap (E_g), an electron is promoted from the valence band (VB) to the conduction band (CB), leaving behind a positively charged hole. The resulting potential drop across the SCL drives holes into the bulk and electrons to the surface, resulting in a non-equilibrium electron density at the surface. This number of electrons that accumulates is described by an electron quasi-Fermi level (E_F^{q}) with the photovoltage (V_{ph}) being the difference between E_F and E_F^{q} . In an n-type semiconductor, holes accumulate at the surface and electrons are driven into the bulk. Consequently, p-type materials lend themselves to reduction reactions (photocathodes), while n-type materials are better suited to oxidation reactions (photoanodes). Connecting a photocathode and photoanode in series is known as a tandem configuration. Tandem cells produce a larger photovoltage and can absorb more of the solar spectrum if complementary bandgaps are chosen, and the cell is illuminated through the wider bandgap material first. Although bulk majority carriers will recombine via the external circuit, leading to the requirement of two photons to drive a single electron round the external circuit, this loss in charge separation efficiency will ideally be offset by harvesting more of the solar spectrum, leading to higher solar-to-hydrogen efficiency (η_{STH}).

As will be discussed in the following sections, this simplified architecture may represent a balance between the cost and efficiency associated with PV + E architectures with the lower cost and scalability of particulate PCWS devices. Although elegant, and potentially lower cost than PV + E, PEC-based devices pose a set of unique challenges for material design and engineering to produce a stable and efficient device. Without the presence of a protection layer, a direct interface with electrolyte in the presence of highly reactive photogenerated charges results in the photocorrosion of all but the most robust materials. Also, many robust oxide materials have non-ideal

charge transport properties, which must be addressed, both in terms of material design and reactor engineering, to produce an efficient device.^[95,109] If a co-catalyst is deposited directly onto the surface of the semiconductor, an additional interface is formed. This direct interface with a co-catalyst can lead to an additional set of complex interactions between the catalyst and semiconductor, such as modulation of the SCL, interfacial charge transfer kinetics, and surface passivation, all occurring in conjunction with catalysis.^[116,117] Due to coupling between catalysis and charge separation, the “drop-in” use of an independently optimized electrocatalyst is not guaranteed to produce the desired effect, leading to challenges in selecting a co-catalyst to overcome specific device limitations.

2.1.3. PCWS Devices

At the extreme end of the technology spectrum is PCWS. Here, a dispersion of one type of particle may drive both half reactions upon illumination, or alternatively, two particles may operate in tandem, connected by a redox mediator (otherwise known as a Z-scheme photocatalyst). Such systems are characterized by low-cost materials (as low as \$2 m⁻²^[109]) and advantages for scale-up, as the pH gradients generated by operation are neutralized locally, while the absence of external circuitry and long ionic diffusion lengths lead to negligible IR drops across the device.^[118] The last decade has seen remarkable advances, such as the advent of “photocatalyst sheet” devices produced using a technique known as particle transfer.^[119] Here, particles are embedded within a conducting mediator. This enables the production of both photoelectrodes^[120] and Z-scheme devices,^[100] the latter facilitated by a selective Rh/CrO_x co-catalyst capable of suppressing back reactions.^[121] Such devices represent a key advance in techniques to transform powders, which are often cheap to produce at large scale, into more efficient devices that share many of the characteristics of photoelectrodes. These important advances have increased η_{STH} from less than 0.1% to around 1%.^[109,102] However, the quantum efficiency of photocatalysts that harvest a larger fraction of the solar spectrum remains stubbornly low.^[109] The low modularity of the materials, combined with the complex nature of particle/catalyst/semiconductor interfaces,^[92] makes the rational design of next-generation photocatalysts a formidable challenge. Finally, it is also worth noting that when used as photoelectrodes rather than in a Z-scheme, photocatalyst sheet devices are generally opaque, which typically precludes their use as a top absorber in tandem devices.

2.2. PEC – A middle Ground between Simplicity and Efficiency

As shown in Figure 11, a range of η_{STH} have been achieved in various water splitting architectures, with traditional PEC devices reaching $\approx 3\%$,^[91] PV + PEC hybrid devices reaching $\approx 8\%$,^[96] and monolithic devices reaching $\approx 19\%$.^[98] Given that the efficiency of such devices falls between those achieved in PCWS ($\eta_{\text{STH}} \approx 1\%$)^[100] and direct PV + E ($\eta_{\text{STH}} \approx 30\%$) systems, PEC water splitting occupies the middle ground in terms of efficiency. Additionally, the degree of device complexity

(and likely cost) can also be considered a middle ground, with PEC devices being more complex than PCWS systems, as they require the photocatalyst to be supported on an electrode and the use of membranes for gas separation (with the exception of monoliths), but are less complex than PV + E systems, as these require the development of distinct PV and electrolyzer components, whereas PEC combines light absorption and catalysis within one component.

There are various benefits to developing PEC devices over the other systems described in Figure 11. For instance, in PEC devices, the catalysis occurs *in situ*, avoiding electrical transmission losses associated with PV + E systems.^[122] Moreover, PEC devices do not require platinum group metal catalysts to function, unlike in PEM electrolyzers that are required for PV + E systems (this is of particular concern for iridium-based electrocatalysts that drive the water oxidation reaction, with TW scale capacity unlikely given the scarcity of this metal).^[31] PEC systems can also utilize the low-cost and scalable materials found in photocatalytic water splitting architectures (typically transition metal oxide semiconductors) and achieve higher η_{STH} than such systems,^[120] while also producing the hydrogen and oxygen products in separate compartments. This latter point is particularly important, not only from a consideration of safety, since hydrogen and oxygen can form explosive mixtures, but also from a consideration of efficiency, as back reactions between hydrogen and oxygen can be minimized.^[123] Moreover, according to preliminary techno-economic analyses, PEC systems can achieve η_{STH} values that are commensurate to commercial viability (i.e., in the region of 10%).^[124] However, to achieve economic viability, one must consider other factors besides η_{STH} , including material cost and scalability, and the replacement lifetime of each component.^[125]

In summary, the shortcomings of cutting edge solar to fuels devices depend strongly on the device chosen and the materials used within the device. PEC and PCWS devices typically use low-cost materials and scalable techniques, but require improvements in efficiency. PV-based devices, using buried junctions, can show excellent efficiencies, but at a prohibitively high cost. We now turn to a more detailed discussion of the various classes of materials that have been explored for use in PEC and monolithic water splitting devices.

3. Material Choice for PEC Water Splitting

The first demonstration of a PEC water splitting device was in 1972, when Fujishima and Honda showed that a rutile titanium dioxide (TiO₂) photoanode, connected to a Pt counter electrode, could split water to, respectively, form O₂ and H₂ when irradiated with a Xe lamp alongside a small applied voltage bias.^[126] Since this seminal work, more than $\approx 14\,000$ papers have been published in the field of water splitting ($\approx 11\,000$ being on photoelectrodes), with the number of publications growing exponentially in recent years (≈ 9000 papers published from 2016 to now).^[127] A comprehensive review by Osterloh, carried out in 2008, documented more than 130 different semiconductors that had been studied for PEC water splitting.^[128] In the 12 years that have passed, this number has likely grown

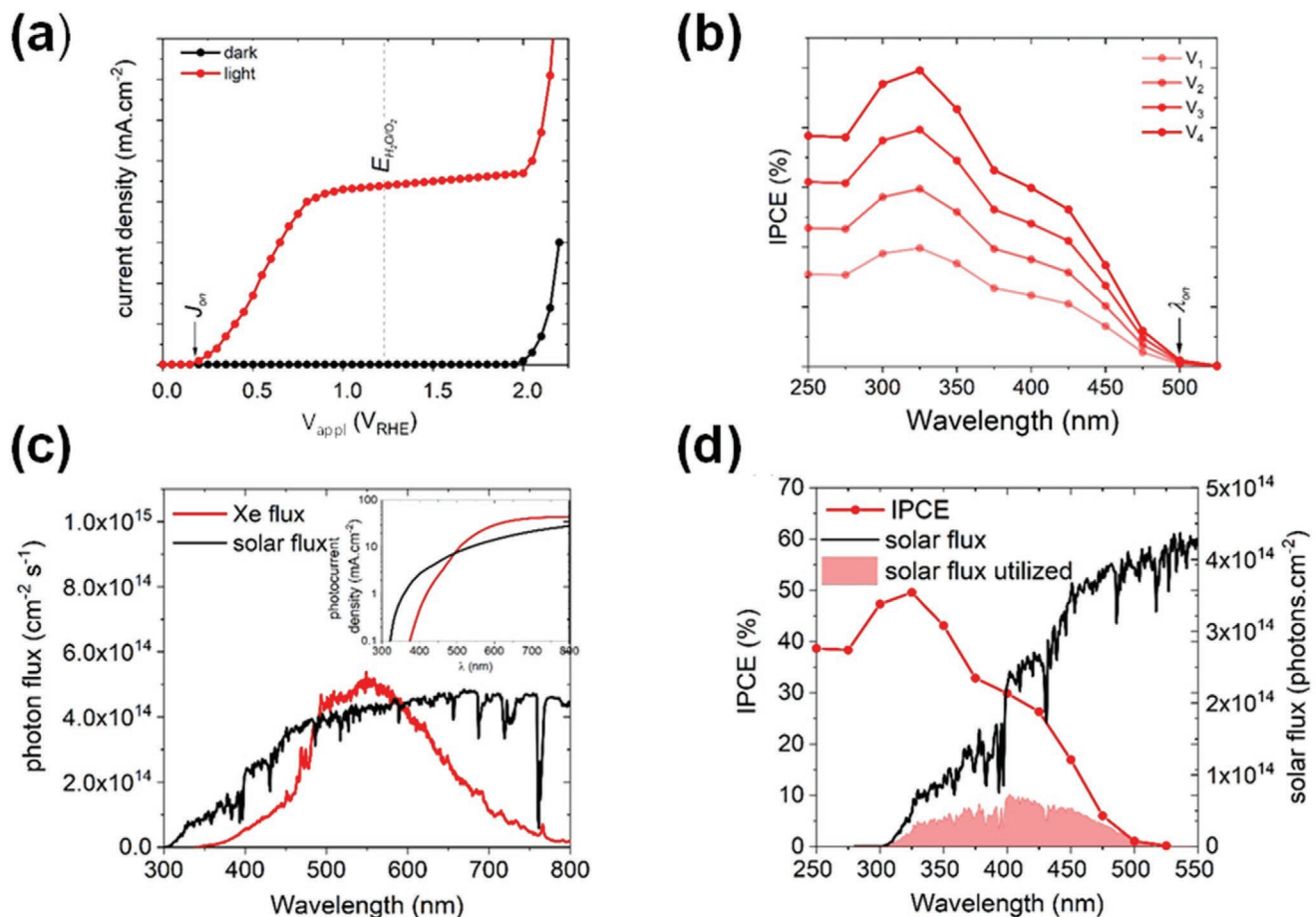


Figure 13. a) A generic photocurrent density measurement of a photoanode. In this case, the applied potential (vs V_{RHE}) is swept from cathodic to anodic potentials in the dark (black symbols) and light (red symbols); J_{on} represents the onset of the photocurrent and $E_{\text{H}_2\text{O}_2}$ represents the thermodynamic potential for water oxidation (1.23 V_{RHE}). b) A generic IPCE curve measurement carried out at a range of potentials for a photoanode, where $V_1 < V_2 < V_3 < V_4$; λ_{on} represents the highest wavelength where photocurrent is observed. c) A comparison of the spectral output from a typical Xe lamp (with a KG3 filter, adjusted to 100 mW cm^{-2} ; red line) and sunlight (AM 1.5 G, 100 mW cm^{-2} ; black line); the inset shows the maximum photocurrent density for a given bandgap for each light source. d) A graphical illustration of how the TSP can be determined by multiplying the IPCE curve (red symbols) with the AM 1.5 G solar spectrum (black line) to determine the solar flux that can be utilized (red shaded region).

considerably, in particular, since the advent of combinatorial methods for screening large libraries of materials.^[129–131] Summarizing the PEC water splitting performance of all materials studied to date is not the goal of this review. Rather, our goal is to summarize the performance of noteworthy and emerging materials. We begin with a summary of the key performance indicators for PEC water splitting materials and highlight best practice (Section 3.1). Following this, we discuss the fundamental requirements of materials for PEC water splitting, covering the intrinsic physical properties of various materials, and how these properties affect performance (Section 3.2). After providing a performance summary of what is considered state of the art (Section 3.3), we give an overview of the most common strategies for improving the performance of PEC materials, showcasing examples to illustrate each strategy (Section 3.4). We then end this section with a case study to illustrate the need for scalable device designs, and the key issues which must be addressed for solar-driven water splitting devices to contribute significantly to green hydrogen production (Section 3.5).

3.1. Key Performance Indicators

To enable comparison between the performances of PEC water splitting materials, we must first define the key performance indicators that one should measure.

3.1.1. Photocurrent Density

The most common measure of performance is photocurrent density; a generic example of the anodic photocurrent density response to applied electrode potential is shown in Figure 13a.^[108] This measurement is typically made in a 3-electrode cell, with the photoelectrode acting as the working electrode, an electrochemically stable material, such as platinum, as the counter electrode, and the reference electrode relative to which the working electrode potential is measured or controlled. The current is measured as the potential is swept in the anodic or cathodic direction; the resulting plot is therefore often called a

current–voltage or J – V curve. A positive photocurrent (oxidation) is measured on photoanodes, while a negative photocurrent (reduction) is measured on photocathodes. The first measurement is carried out in the dark, often starting from a potential that shows no photocurrent (e.g., the open-circuit potential), and sweeping the potential until some electrocatalytic behavior is observed. The second measurement is carried out under illumination (typically using a solar simulator or polychromatic light source with a similar spectral output to sunlight that has been adjusted to give 1 sun power, 100 mW cm^{-2}), sweeping over the same potential range. Some important performance indicators can be obtained by measuring the photocurrent density, including the onset potential where photocurrent is observed (J_{on}) and the photocurrent at the thermodynamic potential of the water splitting half reaction the PEC material drives (i.e., $1.23 \text{ V}_{\text{RHE}}$ for water oxidation in photoanodes and 0 V_{RHE} for water reduction in photocathodes). An ideal photoanode/photocathode should show a highly cathodic/anodic onset potential, and a sharp rise in photocurrent (i.e., good fill factor), to a plateau close to the theoretical limit set by the bandgap of the material. Applied potentials are normally reported against the reversible hydrogen electrode (RHE)

$$V_{\text{RHE}} = V_{\text{appl(RE)}} + \Delta V_{(\text{RE-SHE})}^{\phi} + (0.0592 \times \text{pH}) \quad (3)$$

where $V_{\text{appl(RE)}}$ is the applied potential versus the reference electrode and $V_{(\text{RE-SHE})}^{\phi}$ is the standard potential of the reference electrode (RE) used in the measurement.

3.1.2. Incident Photon-to-Current Efficiency (IPCE)

IPCE determines the fraction of photons that contribute to the photocurrent density for a range of photon energies. In the context of PEC water splitting, the IPCE describes the efficiency with which incoming photons of a given wavelength can produce hydrogen from water. In a typical measurement, the photoelectrode is held at a constant potential in the dark. The sample is then irradiated with monochromatic, often using a polychromatic light source coupled to a monochromator, resulting in photocurrent. With knowledge of the power of the incident monochromatic light, the IPCE at each wavelength can be determined using Equation (4)

$$\text{IPCE}_{\lambda} = \frac{F(J)_{\lambda}}{F'(I)_{\lambda}} \quad (4)$$

where $F(J)_{\lambda}$ is the measured current density expressed as a flux of electrons $\text{cm}^{-2} \text{ s}^{-1}$ and $F'(I)_{\lambda}$ is the intensity of the monochromatic light, expressed as a flux of photons $\text{cm}^{-2} \text{ s}^{-1}$. A generic example of an IPCE curve is shown in Figure 13b, where λ_{on} represents the highest wavelength where photocurrent is observed (which is dictated by the bandgap of the material).

3.1.3. Faradaic Efficiency (η_F)

The Faradaic efficiency (η_F) quantifies the proportion of the measured current that is generated by the desired reaction.

This efficiency may be determined by taking the ratio between the quantity of product that was measured and the quantity of product that was predicted based on the measured current (Faraday's law of electrolysis). In many materials, the photocurrent density observed is wholly due to the splitting of water, and as such, the Faradaic efficiency is unity. However, there are some materials which are not selective in driving the water splitting reaction (e.g., tungsten trioxide (WO_3))^[132] and instead drive undesirable reactions alongside water splitting, such as the oxidation of salts in the electrolyte. In a typical measurement, the photoelectrode is placed in a well-sealed vessel, and the photocurrent is measured typically for several hours at a constant potential. The hydrogen and oxygen produced are often measured using mass spectrometry or gas chromatography. The Faradaic efficiency is then determined using Equation (5)

$$\eta_F = N_{\text{measured}} / \frac{J \times A}{n \times F} \quad (5)$$

where N_{measured} is the externally measured molar flux of hydrogen or oxygen and $J A/nF$ is the predicted flux, which is based on the current density, J , electrode area, A , Faraday constant, F , and the electron stoichiometry of the reaction, n (=2 for water reduction and 4 for water oxidation).

3.1.4. Solar-to-Hydrogen Efficiency (η_{STH})

The solar-to-hydrogen efficiency (η_{STH}) for a photoelectrode is defined as the chemical energy produced per solar energy input, Equation (6)^[138]

$$\eta_{\text{STH}} = \frac{J \times (V^{\phi}) \times \eta_F}{P_{\text{solar}}} \quad (6)$$

where J is the photocurrent density (typically in mA cm^{-2}), V^{ϕ} represents the standard thermodynamic water splitting potential (1.23 V), η_F is the Faradaic efficiency of the reaction, and P_{solar} is the power of AM 1.5 G sunlight (100 mW cm^{-2}).^[133] Very often, the photocurrent density measured in a 3-electrode cell configuration is used to determine η_{STH} , with any applied bias being subtracted from V^{ϕ} ; however, the resulting equation is questionable since, for an applied bias $> 1.23 \text{ V}$, the equation yields increasingly negative efficiencies for increasingly high currents, which is nonsensical. For an appropriate formulation of the efficiency under applied bias, the reader is referred to.^[134,135] For the correct determination of the η_{STH} , the photocurrent density should be measured in a 2-electrode configuration, with the working and counter electrodes short-circuited. Other common errors in determining the η_{STH} are the measurements of the photocurrent density with the working and counter electrodes immersed in electrolytes of differing pH (creating a pH bias of $\approx 59.1 \text{ mV}$ per pH unit), and also, to measure the photocurrent density in an electrolyte that contains sacrificial chemicals, more commonly known as scavengers (creating a chemical bias).

An additional issue that is often not considered is the spectral mismatch between the light source used to carry out these measurements and AM 1.5 G sunlight. This is illustrated in

Figure 13c, which shows the spectral mismatch between a Xe light source (after passing through a KG3 filter to modify its spectral output to better match sunlight) and AM 1.5 G sunlight. We highlight the spectral differences of a Xe light source, as it is perhaps the most commonly used lamp for measuring photocurrent density in the field of PEC water splitting. The comparison shows that a Xe light source emits fewer photons in the UV region than AM 1.5 G sunlight. Using these two light sources, we can determine the maximum photocurrent density for a given bandgap, shown in the inset of Figure 13c. As shown, when using a Xe light source, photocurrent density will be underestimated for wide bandgap materials ($\lambda < 490$ nm) and overestimated for more narrow bandgap materials ($\lambda > 490$ nm). One way of circumventing this issue (apart from investing in a solar simulator light source) is to derive the photocurrent density from IPCE measurements, and is sometimes called a theoretical solar photocurrent (TSP).^[136] This is determined by multiplying the IPCE curve with the AM 1.5 G solar spectrum, integrating the flux that is utilized, and converting this flux into a current, as shown in Equation (7)

$$\text{TSP} = \frac{\lambda \times e}{h \times c} \int_{E_G[\text{nm}]}^{280[\text{nm}]} \text{IPCE}_\lambda \times I_\lambda \quad (7)$$

where I_λ is the spectral irradiance (AM 1.5 G) at a given wavelength and E_G is the material bandgap. A graphical illustration of how the TSP is determined is shown in Figure 13d. Another factor that should be considered is the photodiode that is used to measure the power of the light source. Typically, a Si photodiode is used, which possesses a E_G of ≈ 1.12 eV. Such a photodiode can only detect light of wavelengths less than ≈ 1110 nm, which accounts for $\approx 85\%$ of the solar spectrum in power terms. Also, the photodiode will show some losses in its conversion of light into a measurable photocurrent. Therefore, both of these factors should be taken into account before attempting to calibrate the light source.

3.1.5. Stability Measurements

Many photoelectrodes suffer from photocorrosion. To quantify degradation over time, one typically measures the change in photocurrent density with time. This is typically measured at either the operating potential of a complete device, or the thermodynamic potential of the water splitting half reaction that the photoelectrode drives. Although various technoeconomic analyses assume a set photoelectrode lifetime (before requiring replacement) of several years (typically somewhere between 10 and 20 years),^[102,137] most studies of photoelectrodes only measure stability for several hours (although it has been recommended that this be measured for at least 200 h to establish a better gauge of sample stability).^[138]

3.1.6. Completing the Device

Although there are instances where a single PEC material (when coupled to an electrocatalyst at the counter electrode) can drive solar water splitting with moderate efficiency, there

is greater overall benefit to develop two photoelectrodes (i.e., a photoanode and a photocathode) that each drive one half of the water splitting reaction. This benefit stems from the ability of a tandem system to utilize a greater portion of the solar spectrum.^[139] Theoretical studies suggest that η_{STH} of more than 25% can be achieved when using photoelectrodes in tandem (with bandgaps of ≈ 1.76 and ≈ 1.14 eV for the first and second absorbers, respectively),^[140] and that η_{STH} are limited to $\approx 12\%$ when using a single PEC material (with a bandgap of ≈ 2.25 eV). When deciding which PEC materials to pair in a tandem cell, one should consider if the bandgaps are complementary (i.e., they are not too similar), and importantly, if the J_{on} of the photoanode is sufficiently cathodic of the J_{on} of the photocathode.

3.2. Fundamental Requirements of Materials for PEC Water Splitting

It is generally accepted that to form the basis of a viable PEC device, a candidate material must meet a basic set of criteria.^[108,128,141] Candidate materials for PEC water splitting must: 1) be robust enough to withstand long-term continuous operation while immersed in electrolyte or, alternatively, be easily, cheaply, and reliably protected from corrosion; 2) possess a narrow enough bandgap to efficiently harvest the solar spectrum; 3) possess valence/conduction band edge potentials that are sufficiently oxidizing/reducing to drive water oxidation/proton reduction; 4) finally, and ideally, be fabricated using low-cost precursors using up-scalable production methods.

To some extent, these criteria conflict with one another; narrowing the bandgap to absorb more of the solar spectrum limits the possibility that both band edges in a single material will straddle the water oxidation and proton reduction potentials. Further, a loss of stability tends to be observed with decreasing bandgap.^[142] To date, no single material has been found which satisfies all of these criteria. However, by opting to use two semiconductors in a tandem configuration, criteria 2 and 3 can be relaxed, as the requirement that only one band edge in each material should straddle the proton reduction and water oxidation potential enables a greater number of narrow bandgap materials to be considered. As discussed earlier, tandem configurations also typically have greater theoretical efficiencies, provided materials with dissimilar and complementary bandgaps are chosen.

The current record for oxide-based PEC water splitting is held by a tandem device, shown in Figure 14a, utilizing p-type cuprous oxide (Cu_2O) as the photocathode and n-type Mo-doped bismuth vanadate (BiVO_4) (Mo:BiVO_4) as the photoanode, alongside appropriate back contacts, interlayers, and co-catalysts.^[91] However, the 3% η_{STH} of this device is lower than systems containing buried junction PV materials. This lower efficiency is to some extent counteracted by the fact that the device uses a simpler architecture and uses low-cost, up-scalable fabrication techniques (with the exception of the passivation layer grown on Cu_2O ; discussed later). Two important factors are responsible for this somewhat lagging performance, and relate to the bandgap of the materials. First, the relatively wide bandgaps of both BiVO_4 (2.5 eV; 550 nm) and

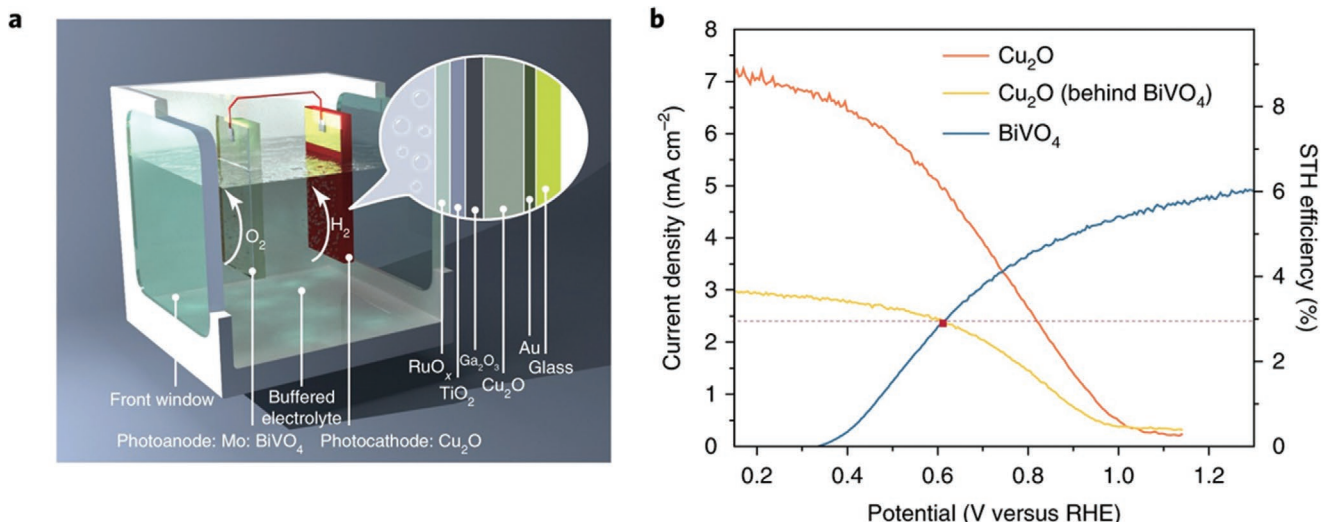


Figure 14. a) The device configuration of a record η_{STH} for a PEC tandem, with the inset showing the buried junction, protection, and catalyst layers used in conjunction with the Cu₂O photocathode. b) Effect of shading on the crossing point of the photocurrent density curves of the device. Reproduced with permission.^[91] Copyright 2018, Springer Nature.

Cu₂O (1.9 eV; 650 nm), in comparison to, for example, 1.1 eV (1130 nm) for a Si photocathode, leads to a lower maximum theoretical η_{STH} (roughly 8% for the device). Second, the two photoelectrodes have similar bandgaps. This results in parasitic absorption and lower operational currents due to the requirement for current matching between the two photoelectrodes, as shown in Figure 14b.

The limitations of the Cu₂O/Mo:BiVO₄ tandem are symptomatic of a broader obstacle to advancing PEC water splitting: a limited library of materials with properties which lend themselves

to application in PEC tandem cells. This is illustrated in Figure 15, which shows the electronic structure of a selection of commonly studied p- and n-type semiconductors for water splitting applications, highlighting the potential limitations of each. The stringent demands of finding two semiconductors with complementary bandgaps and appropriately positioned band edges lead to the exclusion of many materials. For example, commonly used d⁰ binary oxides, such as WO₃^[143] and TiO₂^[144] are often characterized by deep valence bands and wide bandgaps, which limit solar light harvesting (blue boxes in Figure 15). Binary

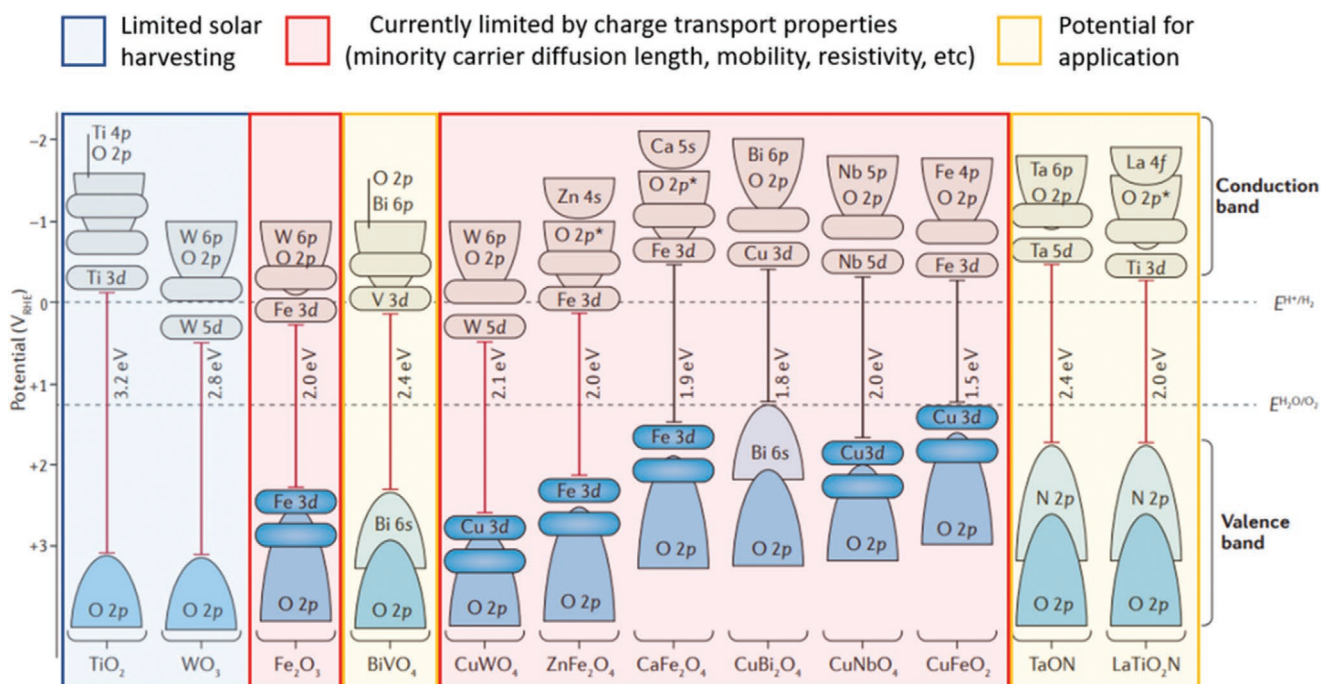


Figure 15. A critical appraisal of the light harvesting and charge transport properties of various transition metal oxides. Color scheme and appraisal of viability come from the same work. Adapted with permission.^[108] Copyright 2016, Springer Nature.

Table 1. A summary of the performance of state-of-the-art PEC water splitting materials and systems. J_{on} represents the onset potential where photocurrent is first observed (V_{RHE}); J_{therm} represents the photocurrent density (mA cm^{-2}) at 1 sun irradiance (100 mW cm^{-2}) at the thermodynamic potential of the water splitting half reaction the PEC drives (rows shaded a darker blue represent photocathodes and lighter blue represent photoanodes; monoliths that drive both halves of the water splitting reaction are not shaded); η_{STH} = solar-to-hydrogen efficiency (%) (asterisked values (*) are devices assisted with an external voltage bias); stability represents the loss in photocurrent density (%) for a given testing time (only included if measured for at least 15 min); η_F = Faradaic efficiency; ns = not stated. ALD = atomic layer deposition; BBNO = $\text{Ba}_2\text{Bi}_{1.4}\text{Nb}_{0.6}\text{O}_6$; CBD = chemical bath deposition; CIGS = copper indium gallium diselenide; CVD = chemical vapor deposition; DC = drop-casting; DSSC = dye-sensitized solar cell; ED = electrodeposition; EP = electrophoresis; HT = hydrothermal; I = impregnation; LT = lithography; MAPI = methyl ammonium lead iodide; MWA = microwave-assisted; N = nitridation; PECVD = plasma-enhanced chemical vapor deposition; PL = photolithography; S = sulfurization; SG = sol-gel; SP = spray pyrolysis; VLS = vapor–liquid–solid growth; VPD = vapor phase diffusion; ITO - indium doped tin oxide; VPE = vapor phase epitaxy; RF-MS = radio frequency magnetron sputtering; PD photodeposition; PT = particle transfer.

Material	Architecture	Synthesis	J_{on}	J_{therm}	η_{STH}	Stability	η_F	Ref.
III-Vs	GaAs/GaInP ₂ /Pt	VPE/ED	ns	ns	≈12.4	≈13%; 20 h	≈100	[159]
	Au/GaInAs/GaInP/Pt–Ru	ED/VPE/PVD	ns	ns	≈16	≈15%; 1 h	>96	[160]
	Rh/TiO ₂ /AlInP:GaInP/GaInAs/GaAs/RuO _x	ED/ALD/VPE/ED	ns	ns	≈19	≈17%; 20 h	≈100	[98]
Si	CoO _x /ITO/3× a-Si/SS/NiMoZn	ED/PVD/ED	≈0.4	≈3.25	≈2.5	≈20%; 24 h	ns	[165]
	n-Si/SiO _x /SnO _x /Ni	SP/PVD	≈0.9	≈31	≈4.1*	0%; 100 h	≈97	[166]
	a-Si:H/a-Si:H/mc-Si:H/AZO/Ag/Pt	PECVD/PLD	≈1.0	≈7.7	≈9.5	≈10%; ≈3 h	ns	[167]
	p-Si/n-Si/Ni–Mo	PL + VLS/CBD	≈0.46	≈9.1	≈1.9*	≈9%; 1 h	ns	[168]
	p-Si/n-Si/MoS ₂	VPD/PLD + S	≈0.35	≈17	ns	0%; 100 h	≈100	[169]
TiO ₂	p-a-Si:H/n-Si /n-a-Si:H/ITO/Pt	PVD/SG	≈0.64	≈33.4	≈13.3	≈15%; 20 h	ns	[170]
	Rutile TiO ₂ /anatase TiO ₂	HT	≈0.0	≈1.1	ns	—	ns	[184]
	Anatase:rutile TiO ₂	CVD	≈0.1	≈1.2	ns	ns	ns	[244]
	Ru–anatase:rutile TiO ₂	ED	≈0.2	≈1.65	ns	—	ns	[185]
	Anatase:rutile TiO ₂	SG	≈0.25	≈2.6	≈1.1*	ns	ns	[186]
$\alpha\text{-Fe}_2\text{O}_3$	Si–Fe ₂ O ₃	CVD	≈0.85	≈2.2	ns	ns	ns	[245]
	Si–Fe ₂ O ₃ /IrO ₂	CVD/EP	≈0.8	≈3.3	ns	≈12%; 3 h	ns	[190]
	Pt–Fe ₂ O ₃ /Co–Pi	CBD/ED	≈0.6	≈4.3	≈0.6*	≈7%; 3 h	ns	[191]
	Fe ₂ O ₃ + 2× c-Si	SP	≈1.0	≈0.15	≈0.55	0%; 1000 h	ns	[192]
	Si–Fe ₂ O ₃ /Al ₂ O ₃ /CoO _x + DSSC	CVD/ALD/CBD	≈0.6	≈1.8	≈1.2	≈20%; 8 h	≈100	[200]
WO ₃	WO ₃	PLD	≈0.5	≈2.4	ns	ns	≈50	[198]
	WO ₃	HT	≈0.6	≈3.7	ns	≈20%; 15 min	ns	[199]
	WO ₃ + DSSC	SG	≈0.5	≈2.7	≈3.1	ns	ns	[200]
	WO ₃ + 3× DSSC	SG	≈0.55	≈2.4	≈3.2	ns	ns	[201]
BiVO ₄	Li–BiVO ₄ /Fe:NiOOH/Co–Pi	SP + ED	≈0.2	≈4.2	ns	0%; 35 h	ns	[155]
	BiVO ₄ /Fe:NiOOH	ED + ED	≈0.2	≈4.7	ns	≈0%; 500 h	≈100	[246]
	SiO ₂ /Mo:BiVO ₄ /Fe:NiOOH + MAPI	LT + SG + ED	≈0.3	≈5.9	≈6.2	≈8%; 10 h	ns	[214]
	WO ₃ /BiVO ₄ /CoPi + GaAs/InGaAsP	PECVD + ED + ED	≈0.3	≈6.75	≈8.1	≈3%; 1 h	≈85	[247]
	Sn/Ni/Mo:BiVO ₄ /NiFeOOH	SG/PT	≈0.25	>4.4	ns	<5%; 1100 h	≈100	[120]
Cu ₂ O	Cu ₂ O/AZO/TiO ₂ /Pt	ED/ALD/ED	≈0.4	≈5.7	ns	≈22%; 20 min	≈100	[206]
	Cu ₂ O/AZO/TiO ₂ /RuO _x	ED/ALD/ED	≈0.55	≈5.0	ns	≈6%; 8 h	≈100	[207]
	Cu ₂ O/AZO/TiO ₂ /MoS _{2+x}	ED/ALD/ED	≈0.45	≈5.7	ns	≈0%; 10 h	≈100	[208]
	Cu ₂ O/AZO/TiO ₂ /RuO _x	ED/ALD/ED	≈0.5	≈7.0	ns	≈30%; 55 h	≈100	[209]
	Cu ₂ O/Ga ₂ O ₃ /TiO ₂ /NiMo + Mo–BiVO ₄ /Co–Pi	ED/ALD/ED	≈1.0	≈7.6	≈3.0	≈12%; 8 h	≈100	[91]
Fe ₂ TiO ₅	TiO ₂ /Fe ₂ TiO ₅ /CoO _x	ED/ED/ED	≈0.2	≈4.1	≈2.7*	≈0%; 2 h	ns	[225]
ZnFe ₂ O ₄	ZnFe ₂ O ₄ /Fe:NiOOH	CBD/ED	≈0.8	≈1.0	ns	≈0%; 16 h	≈99	[226]
BBNO	WO ₃ /TiO ₂ /BBNO/CoMnO _x	HT/ALD/SG/DC	≈0.6	≈3.75	ns	≈0%; 7 h	ns	[176]
CuFeO ₂	CuFeO ₂ /AZO/TiO ₂ /Pt	SG/ALD/ED	≈0.4	≈0.4	ns	≈10%; 40 h	≈100	[227]
CuBi ₂ O ₄	CuBi ₂ O ₄ /CdS/TiO ₂ /Pt	SP/CBD/ALD/ED	≈0.6	≈1.0	ns	≈80%; 3 h	≈91	[223]
Ta ₃ N ₅	Al ₂ O ₃ /GaN/Ta ₃ N ₅ + CIGS/Ni:Pt	RF-MS + PD	≈0.6	≈6.0	≈7	≈30%; 14 h	≈96	[234]
	Ta/Ta ₃ N ₅ /TiO ₂ /Ni(OH) _x /FH	HT/N/PD/ED	≈0.6	≈12.1	ns	ns	≈100	[237]

Table 1. Continued.

Material	Architecture	Synthesis	J_{on}	J_{therm}	η_{STH}	Stability	η_F	Ref.
TaON	TaON/IrO ₂	N/I	≈0.2	≈3.8	ns	≈75%; 2 h	ns	[241]
	TaON/CoO _x	N/I	≈0.2	≈3	ns	≈0%; 1 h	≈100	[242]
LaTiO ₂ N	LaTiO ₂ N/IrO ₂	N/I	≈0	≈3	ns	≈100%; 30 min	≈100	[240]
	LaTiO ₂ N//CoO _x	N/I	≈0.6	≈8.9	ns	≈66%; 2 h	≈80	[243]

oxides with non-zero d-electron occupancy and appropriate band edges, such as hematite (α -Fe₂O₃)^[145] and Cu₂O,^[146] as well as some ternary oxides, typically possess shallower valence bands and can more effectively harvest the solar spectrum. However, a more detailed examination of the optoelectronic properties specific to candidate materials leads to additional red flags and, potentially, further exclusions (red boxes in Figure 15). For example, despite its excellent corrosion resistance, relatively narrow bandgap and well positioned valence band, α -Fe₂O₃ is a charge transfer type Mott insulator (i.e., both the CB and VB are Fe 3d-based, due to an orbital splitting/localization, related to electron–electron repulsion^[147]) suffering from a high flat band potential, a high effective hole mass, poor hole mobility, relatively slow electron transport via polaronic states, and intrinsically fast bulk and surface recombination processes.^[148–151] As will be discussed, this leads to late onset potentials, which despite decades of intensive research, still limit the performance to the extent that α -Fe₂O₃ cannot be considered a viable material for PEC water splitting.^[145] This is not to say that new materials should be excluded on the basis of a preliminary analysis or screening, as it is not always easy to distinguish fundamental limitations in charge transport properties' deficiencies arising from suboptimal synthesis conditions in a new material.^[106] Further, the study of non-viable materials such TiO₂ and α -Fe₂O₃ as model systems forms the foundation for understanding how novel materials can be improved, and has furthered knowledge of how to form a consensus on the viability of new materials.

3.3. State-of-the-Art PEC: Performance of Notable and Emerging Materials

A wide range of materials have been examined for PEC water splitting, including III–Vs and Si, oxides, chalcogenides, nitrides, oxynitrides, and pnictides.^[102,128,152] In this section, we will focus only on notable and emerging materials, with a view to present what is considered state of the art in terms of efficiency and stability. For the materials covered herein, all performance data are summarized in Table 1. It should be noted that organic materials, including carbon nitrides and polymers,^[153] are an emerging class of materials, but to date, have shown low efficiency when applied in photoelectrodes, and as such, will not be covered in this review. For brevity, all photocurrent densities reported herein were measured at 1 sun irradiance (unless otherwise stated).

3.3.1. III–V and Si

Both III–V semiconductors, InP ($E_G \approx 1.35$ eV) and GaAs ($E_G \approx 1.42$ eV), and Si ($E_G \approx 1.12$ eV), possess near ideal bandgaps

for harnessing solar energy for use in PV, with bandgap energies close to the Shockley–Queisser efficiency limit.^[154] However, these materials do not possess sufficient potential energy to drive the water splitting reaction on their own, and either require voltage bias, or to be coupled with other materials to function. On the other hand, other III–V semiconductors, such as GaP ($E_G \approx 2.26$ eV) and GaInP₂ ($E_G \approx 1.83$ eV), possess near ideal bandgaps and band positions to drive the water splitting reaction.^[152] Nevertheless, all these aforementioned materials are highly susceptible to corrosion, and require protective coatings, often called passivation layers.^[155] Depending on the nature of the interface that is formed upon passivation, the material will either be classified as a photoelectrode (producing a photovoltage that is dependent upon being immersed in an electrolyte) or monolith (producing a photovoltage that is independent of being immersed in an electrolyte, otherwise known as a buried junction).^[90,98,156] To date, III–V semiconductors have achieved the highest η_{STH} . Respectively, there have been in the region of 250 and 500 publications for the application of III–V and Si semiconductors in PEC water splitting.

III–V Semiconductors: Although III–Vs have demonstrated the highest η_{STH} to date, many obstacles remain before they can find practical use in solar water splitting devices. Besides the various surface passivation strategies being developed to address the instability of III–V semiconductors, multiple cost reduction approaches are also being explored, including the use of solar concentration, epitaxial lift-off or spalling for substrate reuse, and integration on silicon substrates.^[107] A potential alternative to III–Vs are chalcogenides, such as copper indium/gallium diselenide (CIGS). Such devices can produce high efficiencies^[157] and may potentially be compatible with low-cost fabrication methods.^[158] As with III–V materials, stability remains an issue, with protection strategies being a key concern.

The strengths and weaknesses of III–V materials are well illustrated in key works. Khaselev and Turner showed that GaAs/GaInP₂ photocathodes, loaded with Pt surface co-catalysts, could drive unassisted water splitting (i.e., without requiring additional external voltage bias).^[159] The photo-absorbers were grown using vapor phase epitaxy, and the Pt catalyst was grown using electrodeposition. A η_{STH} of ≈12.4% was demonstrated with η_F of unity. However, after 20 h of testing, a performance reduction of ≈13% was observed. Young et al. synthesized GaInAs/GaInP photocathodes that could also drive unassisted water splitting, the device architecture shown in Figure 16.^[160] The GaInP and GaInAs layers were grown using vapor phase epitaxy on Au electrodes. The surface was decorated with a Pt–Ru surface co-catalyst, deposited by sputtering. A η_{STH} of ≈16% was demonstrated with η_F of 96%. However, similar to Khaselev and Turner, a 15% loss in the photocurrent density was observed after 1 h of testing. Khan et al. integrated

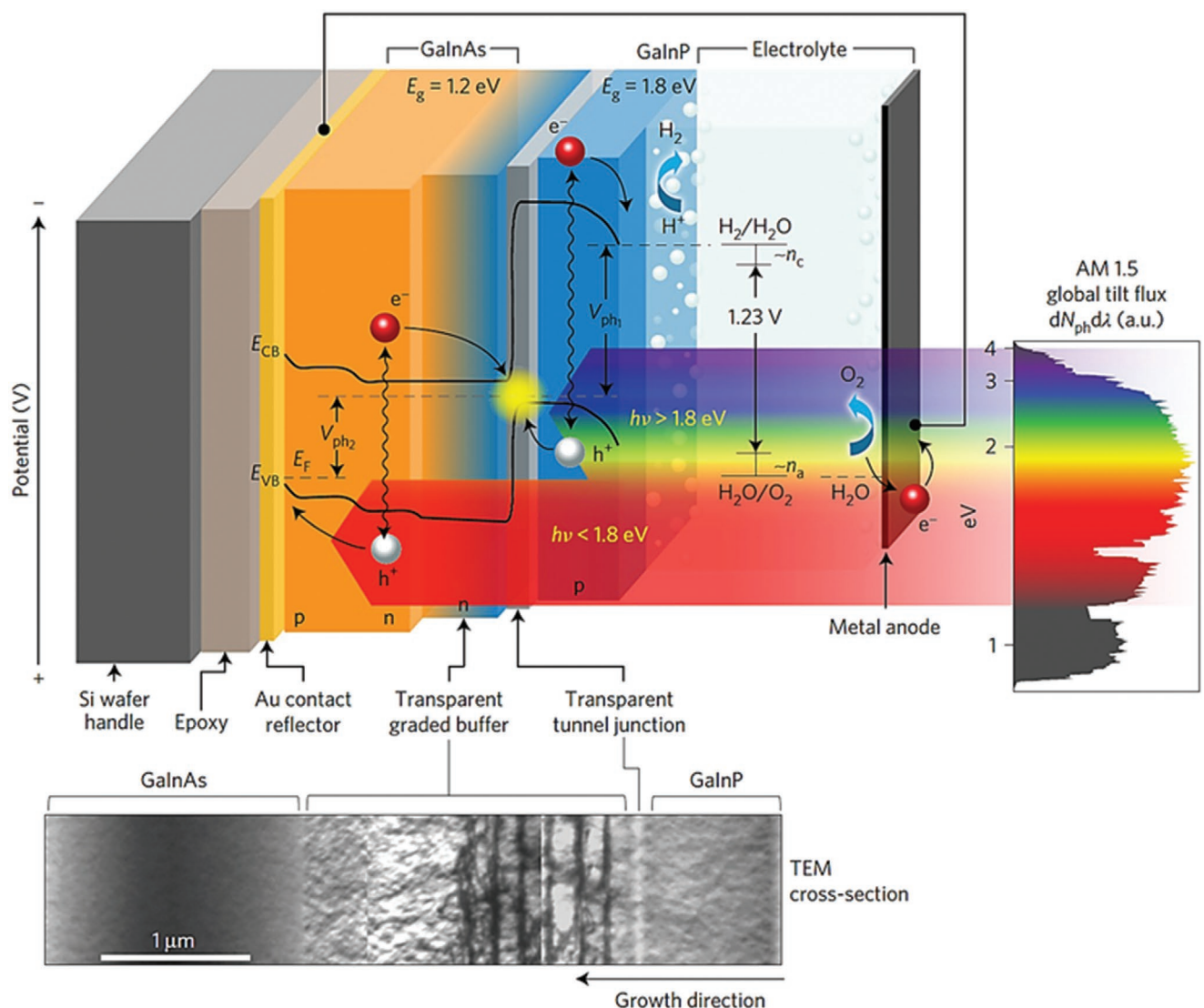


Figure 16. The architecture of the GaInAs/GaInP/Pt–Ru photocathodes developed by Young et al., showing the portions of the solar spectrum that are absorbed by each layer (right), alongside cross-sectional SEM images of the device layers (bottom). Reproduced with permission.^[160] Copyright 2017, Springer Nature.

a triple-junction GaInP/GaInAs/Ge photovoltaic within a PEC reactor.^[161,162] Ni foil was affixed to the Ge side of the photovoltaic, which drove the water oxidation reaction in solution. The GaInP side was wired to a Pt-coated Ti mesh, which drove the water reduction reaction. The device was examined for a range of concentrator simulated sunlight from 1 to ≈ 210 suns. At 1 sun irradiance, a η_{STH} of $\approx 14\%$ was achieved,^[162] whereas at ≈ 40 suns, a η_{STH} of $\approx 18\%$ was achieved. The device was stable and showed no signs of degradation, loss of performance, or Faradaic efficiency ($\approx 100\%$) over a 100 h testing period. Recently, Cheng et al. developed monolithic photoelectrodes that could drive unassisted water splitting with record efficiency.^[98] The device architecture was complex, requiring several synthetic steps to form a Rh/TiO₂/AlInP:GaInP/GaInAs/GaAs/RuO_x monolith. The photoabsorbers were grown using vapor phase epitaxy, the TiO₂ passivation was grown using atomic layer deposition, and the co-catalysts were grown using

electrodeposition. A η_{STH} of $\approx 19\%$ was demonstrated with η_F of unity. However, a 17% loss in performance was observed after 20 h of testing.

Silicon: There has been rapid recent progress in the development of Si for applications in PV. In many economies, reductions in production costs, alongside increases in efficiency, have resulted in grid power reaching price parity with fossil fuels.^[163] Si can be doped to give rise to n- or p-type conductivity for applications in photoanodes and photocathodes, respectively. However, the relatively small bandgap of Si (and thus relatively small photovoltage) means late onset potentials are unavoidable. Therefore, for use in unassisted PEC water splitting devices, Si should either be coupled with a wide bandgap semiconductor that possesses an early onset potential or stacked to form multiple junctions with increased photovoltage.^[164]

Reece et al. developed a monolithic “artificial leaf” using a triple-junction amorphous silicon (a-Si) solar cell.^[165] One side was

coated with indium doped tin oxide (ITO) and a CoO_x water oxidation catalyst, and the other side was affixed to a stainless steel electrode, where the back side was coated with a NiMoZn water reduction catalyst. The device could drive unassisted water splitting with a η_{STH} of $\approx 2.5\%$. Moreno-Hernandez et al. developed n-Si wafers for use as photoanodes.^[166] The wafers were passivated with a layer of SnO_x , grown by spray pyrolysis, and then coated with a Ni surface co-catalyst using a physical vapor deposition method. The photoanodes showed onset potentials of $\approx 0.9 \text{ V}_{\text{RHE}}$ and photocurrent densities of $\approx 31 \text{ mA cm}^{-2}$, with a η_{STH} of 4.1% . Stable photocurrents for $>100 \text{ h}$ were obtained, with a η_F of $\approx 97\%$.

High photocurrents but poor onset behavior in the absence of multiple junctions remain a key issue in the literature. For example, Urbain et al. grew triple junction a-Si photocathodes using plasma-enhanced chemical vapor deposition.^[167] The surface was passivated using Al-doped ZnO (AZO) and Ag layers, grown by sputtering, and loaded with a Pt surface co-catalyst. The buried junction could generate open-circuit voltages of $\approx 2.3 \text{ V}$ and short-circuit currents of $\approx 8 \text{ mA cm}^{-2}$. When connected to a RuO_x electrocatalyst, the device, shown in Figure 17, split water unassisted with a η_{STH} of $\approx 9.5\%$. However, pitting from corrosion was observed after a 3 h stability test, resulting in an $\approx 10\%$ drop in performance. Warren et al. synthesized Si microwire array photocathodes coated with a Ni–Mo surface co-catalyst.^[168] The microwire arrays were grown on p-type Si wafers using a combined photolithography and vapor–liquid–solid growth method. The Ni–Mo co-catalyst was grown using a chemical bath deposition method. Scanning electron microscope (SEM) images of the microwire arrays are shown in Figure 17. Onset potentials of $\approx 0.46 \text{ V}_{\text{RHE}}$ and photocurrents of $\approx 9.1 \text{ mA cm}^{-2}$ were observed, with a η_{STH} of $\approx 1.9\%$. An $\approx 9\%$ drop in performance was found after 1 h of continuous testing. Benck et al. developed p-Si wafers for use as photocathodes.^[169] A MoS_2 co-catalyst was grown on the surface of the photocathode using a two-step

process in which the Mo was first loaded by sputtering and then heated in the presence of H_2S . The photocathodes showed J_{on} of $\approx 0.35 \text{ V}_{\text{RHE}}$ and photocurrent densities of $\approx 17 \text{ mA cm}^{-2}$ at 0 V_{RHE} . No loss in performance was observed after 100 h of operation, with a η_F of $\approx 100\%$. Wang et al. produced buried junction photocathodes using triple-junction Si.^[170] The surface was passivated with ITO, and loaded with a Pt surface co-catalyst, using sputtering methods. The photocathodes showed J_{on} of $\approx 0.64 \text{ V}_{\text{RHE}}$, photocurrent densities of $\approx 33.4 \text{ mA cm}^{-2}$ at 0 V_{RHE} , and a η_{STH} of $\approx 13.3\%$. The stability was examined for 20 h and showed an $\approx 15\%$ drop in photocurrent density.

3.3.2. Transition Metal Oxides

Given their high durability, low cost, and ease of synthesis, transition metal oxides are the most studied class of material for applications in PEC water splitting. In general, some of the key **limitations to** the application of transition metal oxides in PEC water splitting are **their wide bandgaps, low absorption coefficients, and short minority carrier diffusion lengths**.^[172] Although the latter two limitations can be overcome by nanostructuring (discussed in Section 3.4.3), strategies to narrow their bandgaps, until recently, have largely failed (discussed in Section 3.4.2). As shown in Figure 18a, the most popularly studied transition metal oxides for PEC water splitting are binary oxides, including TiO_2 ,^[144,173] $\alpha\text{-Fe}_2\text{O}_3$,^[174] WO_3 ,^[143] and Cu_2O .^[146] However, some of the most promising emerging transition metal oxides are ternary oxides, such as BiVO_4 ,^[175] and quaternary oxides, such as $\text{Ba}_2\text{Bi}_{1.4}\text{Nb}_{0.6}\text{O}_6$.^[176–178] The band positions, relative to the water reduction and oxidation potentials, and bandgaps of anatase TiO_2 ,^[144,173] $\alpha\text{-Fe}_2\text{O}_3$,^[174] WO_3 ,^[143] and Cu_2O ,^[146] are shown in Figure 18b.^[179,180] Of these materials, only anatase TiO_2 possesses appropriate conduction and valence band energies (with sufficient overpotential) to drive overall water splitting.

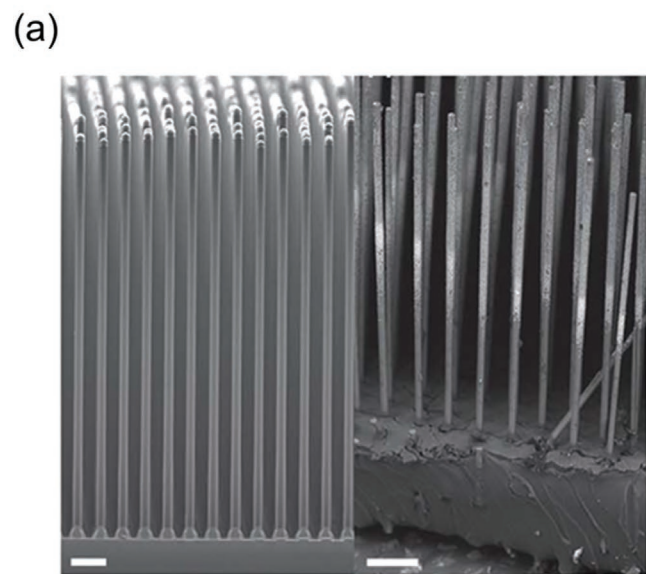


Figure 17. a) Si microwire array photocathodes developed by Warren et al. [scale bars represent $10 \mu\text{m}$]. Reproduced with permission.^[168] Copyright 2012, The Royal Society of Chemistry. b) The a-Si triple-junction architectures developed by Urbain et al. for unassisted water splitting. Reproduced with permission.^[171] Copyright 2016, The Royal Society of Chemistry.

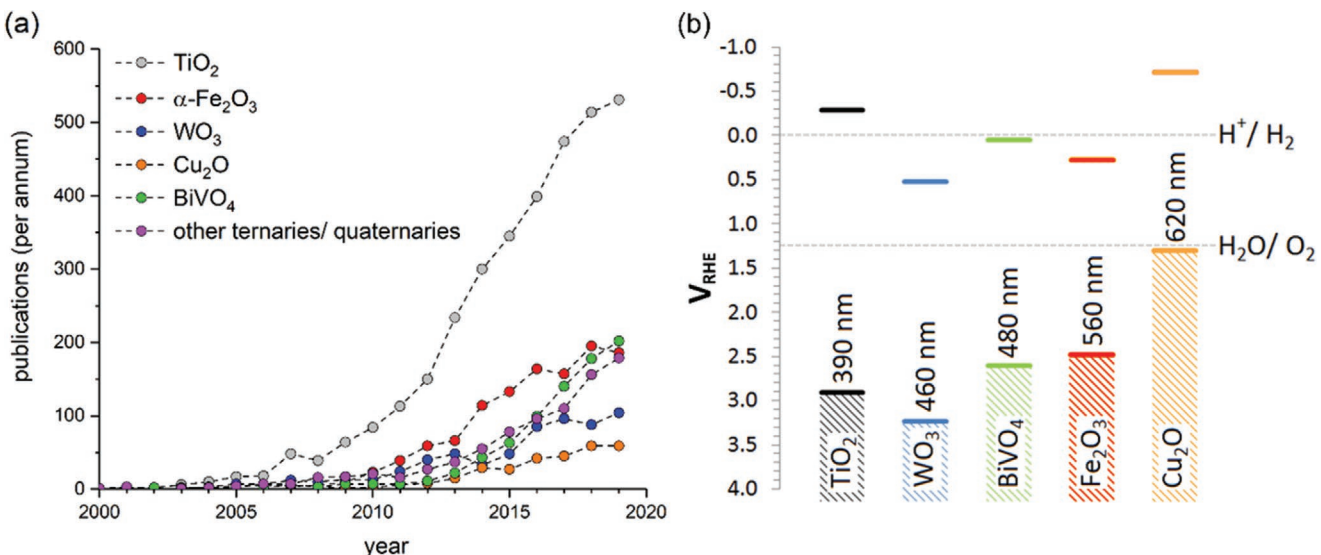


Figure 18. a) Publications per annum for PEC water splitting studies of TiO_2 , $\alpha\text{-Fe}_2\text{O}_3$, WO_3 , Cu_2O , BiVO_4 , and other ternary and quaternary oxides since the year 2000. b) The band potentials, relative to the water reduction and oxidation potentials, and bandgap energy (nm) for anatase TiO_2 , $\alpha\text{-Fe}_2\text{O}_3$, WO_3 , Cu_2O , and BiVO_4 .

TiO_2 : TiO_2 is the most studied material for applications in PEC water splitting, with ≈ 3700 publications to date.^[127] With n-type conductivity and a deep and oxidizing valence band, the material can be used as a photoanode to drive the water oxidation reaction with high light conversion efficiency. It is stable over a wide range of pH and applied potentials. Moreover, it is versatile, with the ability to drive a wide range of photochemical reactions,^[181] and is currently the only photocatalyst that has found large-scale commercial use with applications in self-cleaning windows and tiles, and air purifying paints and cements.^[182] Although photocurrent densities approaching the theoretical limits of this material have been demonstrated in several studies,^[173] its application in PEC devices is highly limited by its wide bandgap and therefore, low maximum theoretical efficiency (where the most commonly studied polymorph, anatase TiO_2 , has a bandgap of 3.2 eV and can only achieve a maximum theoretical η_{STH} of $\approx 1.3\%$).^[183] The material can be grown using relatively low-cost methods, with photoanodes that are categorized by their early J_{on} . Liu et al. grew nanostructured TiO_2 photoanodes using a hydrothermal method, where highly oriented rutile nanorods were decorated with anatase branches.^[184] The photoanodes showed a J_{on} of ≈ 0 V_{RHE}, and photocurrent densities that plateaued at ≈ 1.0 mA cm⁻² at ≈ 0.3 V_{RHE}. Roy et al. synthesized Ru-doped anatase:rutile TiO_2 nanotube photoanodes using an electrodeposition method.^[185] The photoanodes showed a J_{on} of ≈ 0.2 V_{RHE}, and photocurrent densities of ≈ 1.65 mA cm⁻² at ≈ 1.23 V_{RHE}. And, Liu et al. grew anatase:rutile TiO_2 nanowire photoanodes using a sol-gel method.^[186] J_{on} of ≈ 0.25 V_{RHE} were observed, which reached, to our knowledge, the highest photocurrent density to date, of 2.6 mA cm⁻² at ≈ 1.23 V_{RHE}. Moreover, a peak predicted η_{STH} of $\approx 1.1\%$ was found at ≈ 0.65 V_{RHE}.

$\alpha\text{-Fe}_2\text{O}_3$: $\alpha\text{-Fe}_2\text{O}_3$ is perhaps the second most popularly studied material for PEC water splitting applications, with ≈ 1300 publications to date. With n-type conductivity, $\alpha\text{-Fe}_2\text{O}_3$ finds use as a photoanode. It has some qualities, in that it is highly stable in alkaline conditions, and has a narrow bandgap

of ≈ 2.2 eV that facilitates a relatively high maximum theoretical photocurrent density of 12.6 mA cm⁻².^[174] Nevertheless, $\alpha\text{-Fe}_2\text{O}_3$ has many intrinsic limitations, including its highly anodic onset potential (typically in the region of 1 V_{RHE}), poor majority carrier conductivity, short minority carrier diffusion length (<4 nm), and low absorption coefficient.^[187] With the exception of the onset potential, all the aforementioned limitations have been overcome to a promising degree through doping and nanostructuring. Although the onset potential in $\alpha\text{-Fe}_2\text{O}_3$ can be cathodically shifted by the addition of surface co-catalysts, with some progress being made in this space,^[187,188] this remains one of the greatest barriers to the application of $\alpha\text{-Fe}_2\text{O}_3$ photoanodes in water splitting devices.

For instance, Kay et al. grew cauliflower-structured Si-doped $\alpha\text{-Fe}_2\text{O}_3$ photoanodes using chemical vapor deposition that showed J_{on} of ≈ 0.85 V_{RHE} and photocurrent densities of ≈ 2.2 mA cm⁻² at 1.23 V_{RHE}.^[189] However, when decorated with nanoparticulate IrO_2 surface co-catalysts, attached by electrophoresis,^[190] J_{on} was cathodically shifted to ≈ 0.8 V_{RHE} and photocurrent densities increased to ≈ 3.3 mA cm⁻² at 1.23 V_{RHE}. Unfortunately, the IrO_2 surface co-catalyst detached over time, with the photoanodes showing an $\approx 12\%$ drop in photocurrent density after 3 h of testing. Another notable example is by Kim et al., who synthesized worm-like structured Pt-doped $\alpha\text{-Fe}_2\text{O}_3$ photoanodes using a chemical bath deposition method, decorated with a Co-Pt surface co-catalyst by electrodeposition.^[191] These photoanodes showed relatively early J_{on} of ≈ 0.6 V_{RHE}, and achieved record high photocurrent densities of ≈ 4.3 mA cm⁻² at 1.23 V_{RHE}. There have also been some notable examples of PV + PEC systems using $\alpha\text{-Fe}_2\text{O}_3$. Vilanova et al. placed $\alpha\text{-Fe}_2\text{O}_3$ photoanodes, grown using a spray pyrolysis method, in tandem with two c-Si PVs, achieving a η_{STH} of $\approx 0.55\%$.^[192,193] Also, Brillet et al. placed $\alpha\text{-Fe}_2\text{O}_3$ photoanodes in tandem with a single dye-sensitized solar cell (DSSC) with high V_{oc} , and achieved a η_{STH} of $\approx 1.2\%$.^[200]

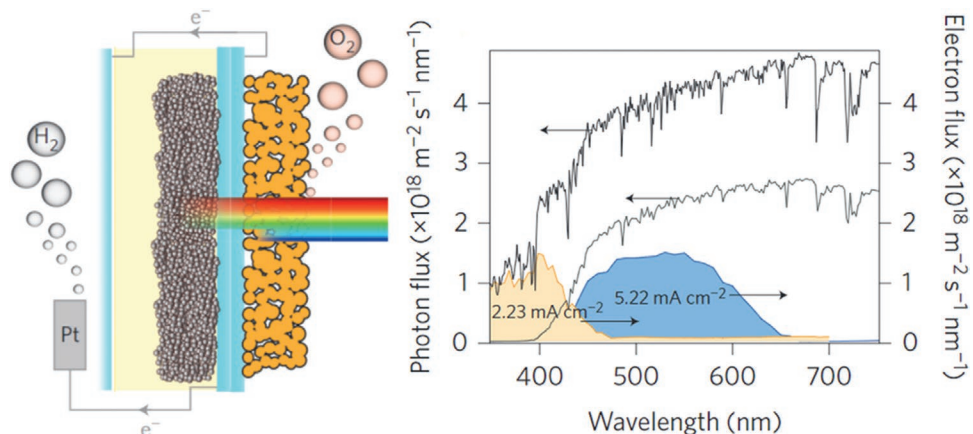


Figure 19. Mesoporous WO_3 photoanode, placed in tandem with a DSSC, developed by Brillet et al., reaching a η_{STH} of $\approx 3.0\%$. Reproduced with permission.^[200] Copyright 2012, Springer Nature.

WO_3 : WO_3 is another popularly studied material for applications as a **photoanode** in PEC water splitting, with >700 publications to date. It has a relatively **narrow bandgap** of $\approx 2.5\text{--}2.8$ eV, with a maximum theoretical photocurrent density of $\approx 5.9 \text{ mA cm}^{-2}$.^[194] It is **highly stable** when held at positive applied potentials in acidic conditions,^[195] and has a **deep and highly oxidizing valence band** for driving the water oxidation reaction, driving this reaction with substantially faster kinetics (turnover frequencies (TOFs) up to $\approx 100 \text{ s}^{-1}$) than many other commonly studied oxides (TOFs typically $<10 \text{ s}^{-1}$).^[196] WO_3 also possesses a longer minority carrier diffusion length (≈ 150 nm), in comparison with other commonly studied oxides (<100 nm).^[143] Although relatively early onset potentials are found in this material ($J_{\text{on}} \approx 0.5 \text{ V}_{\text{RHE}}$), electron extraction is slow (≈ 10 ms).^[197] Moreover, it is notorious for **showing low η_F** , where the deep and oxidizing valence band can parasitically oxidize the salts present in the electrolyte.^[132] Fabrega et al. showed that WO_3 nanorod photoanodes, grown using pulsed laser deposition, possessed J_{on} of $\approx 0.5 \text{ V}_{\text{RHE}}$ and photocurrent densities of $\approx 2.4 \text{ mA cm}^{-2}$ at $1.23 \text{ V}_{\text{RHE}}$.^[198] However, the η_F was low ($\approx 50\%$). Another notable example was by Wang et al., who grew highly orientated (002) nanoplate-shaped WO_3 photoanodes using a hydrothermal method.^[199] The photoanodes showed J_{on} of $\approx 0.6 \text{ V}_{\text{RHE}}$, and at $1.23 \text{ V}_{\text{RHE}}$, record high photocurrent densities of $\approx 3.7 \text{ mA cm}^{-2}$. However, this high performance was not stable, dropping by $\approx 20\%$ after just 15 min of testing, with this loss being attributed to the poor stability of the (200) facets. PV + PEC systems have also been demonstrated using WO_3 photoanodes. Brillet et al. placed mesoporous WO_3 photoanodes, grown using a sol-gel method,^[200] in tandem with a DSSC, shown in Figure 19, demonstrating η_{STH} of $\approx 3.1\%$. And, Lee et al. placed mesoporous WO_3 photoanodes in tandem with 3× DSSC in series, showing η_{STH} of $\approx 3.2\%$.^[201] A comparison of the literature to date finds that the performance of WO_3 photoanodes, in terms of J_{on} and photocurrent density, is intermediate of TiO_2 and $\alpha\text{-Fe}_2\text{O}_3$, with the added caveat of possessing low η_F .

Cu_2O : Cu_2O is a p-type semiconductor, and is perhaps the most widely studied material for applications as a **photocathode** in PEC water splitting, with ≈ 350 publications to date. Although Cu_2O possesses near ideal band positions to drive overall water

splitting, with a highly reducing conduction band for driving the water reduction reaction, and a narrow bandgap of ≈ 2.0 eV that facilitates a maximum theoretical photocurrent density of $\approx 14.7 \text{ mA cm}^{-2}$,^[200] it is highly susceptible to photocorrosion. This is not only because Cu_2O is a metastable phase, with a narrow window of stability,^[202] but also because the band positions in Cu_2O possess sufficient energy to both reduce the material to Cu and oxidize it to CuO .^[180] Given these intrinsic stability issues, protecting the surface of Cu_2O is a crucial requirement when developing this material for applications in PEC water splitting.^[146] This typically requires the use of atomic layer deposition, a technique capable of growing coatings on fragile substrates with atomic-scale thickness control.^[203] Nevertheless, compared to other traditional coating methods, the technique is expensive and slow, with limited uptake by industry to date.^[204] Although more low-cost solution-based methods are being developed for passivating Cu_2O ,^[205] the performance and stability demonstrated by such systems are far lower than what can be achieved using atomic layer deposition.^[146] Paracchino et al. synthesized $\text{Cu}_2\text{O}/\text{AZO}/\text{TiO}_2$ photocathodes, loaded with a Pt surface co-catalyst.^[206] The Cu_2O layer was grown using electrodeposition, the subsequent AZO and TiO_2 layers were grown using atomic layer deposition, and the Pt co-catalyst was grown using electrodeposition. The photocathodes showed J_{on} of $\approx 0.4 \text{ V}_{\text{RHE}}$ and a photocurrent density of $\approx 5.7 \text{ mA cm}^{-2}$ at 0 V_{RHE} . Although the η_F for H_2 formation was unity, stability was poor, with an $\approx 22\%$ loss in photocurrent after 20 min of testing. Given that the loss in performance was primarily attributed to the detachment of the Pt co-catalyst, in a follow-on study, this was replaced with RuO_x , grown using electrodeposition.^[207] The photocathodes showed J_{on} of $\approx 0.55 \text{ V}_{\text{RHE}}$ and a photocurrent density of $\approx 5.0 \text{ mA cm}^{-2}$ at 0 V_{RHE} , and more importantly, the stability of the photocathodes was substantially improved, with only an $\approx 6\%$ loss in photocurrent observed after 8 h of testing. Further studies showed that the RuO_x co-catalyst could be replaced with a more Earth abundant MoS_{2+x} co-catalyst,^[208] where these photocathodes showed J_{on} of $\approx 0.45 \text{ V}_{\text{RHE}}$, photocurrent densities of $\approx 5.7 \text{ mA cm}^{-2}$ at 0 V_{RHE} , and no observable loss in performance over 10 h of testing. It was also shown by Luo et al. that light absorption in Cu_2O photocathodes could be improved by introducing nanostructure

into their $\text{Cu}_2\text{O}/\text{AZO}/\text{TiO}_2$ system, loaded with a RuO_x surface co-catalyst.^[209] The photocathodes showed J_{on} of $\approx 0.5 \text{ V}_{\text{RHE}}$, and at 0 V_{RHE} , photocurrent densities of $\approx 7.0 \text{ mA cm}^{-2}$ and IPCEs $> 50\%$ at wavelengths $< 525 \text{ nm}$. However, an $\approx 30\%$ loss in performance was observed after 55 h of testing. In a follow-on study, the AZO layer was replaced with Ga_2O_3 , and the RuO_x co-catalyst replaced with the more Earth abundant NiMo co-catalyst.^[91] These photocathodes showed vastly improved onset potentials of $1.0 \text{ V}_{\text{RHE}}$, and photocurrent densities of $\approx 7.6 \text{ mA cm}^{-2}$ at 0 V_{RHE} . An $\approx 12\%$ loss in performance was observed after 8 h of testing, and when placed in tandem with a Mo-doped BiVO_4 photoanode loaded with a Co-Pt surface co-catalyst, the system achieved a record η_{STH} of $\approx 3\%$ for a wholly PEC device. Of note, this beneficial effect on photovoltaic, when coupling Cu_2O to Ga_2O_3 to form a heterojunction, was also observed by Chua et al. in their development of an all-oxide solar cell, which achieved a record high V_{oC} of $\approx 1.8 \text{ V}$.^[210]

BiVO₄ and Emerging Ternary and Quaternary Materials. BiVO_4 is one of the most promising emerging materials for applications as a photoanode in PEC water splitting devices, with ≈ 1000 publications to date. BiVO_4 has a bandgap of $\approx 2.4 \text{ eV}$, and therefore, a maximum theoretical photocurrent density of $\approx 7.4 \text{ mA cm}^{-2}$.^[211] It is generally found that the monoclinic scheelite structure is the most active phase.^[212] BiVO_4 is moderately stable at positive potentials in neutral pH. Although BiVO_4 is susceptible to photocorrosion,^[180] this process is kinetically slow, and can be suppressed by either using a vanadium rich electrolyte^[213] (that prevents the dissolution of vanadium ions from BiVO_4 into the electrolyte) or appropriate co-catalysts,^[120] with stable photocurrents demonstrated for over 500 h of testing. Although intrinsic BiVO_4 possesses poor electrical conductivity, this can be overcome by doping. Additionally, the poor absorption coefficient shown by this material can be overcome by nanostructuring, or growing it on top of nanostructured scaffolds (most often WO_3 , forming a heterojunction that further improves charge carrier separation, discussed in Section 3.4).

Prakash et al. synthesized nanoporous Li-doped BiVO_4 photoanodes using a spray pyrolysis method, that were subsequently coated with iron oxyhydroxide (FeOOH)/ NiOOH /Co-Pt surface co-catalysts using an electrodeposition method.^[272] The photoanodes showed J_{on} of $\approx 0.2 \text{ V}_{\text{RHE}}$, and photocurrent densities of $\approx 4.2 \text{ mA cm}^{-2}$ at $1.23 \text{ V}_{\text{RHE}}$. Qiu et al. coated SiO_2 nanocones with Mo-doped BiVO_4 , that was then loaded with a $\text{FeOOH}/\text{NiOOH}$ surface co-catalyst.^[214] The highly ordered SiO_2 nanocone arrays, coated with Pt and SnO_2 layers, were synthesized using a lithography-based method involving multiple steps. Mo-doped BiVO_4 was then grown on top of this scaffold using a sol-gel method. The $\text{FeOOH}/\text{NiOOH}$ surface co-catalyst was then grown using an electrodeposition method. The photoanodes showed J_{on} of $\approx 0.3 \text{ V}_{\text{RHE}}$, and at $1.23 \text{ V}_{\text{RHE}}$, achieved photocurrent densities of $\approx 5.9 \text{ mA cm}^{-2}$ and IPCEs $> 80\%$ at wavelengths $< 460 \text{ nm}$. In a PV + PEC arrangement, with a methyl ammonium lead iodide (MAPI) perovskite solar cell, unassisted water splitting was demonstrated with η_{STH} of $\approx 6.2\%$. Notably, Pihosh et al. developed record-high efficiency nanorod-structured $\text{WO}_3/\text{BiVO}_4$ heterojunction photoanodes decorated with a Co-Pt surface co-catalyst. The photoanodes were synthesized using a three-step method involving the physical vapor deposition of WO_3 nanorods, and the subsequent electrodeposition of BiVO_4 and Co-Pt layers. J_{on} of $\approx 0.3 \text{ V}_{\text{RHE}}$

were found, and at $1.23 \text{ V}_{\text{RHE}}$, photocurrent densities reached $\approx 6.75 \text{ mA cm}^{-2}$ and IPCEs were $> 90\%$ at wavelengths $< 475 \text{ nm}$. When placed in tandem with a double-junction photovoltaic, η_{STH} of $\approx 8.1\%$ were observed.^[96] It should be noted that there have been several other notable demonstrations of unassisted water splitting devices using BiVO_4 -based photoanodes alongside PV, demonstrating η_{STH} ranging from $\approx 3.5\%$ to 6.5% .^[215-219]

Given the promising PEC water splitting performance found in the ternary transition metal oxide BiVO_4 , alternative ternary and quaternary systems have been explored in an effort to develop more efficient photoelectrodes.^[106] This includes transition metal cuprates,^[220] ferrites,^[221] niobates,^[176] titanates,^[222] tungstates,^[223] and vanadates.^[224] A selection of promising examples are highlighted below.

Liu et al. grew Fe_2TiO_5 ($E_G \approx 2.2 \text{ eV}$) photoanodes, decorated with a CoO_x surface co-catalyst, on top of a TiO_2 nanorod scaffold using electrodeposition.^[225] The photoanodes showed early J_{on} of $\approx 0.2 \text{ V}_{\text{RHE}}$, and a promising photocurrent density of $\approx 4.1 \text{ mA cm}^{-2}$ at $1.23 \text{ V}_{\text{RHE}}$. A predicted η_{STH} of $\approx 2.7\%$ was achieved at $\approx 0.45 \text{ V}_{\text{RHE}}$, and no noticeable reduction in performance was observed within 2 h of testing. Zhu et al. synthesized ZnFe_2O_4 ($E_G \approx 1.9 \text{ eV}$) nanorods using a chemical bath deposition, that were then decorated with a $\text{FeOOH}/\text{NiOOH}$ surface co-catalyst using electrodeposition.^[226] J_{on} of $\approx 0.8 \text{ V}_{\text{RHE}}$ were observed alongside photocurrent densities of $\approx 1.0 \text{ mA cm}^{-2}$ at $1.23 \text{ V}_{\text{RHE}}$. Weng et al. fabricated highly nanostructured heterojunctions of $\text{Ba}_2\text{Bi}_{1.4}\text{Nb}_{0.6}\text{O}_6$ (BBNO; $E_G \approx 1.64 \text{ eV}$) on WO_3 nanosheets.^[176] The WO_3 nanosheets were first coated with a thin layer of TiO_2 grown by atomic layer deposition to prevent ion diffusion. The BBNO layer was grown using a sol-gel method, and then decorated with a $\text{Co}_{0.8}\text{Mn}_{0.2}\text{O}_x$ surface co-catalyst by drop-casting. The photoanode showed early J_{on} of $\approx 0 \text{ V}_{\text{RHE}}$, a photocurrent density of $\approx 3.75 \text{ mA cm}^{-2}$ at $1.23 \text{ V}_{\text{RHE}}$, and a negligible decrease in performance after 7 h of continuous testing.

Prévet et al. grew CuFeO_2 ($E_G \approx 1.5 \text{ eV}$) photocathodes using a sol-gel method.^[227] The surface was passivated by growing AZO and TiO_2 coatings using atomic layer deposition, and decorated with a Pt surface co-catalyst using an electrodeposition method. The photocathodes showed J_{on} of $\approx 0.4 \text{ V}_{\text{RHE}}$ and photocurrent densities of $\approx 0.4 \text{ mA cm}^{-2}$ at 0 V_{RHE} . They were relatively stable, showing only a 10% drop over 40 h stability test, and η_F of $\approx 100\%$. Wang et al. grew CuBi_2O_4 ($E_G \approx 1.5-1.8 \text{ eV}$) photocathodes using a spray pyrolysis process, which were passivated with CdS/TiO_2 overlayers and decorated with a Pt surface co-catalyst.^[228] The photocathodes showed onset potentials of $\approx 0.6 \text{ V}_{\text{RHE}}$ and a photocurrent density of $\approx 1.0 \text{ mA cm}^{-2}$ at 0 V_{RHE} with a corresponding η_F of $\approx 91\%$. However, the photocathodes showed significant losses in performance with time, due to the dissolution of the Pt catalyst, with an $\approx 80\%$ loss in 3 h.

3.3.3. Nitrides and Oxynitrides

Transition metal oxides tend to have deep valence band edges, due to the low potential of O 2p orbitals. Although a strongly oxidizing valence band can produce faster water oxidation kinetics,^[196] a deeply situated valence band tends to result in a wider bandgap that can limit solar harvesting. One potential solution to this problem is to replace O 2p orbitals with less

deeply situated N 2p orbitals. Over the last 20 years, a wide variety of nitride and oxynitride materials have been studied, leading to the discovery of three stand out materials: tantalum nitride (Ta_3N_5), tantalum oxynitride (TaON), and lanthanum titanium oxynitride ($LaTiO_2N$), each with ≈ 190 , ≈ 160 , and ≈ 60 publications to date.

Ta_3N_5 : Ta_3N_5 adopts an orthorhombic structure consisting of alternating Ta^{5+} -centered octahedra and tetrahedra.^[229,230] These mainly interact through edge sharing, with some tetrahedra sharing corners. This produces a semiconductor with an indirect bandgap of ≈ 2.1 – 2.2 eV.^[231] Being a d⁰ oxide, its valence band maximum consists mainly of N 2p orbitals, while its conduction band minimum consists mostly of Ta 5d states. Its intrinsic charge carrier transport properties are favorable, with effective electron and hole masses of 0.64 and 0.52 m_0 , respectively.^[229] As both band edges straddle the proton reduction and water oxidation potentials, in theory, Ta_3N_5 can drive both reactions. However, this has not yet been shown for a PEC device, but has been shown in a photocatalytic system of highly crystalline, spatially separated Ta_3N_5 nanorods grown by nitridation on the edges of $KaTa_3O_3$ particles.^[232] Ta_3N_5 shows n-type conductivity due to the presence of nitrogen vacancies in the lattice.^[233] Consequently, Ta_3N_5 is most commonly used as a photoanode in PEC devices to drive water oxidation. Overall water splitting has been demonstrated using a PEC device coupled to a CIGS cell, leading to a η_{STH} of 7%.^[234] This promising result is linked to the fact that Ta_3N_5 is one of the few narrow bandgap PEC materials shown to produce photocurrent densities close to the theoretical maximum. Before 2016, photocurrents of around 6 mA cm⁻² at 1.23 V_{RHE} were record values.^[235,236] However, in 2016, Li and co-workers showed that a Ta_3N_5 film (produced by nitridation of $NaTaO_3$) with a TiO_2 protection layer, a (Ni(OH)_x/ferrhydrite) hole storage layer, and a Co-based molecular catalyst produced a photocurrent density of ≈ 12.1 mA cm⁻² at 1.23 V_{RHE} close to the maximum possible value of 12.9 mA cm⁻².^[237] High IPCE was also observed, with values exceeding 90% below 550 nm. For such a strongly performing material, a relatively disappointing J_{on} of 0.6 V_{RHE} was observed, along with limited stability, an intrinsic limitation of Ta_3N_5 . Significant attention has since been paid to the origin of this limitation. Wang and co-workers have suggested a link between these two limitations – the onset potential and stability – with a decrease in photovoltage arising from the surface oxidation of the material when exposed to an electrolyte.^[238] The corrosive formation of Ta oxide species leads to a downward shift in the position of the Fermi level, thus limiting the maximum photovoltage that can be generated under operation. In addition, Li and co-workers have suggested that the presence of deep hole traps, arising from the presence of N vacancies, may also contribute to this process.^[239] Current work on Ta_3N_5 therefore is focused on surmounting the twin challenges of stability and relatively late onset potential.

TaON and $LaTiO_2N$: One possible means of combining the large photocurrents associated with Ta_3N_5 with the early onset potentials associated with oxides is to alloy with oxygen to form a ternary oxynitride, such as TaON, or quaternary oxynitride perovskite, such as $LaTiO_2N$. Promising J_{on} have been obtained for $LaTiO_2N$ (0.1 V_{RHE})^[240] and especially TaON (-0.2 V_{RHE})^[241], indicating both materials are not subject to the apparent

fundamental limitations associated with Ta_3N_5 . Thus, the remarkably early onset, combined with near ideal band edges, enables TaON to split water with the application of only 0.6 V in a two-electrode cell with a Pt electrocatalyst.^[242] However, to date, photocurrents in TaON (which has a wider ≈ 515 nm bandgap) fall significantly below the theoretical maximum of ≈ 8 mA cm⁻², with currents in the range of 2–4 mA cm⁻² being obtained at 1.23 V_{RHE}.^[241,242] However, photocurrents of up to 8.9 mA cm⁻² have been recorded using $LaTiO_2N$ (theoretical maximum of 12.5 mA cm⁻²).^[243] Significantly larger currents were obtained in the presence of a sacrificial electron donor, indicating a competition between the reaction and recombination of separated surface holes.^[240] This suggests further scope for improving the photocurrent of $LaTiO_2N$ with the use of improved overlayers and co-catalysts. However, to date, it is not clear if oxynitrides are more or less stable than nitrides, as no systematic evaluation of long-term stability has been performed, with papers noting that stability remains an issue, with ≈ 60 – 100% degradation often occurring on the timescale of hours,^[241] and only one report of negligible degradation over the course of 1 h.^[242]

3.4. Common Strategies for Improving Performance

3.4.1. Doping to Improve Conductivity

One of the simplest strategies to improve the performance of PEC materials is to improve conductivity. For photoelectrodes to function, majority carriers must be extracted from the electrode. However, in many commonly studied materials, such as α -Fe₂O₃ (≈ 0.01 – 0.1 cm² V⁻¹ s⁻¹)^[248] and BiVO₄ (≈ 0.2 cm² V⁻¹ s⁻¹)^[249] majority carrier mobility is low, especially when compared with WO₃ (≈ 10 cm² V⁻¹ s⁻¹)^[143] and anatase TiO₂ (≈ 20 cm² V⁻¹ s⁻¹).^[250] A common strategy to improve conductivity is to impurity dope the material and increase the concentration of majority carriers. This is because the conductivity, σ , of a semiconductor is proportional to the concentration of carriers, and controlled by Equation (8)

$$\sigma = n\mu_e + p\mu_h \quad (8)$$

where n and p represent the respective electron and hole carrier concentrations, and μ_e and μ_h represent the respective electron and hole carrier mobilities. In α -Fe₂O₃, various impurity dopants including Ti and Si have been used to improve conductivity. For example, Pu et al. grew nanostructured Ti-doped α -Fe₂O₃ photoanodes using a hydrothermal method that showed photocurrent densities of 2.25 mA cm⁻² at 1.23 V_{RHE},^[251] and Kay et al. grew cauliflower-structured Si-doped α -Fe₂O₃ photoanodes using chemical vapor deposition that demonstrated photocurrent densities of 2.2 mA cm⁻² at 1.23 V_{RHE}.^[189] In BiVO₄, various impurity dopants including W and Mo have been used to improve conductivity. For example, Abdi et al. grew gradient W-doped BiVO₄ photoanodes using a spray pyrolysis method that showed photocurrent densities of ≈ 1 mA cm⁻² at 1.23 V_{RHE}. These photocurrent densities were improved to ≈ 3.6 mA cm⁻² with the addition of a cobalt phosphate (Co-Pi) surface co-catalyst, and achieved a η_{STH} of $\approx 4.9\%$ when placed in tandem with a double junction amorphous silicon

photovoltaic.^[217] Also, Chen et al. grew Mo-doped BiVO₄ photoanodes using a physical vapor deposition that demonstrated photocurrent densities of $\approx 0.8 \text{ mA cm}^{-2}$ at 1.23 V_{RHE}, where these photocurrent densities were improved to $\approx 2.8 \text{ mA cm}^{-2}$ with the addition of a FeOOH surface co-catalyst.^[252]

3.4.2. Doping to Narrow the Bandgap and Improve Light Absorption

Apart from modifying the conductivity of semiconductors, impurity doping can also be used to modify the density of states, and in some cases, narrow the bandgap. The idea behind this strategy is to take wide bandgap PEC materials, which show high light conversion efficiencies, and narrow their bandgap through doping. Unfortunately, the results from using such a strategy are checkered, where in most cases only marginal gains in activity are observed.^[253–255] Various wide bandgap semiconductors have been studied, including ZnO, SnO₂, ZrO₂, and various perovskites,^[256] however, none more so than TiO₂.^[257,258] One of the most popular dopants for modifying the bandgap of TiO₂ is nitrogen.^[258] It is argued that when N dopants substitute O sites in the lattice, the 2p orbitals of nitrogen mix with the 2p orbitals of oxygen (that form the top of the valence band maximum in TiO₂) and thus cause the valence band maximum to lower in energy, and the bandgap to narrow^[258] (although the true role of such anionic dopants remains the subject of some debate).^[259] Torres et al. grew N-doped rutile TiO₂ photoanodes using a physical vapor deposition method, which showed photocurrent densities of $\approx 0.15 \text{ mA cm}^{-2}$ at 1.23 V_{RHE}, and IPCEs that showed an extension in performance from $\approx 425 \text{ nm}$ in intrinsic rutile TiO₂ to $\approx 550 \text{ nm}$ in the N-doped material.^[260] However, it should be noted that the IPCE decreased in the UV region for the N-doped material in comparison to the undoped material. To date, there remains no consensus as to whether or not N-doping is beneficial to the overall activity of TiO₂.^[144] Although visible light activity is granted, time-resolved studies of charge carrier behavior show that N-doping results in a deeper trapping of hole carriers, and therefore a loss in thermodynamic driving force for water oxidation.^[261] Another aspect that should be considered is the deep valence band of TiO₂, which can oxidize nitrogen species into nitrates,^[262] and over time, N-doped TiO₂ has been shown to “photobleach,” resulting in a loss in nitrogen and visible light absorption.^[263]

It has been argued that doped visible light absorbers of this kind are less active, as the energy levels formed by visible light absorbing dopants are spatially isolated (at typical solubility limits), and would thus result in less mobile charges and higher rates of recombination.^[109] In addition, doping strategies can also introduce states into the mid-gap, which trap photo-generated charge and act as recombination centers.^[264] Recently however, Wang et al. demonstrated that a co-doped, visible light absorbing wide bandgap semiconductor (SrTiO₃) can support quantum yields for water splitting exceeding 25% in the visible.^[100] Similar to Rh-doped TiO₂,^[265,266] visible light activity is introduced by Rh⁴⁺ substitution at Ti⁴⁺ sites, which introduces filled Rh 4d states above the O 2p valence band, thereby narrowing the bandgap.^[264,265] However, such singly doped materials appear to be inert, due to the inadvertent introduction

of mid-gap states upon Rh⁴⁺ doping that lead to the quenching of conduction band electrons.^[264,267] Chemical reduction of Rh⁴⁺ to Rh³⁺ appears to remove this mid-gap level,^[264] and can be achieved by co-doping Rh:SrTiO₃ with La³⁺,^[268] resulting in a highly active photocathode.^[93,100,119,268] For reasons not fully understood, this strategy appears to be less viable in TiO₂, possibly due to the reduced number of sites available for co-doping, which may be connected to a reduced tolerance of the anatase/rutile lattice to doping in comparison to perovskites,^[265,268] as well as possible resistance of the natural defect chemistry of TiO₂ to co-doping.^[269] An additional factor which may distinguish Rh-doped and La,Rh-co-doped SrTiO₃ from a host of ineffectual analogs is the strong p-type character observed in both materials,^[93,100,265,270] the origin of which has not yet been satisfactorily explained for the materials, given the electronic structures predicted by density functional theory (DFT).^[264,271] Of note, more narrow bandgap photoelectrode materials have also been subject to doping to further reduce the bandgap and therefore improve light harvesting, including BiVO₄.^[272,273]

3.4.3. Nanostructuring to Improve Light Utilization

Although transition metal oxides are one of the most promising classes of PEC material, they often possess short minority carrier diffusion lengths and low absorption coefficients.^[172] For instance, the average minority carrier diffusion lengths found in α -Fe₂O₃, TiO₂, and BiVO₄ are ≈ 3 , ≈ 15 , and $\approx 100 \text{ nm}$, respectively.^[187] Combined, these two factors can cause low water splitting efficiency, as a thicker material may harvest more of the solar spectrum, yet extract less charge. For instance, if light is absorbed too deep inside the material (i.e., too far beyond the SCL for the minority carriers that are formed to diffuse into), then the minority carriers that are formed cannot reach the surface and react (and will thus ultimately recombine). However, these two issues can be overcome with one simple, yet very effective strategy: to introduce nanostructure.^[274] This strategy is effective because the majority charge carrier diffusion lengths in transition metal oxides are often long. Therefore, by forming high surface area materials, minority carriers, despite their poor diffusion length, can diffuse to an interface with water and react. And, given the long diffusion length of the majority carriers, these nanostructures can be grown on a similar length scale, and thereby facilitate improved light absorption at the band edge. This strategy has been used to improve the efficiency in a wide range of materials, including TiO₂, BiVO₄, α -Fe₂O₃, Ta₃N₅, and TaON.^[275] There are additional benefits to nanostructuring, such as improved light harvesting through light scattering and improved charge transfer due to an increase in surface area, which are discussed in more detail by Osterloh in his review.^[276]

3.4.4. Heterojunctions for Improved Charge Carrier Separation

A heterojunction is the interface that is formed between two dissimilar semiconductors. When the energy levels of the two materials stagger (otherwise known as a type II staggered gap heterojunction), there is a thermodynamic driving force for

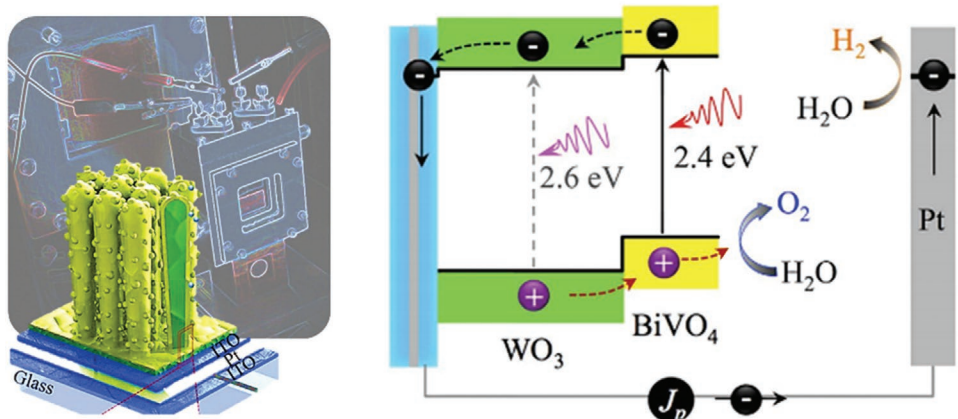


Figure 20. The $\text{WO}_3/\text{BiVO}_4$ heterojunction system, which has been used to great effect to improve the photocurrent densities in BiVO_4 -based photoanodes to $\approx 90\%$ of what is theoretically possible (showing photocurrent densities of $\approx 6.7 \text{ mA cm}^{-2}$ at $1.23 \text{ V}_{\text{RHE}}$ and 1 sun irradiance). Reproduced under the terms of the Creative Commons CC BY license.^[96] Copyright 2015, Springer Nature.

charge carriers to spatially separate. Heterojunctions are now routinely applied in the field of photovoltaics to improve solar conversion efficiency, for example, in p-i-n Si heterojunctions^[277] and bulk heterojunction organics.^[278] Increasingly, heterojunctions are being used in the field of water splitting to improve the performance of PEC materials.^[141] In this field, improving the spatial separation of charge, and thus charge carrier lifetime, is critical. This is because the kinetics at which these charges drive water splitting reactions are often far slower than the kinetics of recombination,^[279] with water reduction reactions typically taking place on the $\approx 1\text{--}10 \text{ ms}$ timescale^[280] and water oxidation reactions typically taking place on the $\approx 100\text{--}1000 \text{ ms}$ timescale.^[196] A similar strategy is used by photosystem II (PSII) in plants to drive the oxidation of water (facilitating one half of the photosynthesis reaction).^[54] The water oxidation complex in PSII exhibits turnover frequencies in the region of $\approx 100\text{--}400 \text{ s}^{-1}$, whereas charge carrier lifetimes in chlorophyll (the chromophore that absorbs solar energy to drive this reaction) are in the region of $\approx 5 \text{ ns}$ (a difference of roughly 6 orders of magnitude).^[281] However, by using a series of redox co-factors, the lifetime of charge carriers in PSII can be extended to $>\text{milliseconds}$, resulting in quantum yields $> 90\%.$ ^[54]

Many pairings of inorganic heterojunctions have been investigated for PEC water splitting, including anatase TiO_2 /rutile TiO_2 ,^[244] $\text{Cu}_2\text{O}/\text{TiO}_2$,^[206] and $\text{ZnO}/\alpha\text{-Fe}_2\text{O}_3$.^[282] However, one of the most popular pairings is $\text{WO}_3/\text{BiVO}_4$ for use as photoanodes.^[283] The band energies of WO_3 and BiVO_4 align in a staggered type II fashion, shown in Figure 20, where the transfer of electrons formed in BiVO_4 into WO_3 , and the transfer of holes formed in WO_3 into BiVO_4 , are both thermodynamically favorable, and therefore drive the spatial separation of charge. Using this strategy, Pihosh et al. demonstrated photocurrent densities of $\approx 6.7 \text{ mA cm}^{-2}$ at $1.23 \text{ V}_{\text{RHE}}$ ($\approx 90\%$ of what is theoretically possible for this material system).^[96] The high efficiency in this system has been attributed to the fast (sub-microsecond) transfer of electrons formed in BiVO_4 into WO_3 , thereby sufficiently prolonging the lifetime of the holes that remain in BiVO_4 to oxidize water (approximately milliseconds to seconds).^[282]

3.4.5. Improvement of Reaction Kinetics Using Surface Co-catalysts

There is often a large mismatch in the lifetime of charge carriers and the rate at which water splitting reactions occur. This mismatch can be reduced by improving the lifetime of charge carriers (i.e., using heterojunctions) or the reaction kinetics (i.e., using surface co-catalysts). A range of surface co-catalysts have been studied, from molecular complexes to solid-state nanoparticles and porous semiconductors. For example, Kay et al. showed that the photocurrent density of $\alpha\text{-Fe}_2\text{O}_3$ photoanodes could be improved from ≈ 2.2 to $\approx 2.6 \text{ mA cm}^{-2}$ at $1.23 \text{ V}_{\text{RHE}}$ by employing a CoO_x surface co-catalyst.^[189] Pastor et al. showed that the photocurrent densities of Cu_2O -based photocathodes (passivated with TiO_2 to prevent photocorrosion) show negligible photocurrent densities in the absence of a co-catalyst,^[284] but after the addition of a RuO_x surface co-catalyst, showed photocurrent densities in the region of $\approx 6 \text{ mA cm}^{-2}$ at 0 V_{RHE} . Pilli et al. showed that the photocurrent density of BiVO_4 photoanodes could similarly be improved from ≈ 0.30 to $\approx 0.95 \text{ mA cm}^{-2}$ at $1.23 \text{ V}_{\text{RHE}}$ by employing a Co-Pt surface co-catalyst.^[285] In another example, Kim and Choi showed that photocurrent density of BiVO_4 photoanodes could be improved from ≈ 1.6 to $\approx 4.4 \text{ mA cm}^{-2}$ at $1.23 \text{ V}_{\text{RHE}}$ by employing an $\text{FeOOH}/\text{NiOOH}$ surface co-catalyst.^[246]

3.5. The Scale Requirements for PEC Water Splitting Devices: A UK Case Study

Before one can consider the requirements for the scale-up of PEC devices, one should first gauge future demand for hydrogen. To do this, we present a case study for the UK, where natural gas in the UK is replaced with H_2 for winter heating. One of the key goals for the UK, made legally binding by the Climate Change Act, is to achieve at least net zero CO_2 emissions by the year 2050. Although power generation can largely be met by nuclear and renewables (such as photovoltaics and wind turbines), a pressing issue is how the UK tackles heating demand during wintertime. In the UK, $\approx 80\%$ of domestic

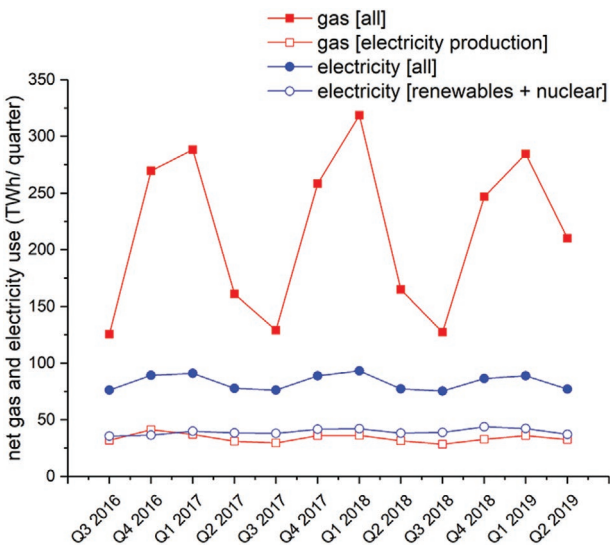


Figure 21. Net gas and electricity use in the UK (TWh per quarter) over the 3 year period from the third quarter of 2016 to the second quarter of 2019. Data are broken down into all gas use (red filled squares), gas use for electricity production (red open squares), all electricity use (blue circles), and electricity use from renewables (blue open circles). Data sourced from Ofgem.^[289]

heating is catered by natural gas.^[286] Moreover, there are occasions during cold weather events where peak hourly natural gas demand can be more than 4 times higher than peak electricity supply.^[287] This point is highlighted in **Figure 21**, which shows the net natural gas and electricity use in the UK over the 3 year period, running from the third quarter of 2016 to the second quarter of 2019. During the first and fourth quarters of any year (i.e., during the colder months), natural gas use is at its peak, ranging from ≈ 250 to 300 TWh per quarter. During the second and third quarters of any year (i.e., during the hotter months), natural gas use is at its trough, ranging from ≈ 125 to 150 TWh per quarter. On the other hand, electricity use throughout the year remains quite constant, ranging between ≈ 75 and 90 TWh per quarter. The mismatch between electricity and gas use is less severe during the second and third quarters (factor of ≈ 1.5); however, the mismatch is more substantial during the first and fourth quarters (factor of ≈ 3). It should also be noted that current electricity supply from nuclear and renewables forms $\approx 50\%$ of electricity generation. Considering all factors, to meet their CO₂ reduction target of net zero by 2050, it would be unreasonable to assume that the UK can replace current energy demands from gas (particularly during colder months) by simply increasing electrical energy production from renewables. However, a more viable strategy to remedy this mismatch is to replace natural gas with green hydrogen.^[14,288]

Now, let us assume the simplest case and neglect any potential contribution to energy storage from renewables and heat pumps, and focus exclusively on natural gas use for winter heating.^[290] From Figure 21, this amounts to ≈ 264 TWh for the first and fourth quarters combined (i.e., the colder half of the year). A recent study on the requirements for carbon neutral heating in the UK from hydrogen estimated a 55 GW production capacity.^[291] Encouragingly, our estimate here of ≈ 264 TWh, for the colder half of the year, is equivalent to ≈ 60 GW,

and is therefore in close agreement with their estimate. This energy can be converted using the gross calorific value of natural gas (≈ 40 MJ m⁻³)^[292] to the volume of natural gas required (≈ 22.5 bcm). Although it remains to be seen if the fuel conversion efficiency of commercial hydrogen boilers will be similar to current natural gas boilers, we will assume, for simplicity, that equivalent efficiencies will be attained. Therefore, as hydrogen (≈ 12.7 MJ m⁻³) possesses a lower gross calorific value than natural gas, this corresponds to a total volume requirement of ≈ 70.6 bcm of hydrogen for winter heating (or rather $\approx 3.15 \times 10^{12}$ moles of hydrogen). We will not account for hydrogen leakage, as this can be considered to be negligible,^[293] but is also yet to be quantified.

For this case study, we will assume that this volume of hydrogen will be exclusively produced using PEC devices (as opposed to PV + E or other renewably powered methods), and all in-house by the UK. Although various efficiency targets for PEC water splitting devices have been proposed, we will assume that the 10% η_{STH} target set by Mission Innovation^[294] is achieved. Of note, this target is a middle ground between current state-of-the-art device efficiencies found in III-Vs ($\approx 19\%$)^[98] and transition metal oxides ($\approx 3\%$).^[91] The average solar insolation level in the UK is between 750 and 1100 kWh m⁻² year⁻¹.^[295] If we assume light levels found in London in 2019 (≈ 1054 kWh m⁻² year⁻¹), then the average irradiance received is ≈ 120 W m⁻² (or roughly a 1/8th of 1 sun power). A 10% η_{STH} device would therefore generate a photocurrent density of ≈ 9.8 A m⁻². Assuming a Faradaic efficiency of unity, this results in a hydrogen production rate of ≈ 800 moles of hydrogen m⁻² year⁻¹ (or rather ≈ 800 million moles of hydrogen km⁻² year⁻¹). Therefore, to produce enough hydrogen to meet the UK requirements for winter heating, an active area of ≈ 4000 km² should be covered with such PEC devices; this area being roughly twice the size of Greater London.

From this case study, one can see that the scale of PEC production required to meet hydrogen demand for winter heating is quite vast (but certainly not unfeasible). For such a scenario to be realized, the methods used to fabricate PEC water splitting devices must be scalable, and ideally, use low-cost and durable materials. Therefore, one of the crucial challenges for the future development of PEC devices is their scale-up; currently, from bench scale research (Technology Readiness Level 4) to pilot scale and above (Technology Readiness Level 5 and beyond).^[296]

3.6. Summary and Future Prospects for Material Development and Scale-Up

To date, no device has shown performance metrics compatible with the production of low-cost green hydrogen at scale. The reasons for this shortfall vary between technologies, and the shortcomings of the materials which underpin them. Although record-high η_{STH} (19%) have been reached in devices using III-V materials, it is thought that such materials are currently incompatible with the cost targets set by the U.S. Department of Energy (DOE) because of the high cost and low scalability of the techniques used to produce them. Thus, progress in low-cost production techniques using methods compatible with large-scale manufacturing will be required to meet these

targets.^[156] Despite extensive studies on protection methods, devices based on III–Vs also possess limited stability in solution.^[297] Progress in these areas is essential for the development of technologies based on these materials.

There has been recent progress in the development of potentially less costly devices based on transition metal oxides, nitrides, and oxynitrides. These materials can be grown using methods currently used by industry to grow coatings at scale (e.g., electrodeposition, pyrolysis, chemical vapor deposition, etc.).^[298] For example, there have been various demonstrations using chemical vapor deposition to grow transition metal oxides for use in PEC devices.^[189,244] As this method is used by the glazing industry to grow fluorine-doped tin oxide (FTO) electrodes – a commonly used transparent electrode for PEC materials – we envisage that the production of PEC devices may be incorporated with their fabrication. However, significantly lower η_{STH} , in comparison to III–Vs, have been reached using such low-cost materials.^[91] This can be attributed to the limited number of narrow bandgap materials which show good stability and can operate efficiently. Consequently, the expansion of the library of narrow bandgap materials is a crucial area of research in this field. Although progress on ostensibly viable materials, such as $\alpha\text{-Fe}_2\text{O}_3$, has ultimately been limited by deficiencies in fundamental charge transport properties, the example of BiVO_4 demonstrates that stable and efficient materials with a narrower bandgap can be produced. Already, some promising examples have been found which suggest the viability of this approach: LaTiO_2N ^[240] possesses a 600 nm bandgap and can operate close to its theoretical limit, while BBNO exhibits a bandgap which may be continuously tuned, and greatly improves the visible light harvesting of wider bandgap materials when implemented in a heterojunction.^[176] However, some less costly materials, such as Cu_2O , are also susceptible to corrosion, and currently, can only be protected using atomic layer deposition methods.^[206] As atomic layer deposition is a slow and relatively expensive process,^[204] this remains a significant barrier to the scale-up of PEC devices based on such materials.

A further crucial area of development for all device designs is the lack of basic research into scale-up. Despite the large number of publications in the field of PEC water splitting to date ($\approx 11\,000$), most studies have focused on developing only one half of the device (either the photoanode or the photocathode). By comparison, the number of studies that present the development of a complete water splitting device is lacking.^[299] Even here, most devices are demonstrated on the $\approx 1\text{ cm}^2$ scale.^[300,301] Recently, however, more studies have been carried out at scales more commensurate to their commercial application.^[95,302] From such work, several design engineering considerations have emerged, which must be addressed for any device architecture to be successful, and will be discussed in Section 4.

4. Engineering Considerations in PEC Reactor Design

Electrolyzers and PV systems have followed their respective research and development, and commercial deployment trajectories separately. A great many technical problems have been solved, but many challenges remain. It would therefore be an understatement to say that researchers working on PEC

systems now have a difficult task ahead of them, which is to resolve in one system the technological and economic demands hitherto placed on two separate systems.

PV materials, panel designs, trackers, and concentrators for solar electricity generation have been developed and installed to suit particular applications, including domestic, industrial, grid-scale, or extraterrestrial, as well as varying locations, whether deserts, cities, or snow-covered landscapes. They function under predictable conditions. Current collection in cells, anti-reflection layers, and encapsulation for corrosion protection have been optimized to maximize performance and longevity and so, commercial PV materials are not instantaneously adaptable to being immersed in aqueous environments under strongly reducing/oxidizing conditions. Trackers and concentrators have been designed to manage electricity transportation and to support heat dissipation, but not the transportation and processing of flammable gaseous products such as hydrogen. Even without the use of optical components, the collection of hydrogen gas from arrays of PEC cells distributed in a solar field is viewed as a significant challenge for the deployment of large-scale PEC water splitting.^[303]

From the perspective of electrolyzers, in addition to generating hydrogen within compact stacks with minimal Ohmic, overpotential, and parasitic losses and aiding multiphase flow, they must now accommodate photoabsorbing elements and respond to constant changes in power supplied by solar photons.

The approach to designing the “2-in-1” system naturally started with the development of new multifunctional (photo) electrode materials, and this research is still the focus of the field. However, scale-up considerations merit more discussion than they are currently receiving. Required expertise in electrochemical and photoelectrochemical reactor engineering is unique and so is presently the second limiting factor behind materials. However, engineering progress is required urgently, because with a shortage of demonstration prototypes and pilot plants, it is difficult to envisage what an industrial scale installation for PEC hydrogen generation might look like. This must change in the near future if this type of solar hydrogen technology is to help nations meet their greenhouse gas reduction goals.

4.1. The Engineering Challenges of PV and Electrolyzer Integration into a Single Device

Research published over the last decade reveals a wide variety of PEC system designs, reflecting the many ways in which electrolyzers and PV can be morphed together. The different levels of photoabsorber and electrolyzer integration led to ambivalence over design classifications and had prompted the development of a specialized taxonomy, through which different devices may be distinguished.^[90] The taxonomy of 10 device types, which may be understood using an accompanying algorithm, enables one to get an indication about the potential complexities in the device design, which typically increases with the level of photoabsorber and electrolyzer integration. What has also been particularly helpful is a set of schematic, 2D, representations of devices created by various research teams.^[304] These are

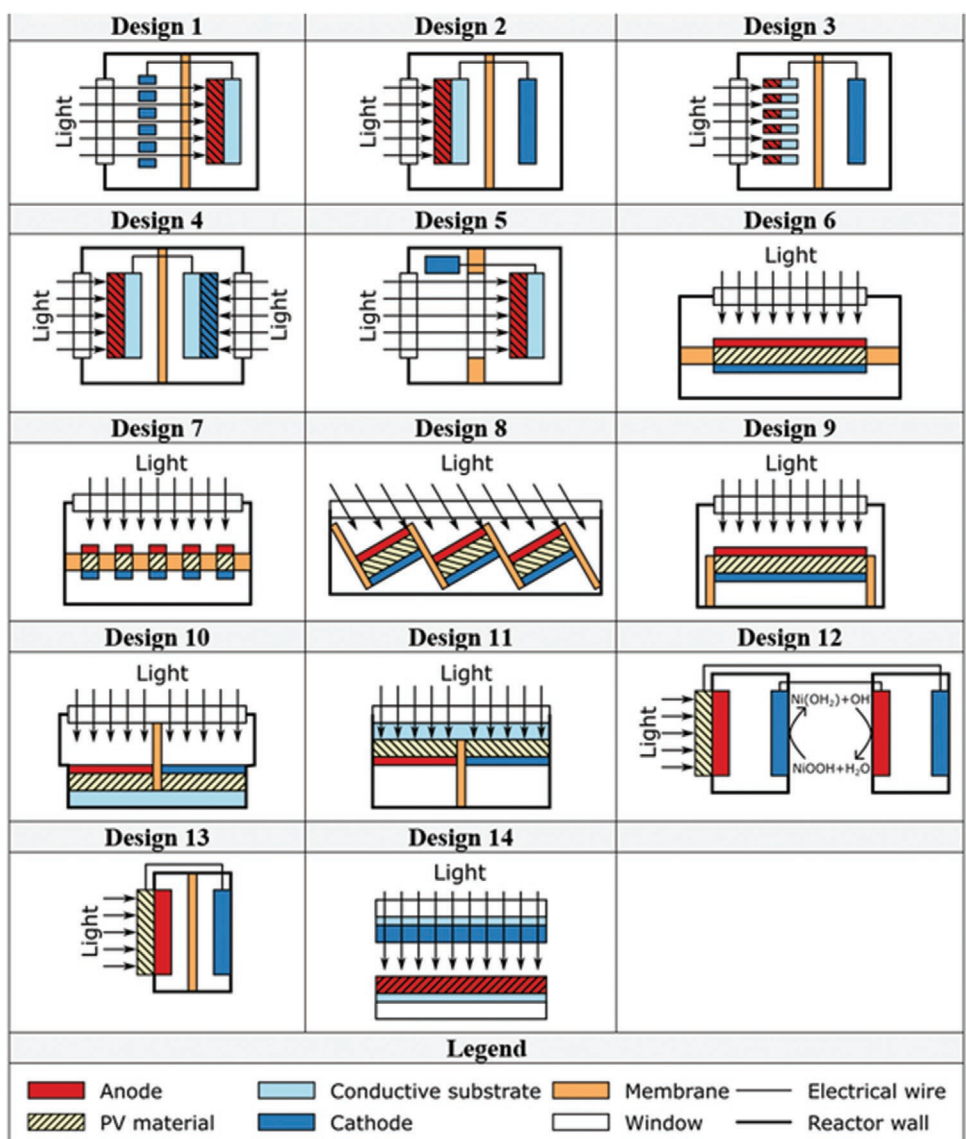


Figure 22. Schematics of various PEC device designs found in the literature: Design 1,^[305] Design 2,^[306–308] Design 3,^[314] Design 4,^[306,309] Design 5,^[310] Design 6,^[311–313] Design 7,^[313–315] Design 8,^[316] Design 9,^[317] Design 10,^[314] Design 11,^[314,318] Design 12,^[319] Design 13,^[320–322] and Design 14.^[323] Reproduced with permission.^[304] Copyright 2019, Scrivener Publishing LLC.

shown in **Figure 22**. Since the publication of these schematics, additional designs have materialized; our interpretations of these are shown in **Figure 23** following the same legend as Figure 22. The variety of designs will likely increase in the coming years as work on devices continues.

Devices can be broadly described at two levels: 1) conceptual design and 2) the physical layout of all the components within the reactor system.^[304]

The conceptual design defines the type of system through information on i) the number of photoabsorbers, which allows the *a priori* determination of the maximum theoretically

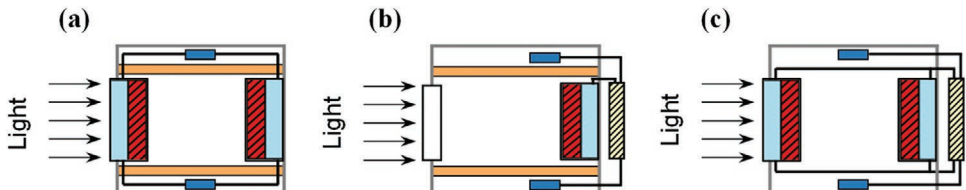


Figure 23. a–c) Additional reported device designs, drawn following the same legend as in Figure 22: (a) in this design, an external bias is required (not indicated explicitly in the schematic),^[324] (b) refs. [192,193], and (c) ref. [95].

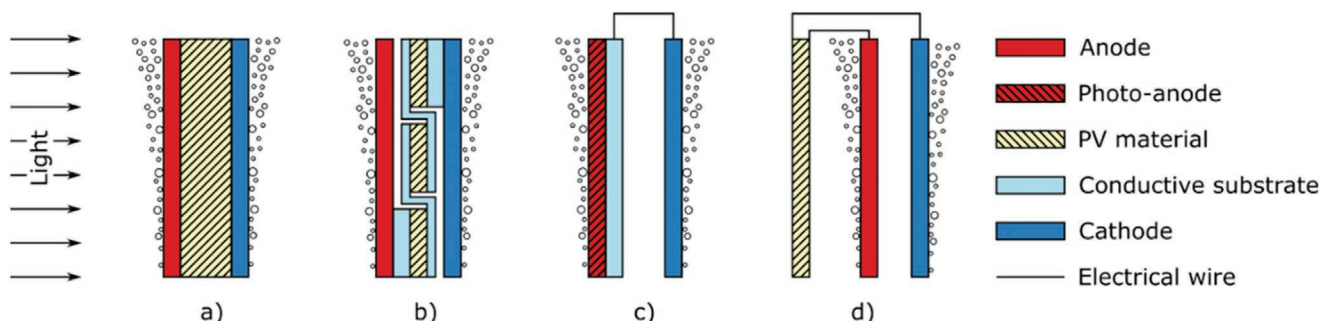


Figure 24. Examples of electronic connections: a) wireless monolithic, b) wired monolithic, c) monopolar PEC, and d) monopolar PV + E.^[304] Reproduced with permission.^[304] Copyright 2019, Scrivener Publishing LLC.

achievable efficiency,^[139,140,325] ii) electrical configuration of photoabsorbers, examples of which are shown in **Figure 24**, and iii) system optics and optical connection of photoabsorbers. The total bias generated by a device also depends on the type of junctions associated with the photoabsorbers, which can be solid state junctions (a p–n heterojunction or several stacks thereof, or heterojunctions between several n-type or several p-type materials) or semiconductor | liquid (or gas) junctions. Optical configurations become progressively more important and variable as the number of photoabsorbers in the system increases. Irradiation of photoabsorbers with different band-gaps in series enables a greater utilization of photons with wavelengths in the UV and visible range, while irradiation in parallel enables better performances of materials with similar bandgaps. In practice, various permutations of series and parallel optical pathways are possible. The maximum achievable η_{STH} of a given system will depend on the limits imposed by the number of photoabsorbers and the electrical and optical connections; the conceptual abstraction associated with these three considerations enables a fundamental comparison of devices, though not taking into account the actual engineering.

The materialization of a conceptual design into a physical system requires decisions to be made regarding electrode dimensions, the physical placement of all system components relative to each other and the light source, choice of electrolyte and any flow regime, optical arrangements, and product separation and harvesting. Any elements of a design that will constrain the engineering and performance of an up-scaled device need to be identified a priori. For example, components such as the membrane (or absence thereof) or optical elements, such as mirrors or Fresnel lenses, can restrict the device geometry such that all of the remaining components have to be designed and optimized around these central features. Therefore, the overall true performance of any device cannot be based solely on material studies; system engineering must be accounted for, as is the case with electrolyzers and PV installations.

Upon scale-up, several phenomena can impose particularly severe constraints on device performance, but these have been largely overlooked due to the rudimentary design and small size of most PEC reactors explored to date. In this review, we address specific phenomena and problems that are especially apparent from the device designs published so far: i) effect of suboptimal electrode orientations, ii) effect of low substrate

conductivity on inhomogeneities of reaction rates across the (photo)electrode surfaces, and iii) effect of bubble evolution on optical losses, overpotential losses, and mass transport. We note that an excellent recent report on the many PEC devices that have been reported to date, both lab scale and pilot plant scale, is already available.^[299] Hence, here we focus specifically on the technical descriptions of challenges associated with some of these designs. Due to the absence of standardized benchmarking procedures and reporting standards for PEC devices, as well as the difficulty in deconvoluting the contributions of the various scale-up-related loss processes to system efficiency, quantitative comparisons between published systems have been mostly omitted in this section.

4.2. Principal Phenomena Affecting the Performance of Up-scaled PEC Systems

4.2.1. Effect of Electrode Orientation

As shown in Section 1.1, in commercial electrolyzers, the electroactive surfaces of the anode and cathode are parallel and face toward each other, leading to a largely uniform electric field between them. This is illustrated in **Figure 25a**. Uniformity of the electric field results in a uniform ionic current, which is very important for ensuring the homogeneous distribution of the reaction rates across the electrode surfaces. However, Figure 22 shows 14 integrated device designs for solar hydrogen production and in seven of these (Designs 2, 3, 4, 6, 7, 8, and 9), the (photo)electroactive surfaces face away from each other by 180° or 360°. The effect of such orientations on the electric field distribution between the electrodes and the resulting current density profiles along the (photo)electrode lengths is shown schematically in 2D in **Figure 25b,c** for the 180° or 360° conditions, respectively. Even the intermediate case in **Figure 25b** has been shown experimentally and computationally to result in regions of inactive electrode surface area, the effect becoming more pronounced with decreasing ionic conductivity of the electrolyte and increasing ionic path length (determined by the electrode size).^[134] In general, increased integration leads to increased ionic resistance and losses.^[326] It is tempting to think that such effects will not be pronounced at the low current densities (of order 1 mA cm⁻²) that are typical of PEC systems (in contrast to commercial electrolyzers, where the current

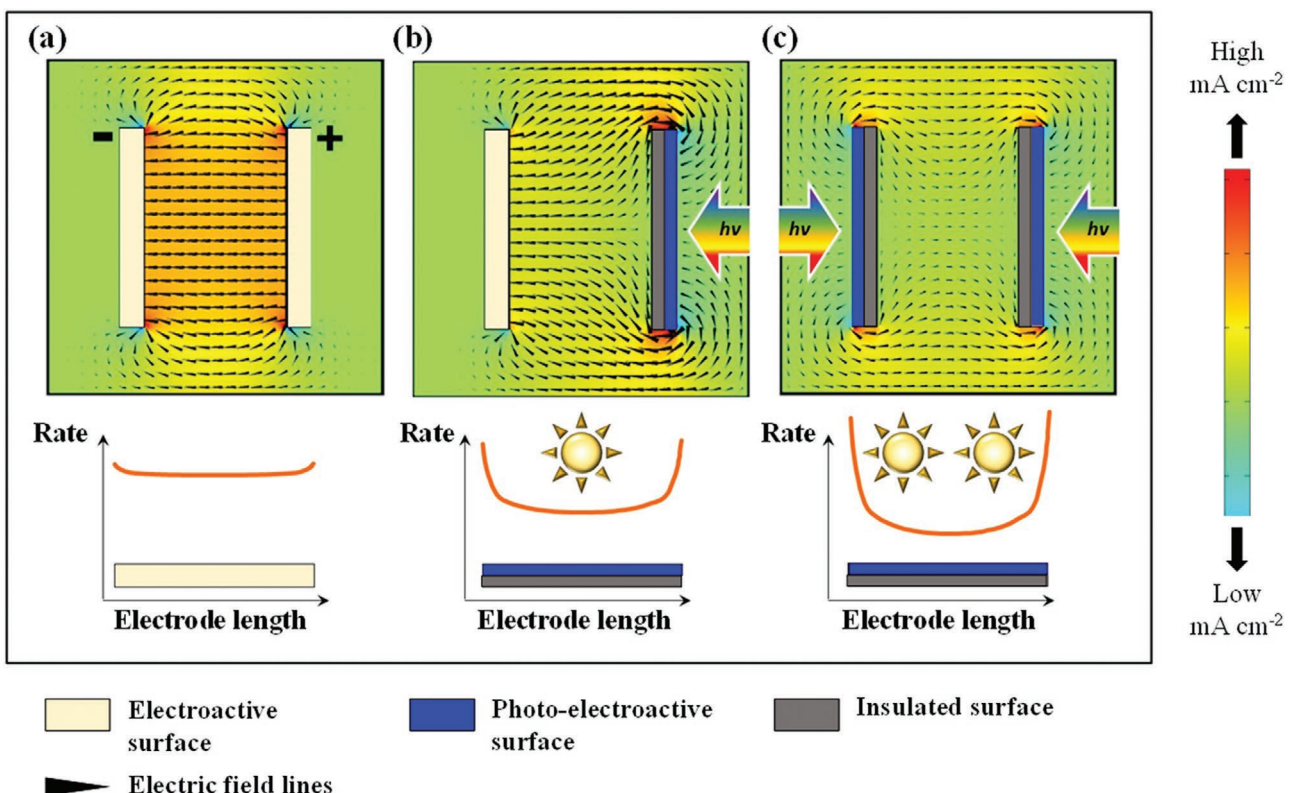


Figure 25. 2D representation of the relative impacts of (photo)electroactive surface orientations on current density and reaction rate distributions: a) electroactive surfaces face parallel to each other, as they do in alkaline and PEM electrolyzers, b) one (photo)electroactive surface faces away from the other in order to enable front illumination as in Designs 2, 6, 8, and 9 in Figure 22, and c) both (photo)electroactive surfaces face in opposite directions as in Design 4 in Figure 22. The electric field arrow dimensions are sized logarithmically with current magnitude. Simulations were performed using COMSOL Multiphysics with Secondary Current Distributions to produce schematic illustrations of macroscopic effects, which will invariably affect the performance of up-scaled reactors.

density is several orders of magnitude higher). However, charged species take the path of least resistance and hence no current density is too small for these effects to be irrelevant.

Two designs in Figure 22 (Designs 3 and 7) utilize a perforated electrode, which can be imagined as a planar electrode that has been punctured to create an array of millimeter- or micrometer-sized holes. The purpose of the holes is to create ionic shortcuts, thereby homogenizing the electric field and the electrode current density.^[134,315,327,328] The perforated design has mostly been used as a proof of concept – to illustrate the significance of ionic path lengths on the overall (photo) electrochemical reaction rates. However, in practice, perforated structures would be vulnerable to degradation via corrosion, which would be caused by the inevitable exposure to the electrolyte of the electrode substrates and any other material layers used for creating junctions for improved charge separation.

Of the 14 devices shown in Figure 22, a further two designs (Designs 10 and 11) have the (photo)electroactive surfaces positioned side by side (also facing away from each other by 180° but in a different arrangement to Design 2). **Figure 26** shows that this arrangement also results in severe inhomogeneities. Comparisons between Figure 26a,b show the direct effect of reorientating two electroactive surfaces from facing each other (optimal scenario) to facing in the same direction. Subsequently, any increase in electrode length will not result in

any practical increase in product flux. A similar effect would be observed on electrodes positioned at 90° relative to each other. The situation improves as the electrolyte conductivity increases (difference between Figure 26d,e), however, there will be a practical limit on this parameter.

There is no uncertainty that suboptimal geometric orientations of (photo)electroactive surfaces will prohibit effective device scale-up and hence, this should be one of the primary considerations in reactor design.

4.2.2. Effect of Photoelectrode Substrate Resistivity

Conducting oxides, such as FTO, are used ubiquitously as photoelectrode substrates. Their principal advantages are that they i) are transparent, thereby enabling front and back illumination of the overlying photoelectrodes, ii) form adequate junctions with overlying semiconducting materials, and iii) exhibit very poor HER or OER kinetics such that their contribution to PEC measurements can be largely excluded. The transparency of such oxides also enables their use in tandem photoelectrodes and PV cells and has been crucial in enabling more optimal electrode arrangements so as to obviate the effects described in Section 4.2.1. The major disadvantage of FTO is its high resistivity and it could never be used in commercial electrolyzers.

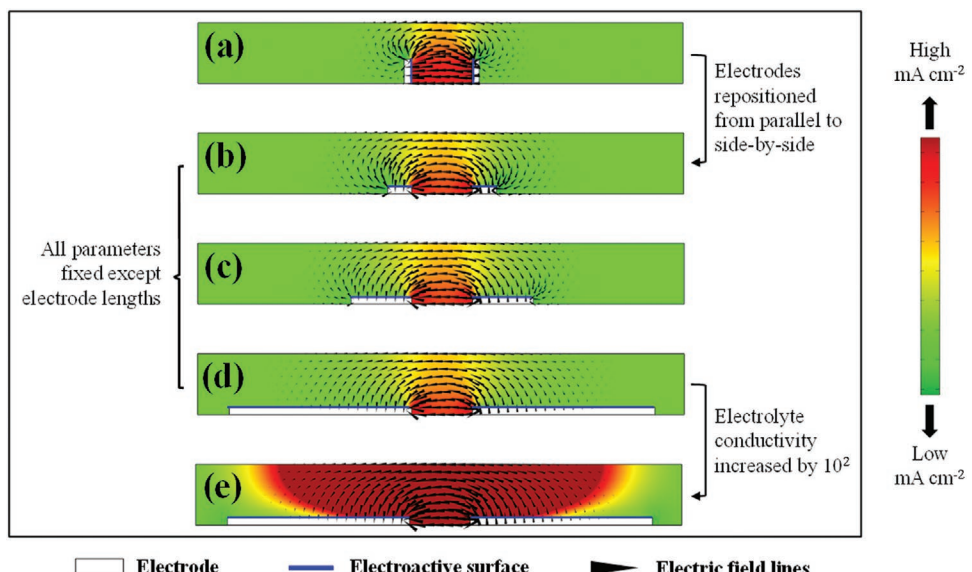


Figure 26. 2D representation of the impacts of (photo)electroactive surface dimensions when positioned side-by-side, as shown in Designs 10 and 11 in Figure 22. a,b) A direct comparison of the impact of change in orientations of two identical sets of electrodes from parallel to side-by-side is enabled; b–d) the effect of increase in electrode lengths on the current density distributions is shown, and e) the same system as in (d) is shown, but with the electrolyte conductivity increased by 2 orders of magnitude. The electric field arrow dimensions are sized logarithmically with current magnitude. Simulations were performed using COMSOL Multiphysics with Secondary Current Distributions to produce schematic illustrations of macroscopic effects, which will invariably affect the performance of up-scaled reactors.

The negative effect of the FTO substrate on the performance of up-scaled photoelectrodes has been demonstrated unambiguously.^[95,192,305,324,329] Numerical simulations, shown in Figure 27, have quantified the potential drops across a 2D FTO surface as a function of current density. The drops are significant, even when the potential is applied along the entire electrode length and on both sides of the electrode (as opposed to point contacts via a crocodile clip that often suffices for small electrodes). These findings are supported by experimental data and two strategies are being adopted to avoid these losses and facilitate a more effective scale-up: i) addition of a conductive “grid” between the FTO and overlying semiconductor, such as that shown in Figure 27d^[95] and ii) employment of modular electrode arrangements, such as that shown in Figure 27e.^[324] Option (i) requires the right balance to be found between improvements to the reaction rate homogeneity at the electrode surface (impacted by the phenomenon shown schematically in Figure 27c) and optical blockage from the metal grid. While option (i) introduces additional steps into the photoelectrode synthesis process, option (ii) increases the complexity of reactor design. However, modular electrode systems could be designed judiciously to enable efficient mass transport, as well as to decrease the impact of any single underperforming photoelectrode on the overall reaction rate.^[324]

4.2.3. Effect of Bubble Evolution

An observation of vigorous bubble evolution at a photoelectrode can bring immense joy, for it usually means a high gaseous product generation rate and, implicitly, a high η_{STH} . However, the evolution of bubbles introduces a plethora of changes,

which impact on one another and can be challenging to deconvolute, especially in a dynamic system. These changes can be broadly divided into optical, mass transport, Ohmic, and kinetic.^[330]

Optical effects introduced by bubbles directly impact photoelectrode performance in the cases of front-side illumination, because they limit the transmission of incident light to its surface through the electrolyte. This is illustrated in Figure 28. Depending on the mode of photoelectrolysis operation, light may propagate through a flowing two-phase bubbly mixture and/or through bubbles adhering to an electrode surface, as shown in Figure 28c,d, respectively.^[331,332] At every gas | liquid interface through which the light passes, it may undergo reflection, scatter, or refraction, leading to losses in transmitted light.

It was determined from single bubble studies in a quiescent system where any kinetic and Ohmic effects were minimized, that the growth of a bubble from 150 to a 1000 μm diameter can directly result in a photocurrent density decrease from 2% to 23%, respectively.^[332] Using videographic imaging, it is possible to correlate optical losses on transparent substrates with current density, as well as to determine the bubble number density, velocity distribution of bubbles, and bubble radius distribution.^[331] However, optical losses in real systems will be impacted by bubble dynamics, to which many different conditions can contribute. In general, the whole bubble evolution process comprises several steps, as shown in Figure 29a, and the theory of which is described by Angulo et al.^[330] The evolution of bubbles, their growth and detachment from the surface or coalescence into larger bubbles, is highly sensitive to the properties of the interface and conditions such as temperature and pressure.^[331,333] Delayed detachment leads to an increase in bubble size. It has been observed in multiple

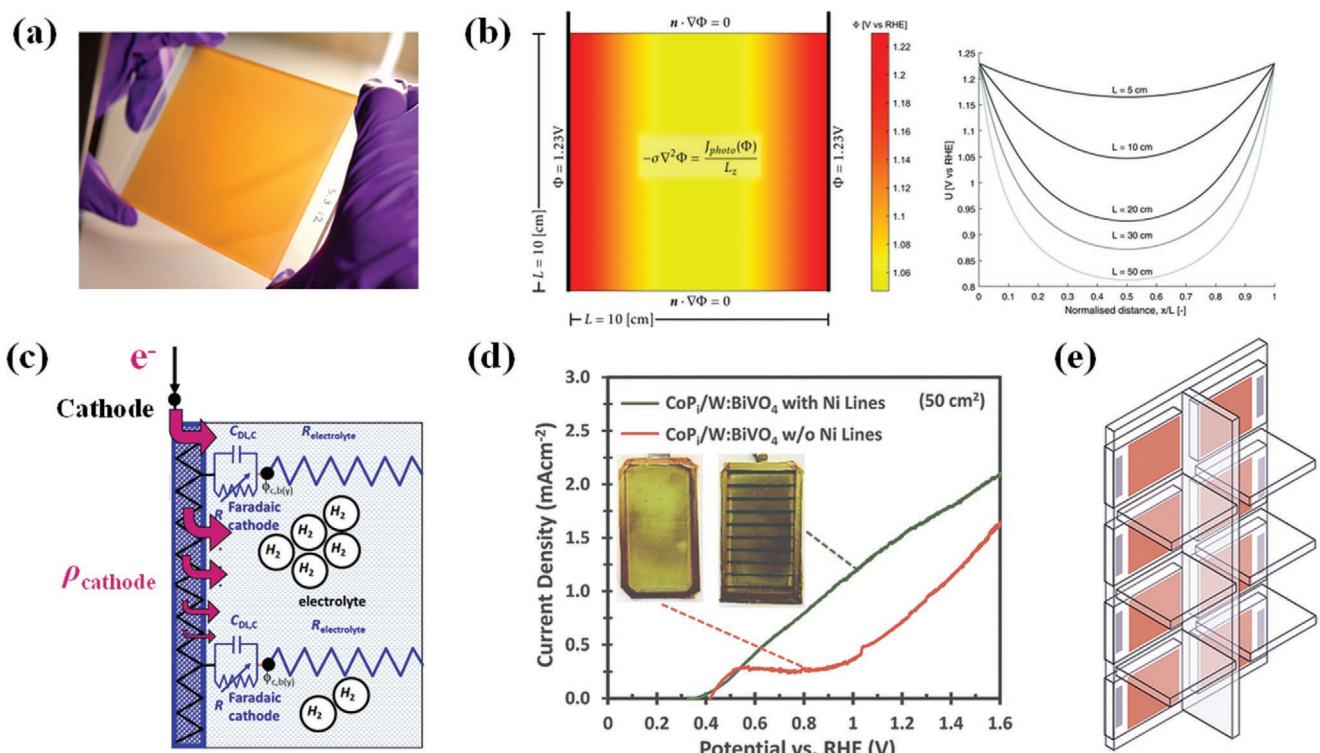


Figure 27. a) A 10 cm × 10 cm hematite thin film spray pyrolyzed onto a FTO substrate; b) simulated potential drops across a 10 cm × 10 cm FTO electrode and normalized potential drops for FTO electrodes of lengths in the range 5–50 cm; c) schematic representation of relative electronic flow through a highly resistive material, impacting reaction rates across the electrode length; d) the homogenizing effect of electronically conducting Ni strips on the potential distribution across a BiVO₄ photoelectrode and impact on measured photocurrent density; and e) modular photoelectrode. (b) Reproduced with permission.^[329] Copyright 2018, Royal Society of Chemistry; (d) Reproduced with permission.^[95] Copyright 2019, Royal Society of Chemistry; (e) Reproduced with permission.^[324] Copyright 2018, Elsevier B.V.

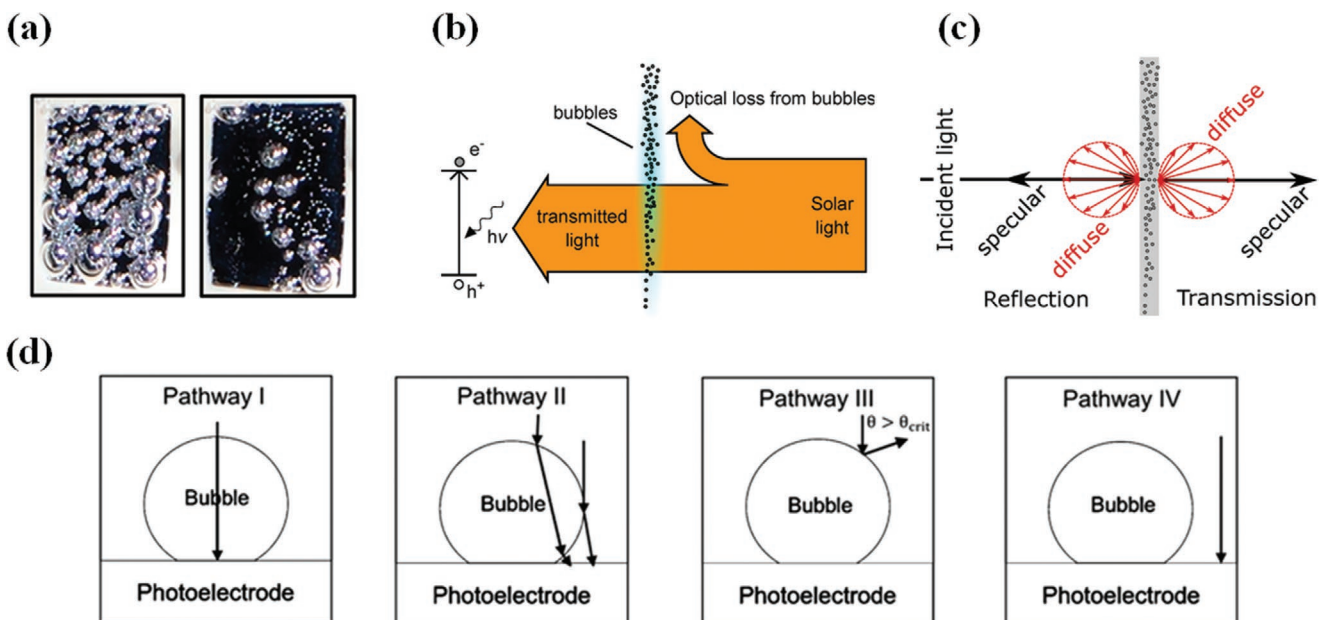


Figure 28. a) Photographic image of bubble-covered photoelectrode surface, b) high level schematic of the impact of bubbles on light transmission to the electrode surface, c) optical loss mechanisms in a rising bubbly mixture of liquid and gas, and d) different optical pathways that are likely to occur for a bubble bound to a photoelectrode surface. (a) and (d) Reproduced with permission.^[332] Copyright 2017, American Chemical Society; (b) and (c) Reproduced with permission.^[331] Copyright 2019, American Chemical Society.

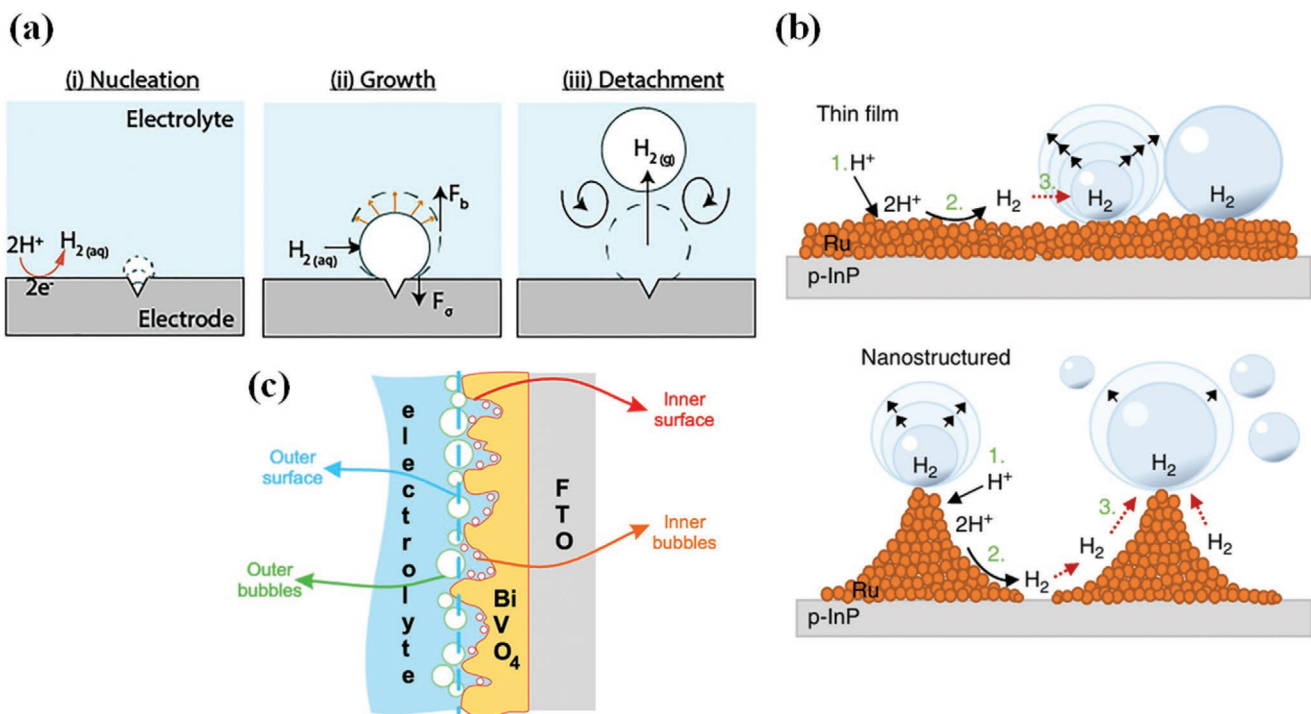


Figure 29. a) Schematic illustration of the three principal stages of bubble evolution: 1) nucleation, 2) growth, and 3) detachment from a gas evolving electrode surface; b) cross-sectional illustration of a gas bubble evolution model on a thin-film and nanostructured photoelectrode; c) schematic of a gas bubble evolution model on a nanostructured thin-film photoelectrode, illustrating the spatial distributions in bubble dimensions away from the innermost surface. (a) Reproduced with permission.^[330] Copyright 2020, Elsevier Inc.; (b) Reproduced under the terms of the Creative Commons Attribution-Non-Commercial license.^[334] Copyright 2018, Springer Nature; (c) Reproduced with permission.^[336] Copyright 2015, American Chemical Society.

studies that limiting bubble growth, and the resultant decrease in active site blockage, is facilitated by nanotextured surfaces, as shown schematically in Figure 29b. For example, studies of PECs in microgravity, aimed at understanding their potential in extraterrestrial applications, have shown that in the absence of buoyancy, bubble detachment is facilitated by photoelectrode nanostructure, while flat photoelectrodes promote coalescence of bubbles into froth layers on the electrode surface.^[334] The proposed influence of nanostructure was to enhance the electric field at the tips of any protrusions relative to a flatter surface, resulting in high localized current densities and bubble generation rates; bubbles growing at the tips of protrusions therefore have much greater contact angles, leading to easier detachment. In addition to contributing to optical losses, prolonged adhesion of bubbles to the electrode surface with a low contact angle results in the blockage of active surface sites and decreased (photo)electrochemical reaction rates. A study of bubble evolution on microwire arrays oriented against gravity found that an electrode surface structured in this way enables the removal of bubbles by capillary forces and limits their departure diameter.^[335] Microwires with a decreased tip radius would further enhance bubble removal rates due to the increased contact angle; therefore the micro- and nanostructures being developed to increase PEC performance will also serve the purpose of promoting gas bubble removal. However, porous microstructures, while offering a high specific surface area, suffer from a degree of electrode reaction site blocking during bubble evolution, as shown experimentally, and described computationally using a surface blocking factor function.^[336]

In general, bubble adhesion to the electrode surface has a negative effect on electrode performance. Table 2 summarizes the contribution of bubbles to three overpotentials, which collectively contribute to the potential drop across the (photo)electrochemical reactor.^[330,337] In addition to the obvious negative impact of reaction site blockage by bubbles on increasing the activation overpotential, bubbles, which can be thought of as small insulators, distort and elongate ionic pathways, resulting in increased Ohmic drop. The impact of bubbles on the Ohmic drop is considerably smaller than for commercial electrolyzers, which operate at current densities that are several orders of magnitude greater (>200 mA cm⁻²). However, the suboptimal electrode orientations can compromise this otherwise small loss, as shown in Figures 25 and 26. Finally, in the case of photoelectrodes,

Table 2. Summary of possible bubble-induced effects on each of the overpotential components in an electrochemical gas-evolving system. Reproduced with permission.^[330] Copyright 2020, Elsevier Inc.

Overpotential component	Typical effect of bubbles
Activation	Attached bubbles increase the overpotential due to masking of the electrodes and decrease of the effective electrocatalytic area
Ohmic	Attached and free bubbles increase the overpotential due to a blockage of the ion pathways available for current transport
Concentration	Bubbles may decrease the concentration overpotential by absorbing dissolved gas products and decreasing supersaturation levels in the electrolyte

prolonged bubble adhesion could lead to rapid degradation.^[338] For example, a large bubble of hydrogen contacting the photoelectrode surface could generate a localized reversible potential that is different to the bare electrode surface that contacts the electrolyte; this local distortion could cause localized corrosion.

One positive impact of bubble evolution is the enhancement of mass transport in the vicinity of the electrode surface, which usually results in increased current densities and vice versa.^[330,339,340] This enhancement is due to bubble evolution disturbing the diffusion layer that otherwise develops in quiescent solutions and grows with the square root of time.^[341] Forced convection, such as that delivered by pumping the electrolyte along the electrode surface (or through it, in the case of perforated electrodes), has two simultaneous effects of increasing mass transport to/from the electrode surface and increasing bubble removal rates. Electrolyte flow will most likely be necessary in up-scaled PEC reactor installations in the same way that it is required in alkaline and PEM electrolyzers; in such scenarios, it could have an additional benefit of being a medium for excess heat removal, preventing the photoabsorbers from overheating (the electrolyte in PEC systems will replace the role of the active cooling medium in PV installations, described in Section 1.2). However, in terms of electrolyte convection impact on bubble dynamics and the combined two-phase flow distribution, a lot depends on the current density, the size of generated bubbles, the electrolyte flow rate, the geometry of the channel through which the flow progresses, and even the chemical composition of the electrolyte.^[340,342] In cases when the bubble volume fraction and the resulting bubble–bubble interactions become significant, for example, in a narrow channel at high gas evolution rates, increases in drag become important.^[343] The latter phenomenon will of course impact the bubble residence time in front of a photoelectrode surface and affect optical losses. Furthermore, the size of the bubbles and the current density at which they are evolved can determine the two-phase flow regime. The flow regime can transition from quasi-steady, to transitional, to pseudo-turbulent as bubbles' size decreases and their evolution rate increases.^[340]

All these points considered, it is very difficult to tackle any particular bubble-associated loss mechanism individually, since many phenomena are intrinsically interconnected. A successful device with relevance to industry can only be designed and optimized with all effects considered, including electrode surface microstructure and texture, electrolyte flow, electrode orientation (relative to gravity and electrolyte flow), and reactor geometry. The expected impact of these parameters on bubble size and residence time on optical losses needs to be well understood. Consideration would also need to be given to any hourly changes in PEC reactor tilt that may be imposed in an analogous manner to PVs mounted on tracking systems. Tilt is expected to impact on the buoyant force that causes bubble uplift as well the two-phase flow field and so, its impact on any PEC reactor performance will require study.^[332]

4.3. Constraints to the PEC Reactor Design Imposed by System Components

Commercial electrolyzers utilize electrodes with geometric areas ranging from several hundred to tens of thousands centimeters

squared, as discussed in Section 1.1. This is possible principally because i) the electrode geometries and orientations enable a uniform electric field distribution between the anode and the cathode and ii) current feeders are thick metallic plates and not semiconductors or highly resistive thin films, thereby limiting the severe Ohmic losses discussed in Section 4.2.2. It is therefore reasonable to conclude that PEC reactors will utilize smaller electrodes and will be more modular in nature; indeed, this is the trend observed to date. However, excessive modularity will have the effects of i) increasing the amount of materials used in reactor construction, since each reactor module will require its own electrolyte circuitry, gas manifolds, and so on, and ii) increasing the difficulty of making electronic contacts between each small electrode in a manner that does not leave the contact areas susceptible to degradation.

The drawbacks of modularity can be lessened by concentrating the incident light, thereby increasing the photocurrent density (provided the photoelectrode components do not degrade under such conditions). There may also be an associated cost benefit, especially where the chosen semiconductor is expensive (such as III–V materials). Several systems operating under concentrator light have been reported.

A system utilizing hematite photoanodes and silicon heterojunctions in a tandem configuration, operating under forced electrolyte convection, has been tested under natural light that was concentrator by a factor of up to ≈ 20 , as shown in Figure 30.^[193] The system utilized linear mirrors mounted on a two-axis tracking platform and demonstrated promising performance with average photocurrent density output in the range $0.5\text{--}2 \text{ mA cm}^{-2}$, depending on the exact configuration of the electrodes.

In a different system, III–V solar cells were thermally and electrically integrated with a PEM electrolyzer and irradiated with light delivered by a high-flux solar simulator shown in Figure 31a. The system, shown in Figure 31b, was able to perform under irradiances of up to 47.4 W cm^{-2} .^[322,345] Aqueous reactant flowed over the surface of the PV, absorbing a fraction of the generated heat, before being supplied to the anode compartment of the electrolyzer; at the same time, the anode was in thermal contact with the PV cells, and this combined mode of thermal integration increased the overall solar to hydrogen conversion efficiency. This system achieved η_{STH} of $\approx 15\%$ under a light concentration factor of 474, with the PV cells delivering 6000 mA cm^{-2} and electrolyzer delivering 888 mA cm^{-2} . This lab-scale prototype is now being developed into a commercial-scale pilot demonstrator, in which the integrated PV–electrolyzer system will be positioned at the focal point of a 7 m diameter parabolic dish concentrator, mounted on a dual-axis tracking system, for co-generation of chemical (H_2), electrical, and thermal energy.^[346] One of the motivations of decoupling the photoabsorbing and electrochemical elements physically was to avoid the utilization of semiconductor | liquid junctions, which remain prone to degradation and would be less likely to sustain long-term exposure to highly concentrator radiation.^[338] However, the adoption of light concentrators is clearly not limited to PV + E systems and could be used with PEC reactors employing inorganic semiconductor | liquid junctions, given appropriate reactor designs and thermal management.^[320,347]

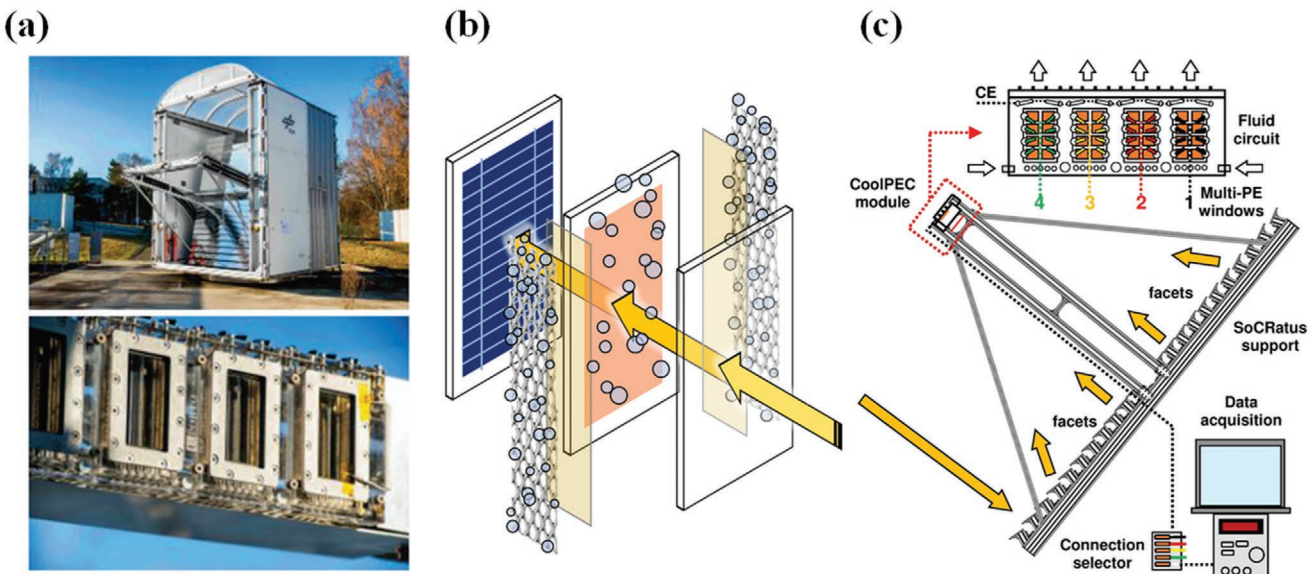


Figure 30. a–c) Modular PEC system utilizing hematite photoanodes (50 cm^2 per module) and two-heterojunction silicon PVs in a tandem configuration, mounted on a dual-axis tracking system for operation outdoors under concentrator light of up to 12.8 kW m^{-2} .^[193,344] (a) Reproduced with permission.^[344] Copyright 2018, Springer Science Business Media LLC; (b) and (c) Reproduced with permission.^[193] Copyright 2020, Elsevier B.V.

Modularity can potentially also enable the adoption of devices without a membrane, where the gaseous products are separated by forced convection, and therefore decrease the capital cost of the system.^[323,348,349] The separation efficiency will depend heavily on the hydrodynamics and dimensions of the flow channels between the electrodes. However, the feasibility of using a series of mini-module PEC devices without a membrane operating under forced convection is yet to be demonstrated.

In summary, accelerated efforts in PEC reactor prototype development are required in order to bring these systems closer to commercialization. Ways for avoiding major losses associated with suboptimal orientation of (photo)electroactive surfaces relative to each other, high material resistivity, and complications due to bubble evolution must be explored more proactively. Furthermore, reactor design should be supplemented with numerical models of: 1) Microkinetics – the prediction of photocurrent generated by a chosen combination of materials as a function of light intensity;^[134,313,350–355] 2) macrokinetics – accounting for the spatial distributions of electrode kinetics, management of heat imparted by solar photons, changes in the chemical composition of the electrolyte, effect(s) of bubbles, product separation;^[110,134,313,314,326] 3) systems model – for determining the BoP required to support the operation of the PEC reactor, including the means by which the H_2 product is collected and transferred to energy storage systems;^[356,357] 4) techno-economic model – for determining how cost-effective the system is, given the combined set of parameters that characterize its performance (discussed in Section 5).

5. Future Directions

The development targets for PEC water splitting set by the U.S. DOE was to reach a leveled cost of hydrogen (LCOH)

of $\text{US\$}5.70\text{ kg}^{-1}\text{ H}_2$ in 2020, with the ultimate ambition of reducing the LCOH to $\text{US\$}2.10\text{ kg}^{-1}\text{ H}_2$.^[125] While these targets have not been met, they broadly help guide researchers and companies toward the technical and economic requirements to achieve a commercially viable technology. The cost of hydrogen produced today varies considerably depending on the technology. Currently, the lowest costs are achieved by fossil-fuel-based production techniques ranging from an average of $\text{US\$}1.28\text{ kg}^{-1}\text{ H}_2$ in steam methane reforming and up to $\text{US\$}2.24\text{ kg}^{-1}\text{ H}_2$ in biomass gasification.^[23] The reported costs from electrolysis routes vary widely across the literature, and are considerably more expensive than fossil-fuel-based options. Grid-connected systems are capable of producing a median LCOH of $\text{US\$}8.81\text{ kg}^{-1}\text{ H}_2$ in the US and $\text{US\$}13.11\text{ kg}^{-1}\text{ H}_2$ in the EU in 2020.^[358] For systems that are not grid connected, the cost of electrolysis ranges between $\text{US\$}1.95$ and $\text{US\$}17.30\text{ kg}^{-1}\text{ H}_2$.^[23] However, experience curves based on historical data suggest continued declines in the system price of electrolyzers.^[21] Following this trend, it has been recently demonstrated that wind power plants can produce hydrogen at prices as low as $\text{€}3.23\text{ kg}^{-1}\text{ H}_2$ in Germany and $\text{US\$}3.53\text{ kg}^{-1}\text{ H}_2$ in Texas, lower than previously reported in the literature for such systems.^[359]

Currently, solar electrolysis approaches are not economically viable for large-scale deployment. A recent literature review on low-carbon heat solutions for heavy industry suggests that hydrogen production using solar electrolysis costs roughly 50% more per unit energy of high-grade heat compared to hydrogen produced from PEM electrolysis using grid electricity.^[360] In 2013, PEC water splitting was simulated to achieve a LCOH between $\text{US\$}4.00$ and $\text{US\$}10.40\text{ kg}^{-1}\text{ H}_2$, albeit without considering the current limitations of material performance issues and scale-up.^[102] In 2016, another techno-economic analysis of PEC water splitting estimated a LCOH of $\text{US\$}9.20\text{–}\text{US\$}11.40\text{ kg}^{-1}\text{ H}_2$ using market indicators and assumptions in

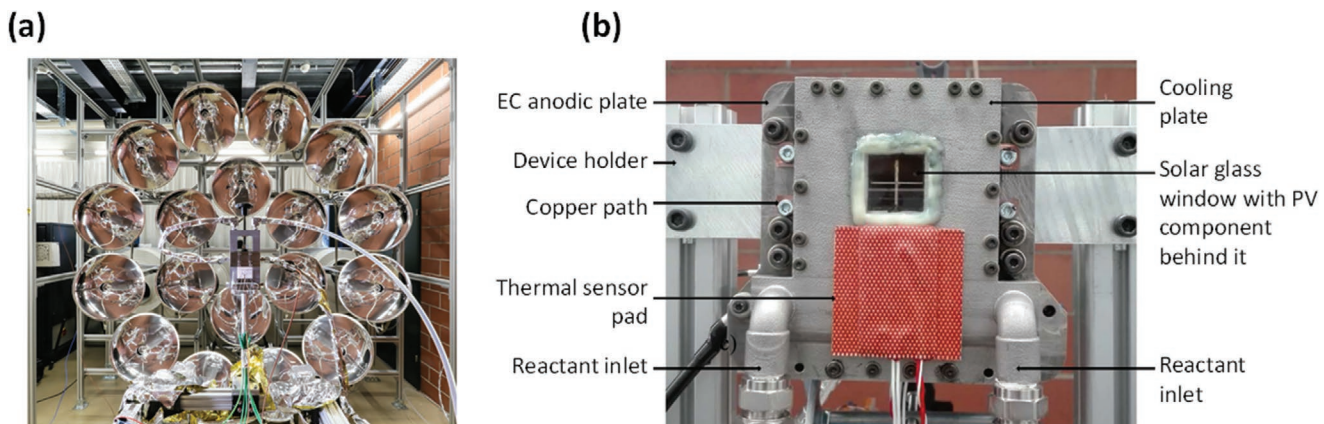


Figure 31. a) High-flux 45 kW_{el} solar simulator capable of delivering an irradiance of up to $\approx 21.7 \text{ MW m}^{-2}$ ^[345] and b) photograph of the integrated PV-electrolyzer assembly.^[322] (a) Photograph courtesy of Sophia Haussener, Laboratory of Renewable Energy Science and Engineering (LRESE), EPFL; (b) Reproduced with permission.^[322] Copyright 2019, Springer Nature.

the US.^[137] In 2020, more recent estimates of the LCOH for an off-grid PV-E system and a PEC system was estimated to be US\$6.22 kg⁻¹ H₂ and US\$8.42 kg⁻¹ H₂, respectively.^[361] Results from these studies suggest that PEC hydrogen systems are not currently cost-competitive with existing alternatives in the market. One primary driving force to deploy disruptive technologies, such as PEC hydrogen systems, would be economic considerations and much research is focused on how to make these systems less expensive to produce.

One means of achieving economically competitive solar electrolysis systems is to develop systems with high η_{STH} . For meeting its cost targets, DOE has set the η_{STH} target of 20% by 2020 and an ultimate value of 25%.^[125] The highest demonstrated η_{STH} of solar electrolysis systems have been 24.4%, by combining concentrator photovoltaic (CPV) modules with triple-junction cells and PEM, and 30%, by combining triple-junction solar cells with two series-connected PEM.^[362,97] Solar electrolysis systems could potentially achieve higher η_{STH} , but these studies demonstrate the potential of solar electrolysis systems to produce hydrogen at efficiencies approaching the theoretical limit. The main challenge is achieving a sufficiently high η_{STH} , while also meeting other system performance targets, such as PEC cell life span. Similar to PV installations, even highly efficient PEC systems will have a long payback period.^[363] Moreover, a successful PEC module should not only show high η_{STH} , but also show high hydrogen production rate capability. The land use by these modules may also be a limiting factor to their deployment, especially with competition from solar PV and cultivating bioenergy crops in upcoming decades.

Up-to-date system costs for solar electrolysis are rare in the literature. The technology is still in its infancy, and the lack of reliable and readily available information is understandable. However, cost estimates and frequent updates on cost projections help researchers to make better predictions on the future of a technology. Such reviews and projections also make comparative and critical studies of electrolysis technologies possible. For improving these projections, there is a need for more experimental data from up-scaled systems, hence, engineering work for scaling up existing systems is urgent and crucial. In addition to demonstrating larger scale systems, another challenge is manufacturing modules that provide reliable per-

formance for long durations. Currently, lifetime testing of PEC cells beyond 48 h is not usually reported.^[156,364] Data on system lifetime would support reliable techno-economic analyses for PEC systems based on realistic lifetime projections. After η_{STH} , the PEC cell life span has been shown to be the most significant parameter in life cycle energy balance of a PEC system.^[365] Ensuring a stable performance over the extended lifetime of a PEC cell is crucial for the commercial deployment of this technology. Hence, it is also important to develop standardized lifetime testing of PEC cells to serve as a reference point between different prototypes that are currently being developed. The importance of establishing a standard set of measures and methods has been discussed,^[138] but this now needs to be expanded to include more robust experimental guidelines. The future development of PEC devices would greatly benefit from additional discussion and the establishment of standardized methodology for their testing, akin to the international standards organisation (ISO) methodology that has been developed for photocatalytic air remediation technologies.^[366]

The amount of energy required for the manufacturing of PEC cells would be another critical consideration before PEC modules can be commercially deployed. A fundamental system requirement for PEC cells is to provide substantially more energy in the form of hydrogen energy than the total energy investment that goes into their manufacture and end-of-life recycling. Having a relatively low energy footprint is important in order to effectively mitigate atmospheric CO₂ emissions. Water electrolysis driven by renewables has been shown to be favorable in comparison to several other alternatives in terms energy required to abate a unit of CO₂ emissions.^[367] PEC modules should be able to achieve a similar performance to be considered a viable CO₂ mitigation technology. Currently, the fabrication of active cell components is estimated to be the largest energy input into the manufacturing of a PEC module, and one of the main determinants in the net energy performance.^[363] Another major energy expenditure is the energy required to compress the hydrogen gas to elevated pressures for delivery, which can account for half of the annual energy balance of a PEC hydrogen production facility.^[365] The delicate structures of many PEC materials may not render them sufficiently mechanically robust to withstand elevated pressures as well as convection-enhanced mass

transport, though to our knowledge, pressurized PEC reactors have not been tested experimentally; hence, external compression currently seems unavoidable. In addition to reducing embedded energy requirements of PEC modules relative to the energy return they provide, a major challenge is to efficiently scale-up a manufacturing process from laboratory scale (<kilowatt production capacity) to commercial scale (>megawatt production capacity). While the manufacture of some components would be more efficient as the production is scaled due to the benefits of a large-scale and streamlined supply chain, the commercial production techniques for the photoabsorber layers should also achieve similar performance to what would be demonstrated in laboratory experiments. This can be challenging, since some of the techniques used in laboratory settings cannot be utilized to manufacture PEC cells at scale.

We are currently going through a massive transformation in our energy infrastructure toward decarbonization. Energy infrastructures can outlive many generations, and decisions that we take today will have a lasting impact in ultimately determining our success in mitigating the global climate crisis. Fuels like hydrogen, which can be produced using renewable energy, could directly replace fossil fuels, and be used in society without necessitating a radical change in existing energy infrastructures. Producing hydrogen directly from solar power can be an essential tool toward decarbonizing societies; with PEC water splitting being an enabling technology at this front. However, there are major materials and engineering challenges, which have been reviewed and discussed in this work, that must be overcome before PEC water splitting can fulfill this promise.

Acknowledgements

A.K. thanks the Imperial College for a Junior Research Fellowship, the EPSRC for a Capital Award Emphasizing Support for Early Career Researchers, and the Royal Society for an Equipment Grant (Grant No. RSG|R1|180434). O.B. thanks the Imperial College London for an Imperial College Research Fellowship. B.M. thanks the EPSRC for a doctoral training partnership.

Conflict of Interest

The authors declare no conflict of interest.

Keywords

hydrogen, inorganic photoelectrodes, photoelectrochemistry, reactor engineering, solar fuels

Received: October 16, 2020

Revised: December 10, 2020

Published online: February 25, 2021

[1] E. Hawkins, P. Ortega, E. Suckling, A. Schurer, G. Hegerl, P. Jones, M. Joshi, T. J. Osborn, V. Masson-Delmotte, J. Mignot, P. Thorne, G. J. van Oldenborgh, *Bull. Am. Meteorol. Soc.* **2017**, *98*, 1841.

- [2] J. E. Tierney, A. M. Haywood, R. Feng, T. Bhattacharya, B. L. Otto-Biesner, *Geophys. Res. Lett.* **2019**, *46*, 9136.
- [3] A. C. Ravelo, D. H. Andreasen, M. Lyle, A. O. Lyle, M. W. Wara, *Nature* **2004**, *429*, 263.
- [4] J. Rogelj, M. den Elzen, N. Höhne, T. Fransen, H. Fekete, H. Winkler, R. Schaeffer, F. Sha, K. Riahi, M. Meinshausen, *Nature* **2016**, *534*, 631.
- [5] S. B. Walker, U. Mukherjee, M. Fowler, A. Elkamel, *Int. J. Hydrogen Energy* **2016**, *41*, 7717.
- [6] E. S. Hanley, J. Deane, B. Ó. Gallachóir, *Renewable Sustainable Energy Rev.* **2018**, *82*, 3027.
- [7] *Hydrogen Roadmap Europe: A Sustainable Pathway for the European Energy Transition*, Fuel Cells And Hydrogen 2 Joint Undertaking, Brussels **2020**.
- [8] A. Sgobbi, W. Nijs, R. D. Miglio, A. Chiodi, M. Gargiulo, C. Thiel, *Int. J. Hydrogen Energy* **2016**, *41*, 19.
- [9] I. Staffell, D. Scamman, A. V. Abad, P. Balcombe, P. E. Dodds, P. Ekins, N. Shah, K. R. Ward, *Energy Environ. Sci.* **2018**, *12*, 463.
- [10] S. J. Davis, N. S. Lewis, M. Shaner, S. Aggarwal, D. Arent, I. L. Azevedo, S. M. Benson, T. Bradley, J. Brouwer, Y.-M. Chiang, C. T. M. Clack, A. Cohen, S. Doig, J. Edmonds, P. Fennell, C. B. Field, B. Hannegan, B.-M. Hodge, M. I. Hoffert, E. Ingersoll, P. Jaramillo, K. S. Lackner, K. J. Mach, M. Mastrandrea, J. Ogden, P. F. Peterson, D. L. Sanchez, D. Sperling, J. Stagner, J. E. Trancik, C.-J. Yang, K. Caldeira, *Science* **2018**, *360*, eaas9793.
- [11] T. Isaac, *Clean Energy* **2019**, *3*, 114.
- [12] P. E. Dodds, I. Staffell, A. D. Hawkes, F. Li, P. Grünewald, W. McDowell, P. Ekins, *Int. J. Hydrogen Energy* **2015**, *40*, 2065.
- [13] *Fuel Cells Bulletin*, Vol. 2018, Elsevier, Amsterdam **2018**, p. 4.
- [14] Q. Wang, in *Handbook of Climate Change Mitigation* (Eds: W. Y. Chen, J. Seiner, T. Suzuki, M. Lackner), Springer, New York **2012**.
- [15] IEA, *The Future of Hydrogen*, <https://www.iea.org/reports/the-future-of-hydrogen> (accessed: September 2020).
- [16] *Fuel Cells Bulletin*, Vol. 2020, Elsevier, Amsterdam **2020**, p. 4.
- [17] J. Artz, T. E. Müller, K. Thenert, J. Kleinekorte, R. Meys, A. Sternberg, A. Bardow, W. Leitner, *Chem. Rev.* **2017**, *118*, 434.
- [18] R. Phillips, W. J. F. Gannon, C. W. Dunnill, in *Electrochemical Methods for Hydrogen Production* (Ed: K. Scott), The Royal Society of Chemistry, London **2019**, pp. 28–58.
- [19] D. Bessarabov, P. Millet, in *PEM Water Electrolysis*, Academic Press (Elsevier), London **2018**, pp. 1–31.
- [20] T. Bystron, M. Paidar, T. Klicpera, M. Schuster, K. Bouzek, in *Electrochemical Methods for Hydrogen Production* (Ed: K. Scott), The Royal Society of Chemistry, London **2019**, pp. 59–93.
- [21] O. Schmidt, A. Gambhir, I. Staffell, A. Hawkes, J. Nelson, S. Few, *Int. J. Hydrogen Energy* **2017**, *42*, 30470.
- [22] S. Y. Ereev, M. K. Patel, *J. Bus. Chem.* **2012**, *9*, 31.
- [23] B. Parkinson, P. Balcombe, J. F. Speirs, A. D. Hawkes, K. Hellgardt, *Energy Environ. Sci.* **2018**, *12*, 19.
- [24] L. Bertuccioli, A. Chan, D. Hart, F. Lehner, B. Madden, E. Standen, Study on Development of Water Electrolysis in the EU, **2014**.
- [25] J. Rossmeisl, Z.-W. Qu, H. Zhu, G.-J. Kroes, J. K. Nørskov, *J. Electroanal. Chem.* **2007**, *607*, 83.
- [26] H. Wendt, G. Iamarisio, *J. Appl. Electrochem.* **1988**, *18*, 1.
- [27] R. W. Revie, *Uhlig's Corrosion Handbook*, Wiley, Hoboken, NJ **2011**.
- [28] C. Xiang, K. M. Papadantonakis, N. S. Lewis, *Mater. Horiz.* **2016**, *3*, 169.
- [29] K. Zeng, D. Zhang, *Prog. Energy Combust. Sci.* **2010**, *36*, 307.
- [30] A. J. Bard, R. Parsons, J. Jordan, *Standard Potentials in Aqueous Solutions*, Marcel Dekker, New York **1985**.
- [31] J. Kibsgaard, I. Chorkendorff, *Nat. Energy* **2019**, *4*, 430.
- [32] G. Ozin, *Advanced Science News*, John Wiley & Sons, Hoboken, NJ **2021**.
- [33] J. K. Nørskov, T. Bligaard, A. Logadottir, J. R. Kitchin, J. G. Chen, S. Pandelov, U. Stimming, *J. Electrochem. Soc.* **2005**, *152*, J23.
- [34] B. E. Conway, J. O. Bockris, *J. Chem. Phys.* **1957**, *26*, 532.

- [35] A. J. Appleby, M. Chemla, H. Kita, G. Bronoel, *Encyclopedia on Electrochemistry of the Elements*, Marcel Dekker, New York **1982**.
- [36] D. M. F. Santos, C. A. C. Sequeira, J. L. Figueiredo, *Quim. Nova* **2013**, *36*, 1176.
- [37] S. J. D. V. Stralen, W. M. Sluyter, *J. Appl. Electrochem.* **1985**, *15*, 527.
- [38] M. M. Bakker, D. A. Vermaas, *Electrochim. Acta* **2019**, *319*, 148.
- [39] N. Nagai, M. Takeuchi, T. Kimura, T. Oka, *Int. J. Hydrogen Energy* **2003**, *28*, 35.
- [40] R. Phillips, C. W. Dunnill, *RSC Adv.* **2016**, *6*, 100643.
- [41] I. Dedigama, P. Angeli, N. van Dijk, J. Millichamp, D. Tsaoilidis, P. R. Shearing, D. J. L. Brett, *J. Power Sources* **2014**, *265*, 97.
- [42] C. Immerz, M. Schweins, P. Trinke, B. Bensmann, M. Paidar, T. Bystroň, K. Bouzek, R. Hanke-Rauschenbach, *Electrochim. Acta* **2018**, *260*, 582.
- [43] J. O. Majasan, J. I. S. Cho, I. Dedigama, D. Tsaoilidis, P. Shearing, D. J. L. Brett, *Int. J. Hydrogen Energy* **2018**, *43*, 15659.
- [44] H. A. Miller, K. Bouzek, J. Hnat, S. Loos, C. I. Bernäcker, T. Weißgärber, L. Röntzscher, J. Meier-Haack, *Sustainable Energy Fuels* **2020**, *4*, 2114.
- [45] L. Xiao, S. Zhang, J. Pan, C. Yang, M. He, L. Zhuang, J. Lu, *Energy Environ. Sci.* **2012**, *5*, 7869.
- [46] J. R. Varcoe, P. Atanassov, D. R. Dekel, A. M. Herring, M. A. Hickner, P. A. Kohl, A. R. Kucernak, W. E. Mustain, K. Nijmeijer, K. Scott, T. Xu, L. Zhuang, *Energy Environ. Sci.* **2014**, *7*, 3135.
- [47] M. R. Kraglund, M. Carmo, G. Schiller, S. A. Ansar, D. Aili, E. Christensen, J. O. Jensen, *Energy Environ. Sci.* **2019**, *12*, 3313.
- [48] J. J. Kaczur, H. Yang, Z. Liu, S. D. Sajjad, R. I. Masel, *Front. Chem.* **2018**, *6*, 263.
- [49] Ö. F. Selamet, F. Becerikli, M. D. Mat, Y. Kaplan, *Int. J. Hydrogen Energy* **2011**, *36*, 11480.
- [50] M. Santarelli, P. Medina, M. Cali, *Int. J. Hydrogen Energy* **2009**, *34*, 2519.
- [51] J. C. Koj, A. Schreiber, P. Zapp, P. Marcuello, *Energy Procedia* **2015**, *75*, 2871.
- [52] A. Roy, S. Watson, D. Infield, *Int. J. Hydrogen Energy* **2006**, *31*, 1964.
- [53] O. Kraan, G. J. Kramer, M. Haigh, C. Laurens, *Joule* **2019**, *10*, 2286.
- [54] Y. Tachibana, L. Vayssieres, J. R. Durrant, *Nat. Photonics* **2012**, *6*, 511.
- [55] O. Morton, *Nature* **2006**, *443*, 19.
- [56] BP, "Statistical Review of World Energy," <https://www.bp.com/en/global/corporate/energy-economics/statistical-review-of-world-energy.html> (accessed: October 2020).
- [57] A. Louwen, W. van Sark, in *Technological Learning in the Transition to a Low-Carbon Energy System* (Eds: M. Junginger, A. Louwen), Elsevier, Amsterdam **2020**, pp. 65–86.
- [58] D. Gielen, F. Boshell, D. Saygin, M. D. Bazilian, N. Wagner, R. Gorini, *Energy Strategy Rev.* **2019**, *24*, 38.
- [59] A. Martinez-Gracia, I. Arauzo, J. Uche, in *Solar Hydrogen Production – Processes, Systems and Technology* (Eds: F. Calise, M. D'Accadia, M. Santarelli, A. Lanzini, D. Ferrero), Academic Press (Elsevier), London **2019**, pp. 113–149.
- [60] J. C. Lam, D. H. W. Li, *Int. J. Ambient Energy* **1998**, *19*, 187.
- [61] R. Marquez, V. G. Gueorguiev, C. F. M. Coimbra, *J. Sol. Energy Eng.* **2013**, *135*, 011017.
- [62] D. Yang, P. Jirutitijaroen, W. M. Walsh, *Sol. Energy* **2012**, *86*, 3531.
- [63] T. M. Y. Khan, M. Elahi M. Soudagar, M. Kanchan, A. Afzal, N. R. Banapurmath, N. Akram, S. D. Mane, K. Shahapurkar, *J. Therm. Anal. Calorim.* **2020**, *141*, 511.
- [64] S. Racharla, K. Rajan, *Int. J. Sustainable Eng.* **2017**, *10*, 72.
- [65] A. Z. Hafez, A. M. Yousef, N. M. Harag, *Renewable Sustainable Energy Rev.* **2018**, *91*, 754.
- [66] R. Eke, A. Senturk, *Sol. Energy* **2012**, *86*, 2665.
- [67] O. Perpiñan, E. Lorenzo, M. A. Castro, R. Eyras, *Prog. Photovoltaics* **2009**, *17*, 137.
- [68] W. Nsengiyumva, S. G. Chen, L. Hu, X. Chen, *Renewable Sustainable Energy Rev.* **2018**, *81*, 250.
- [69] "PVsyst photovoltaic software," <https://www.pvsyst.com/> (accessed: September 2020).
- [70] "PVGIS," https://re.jrc.ec.europa.eu/pvg_tools/en/ (accessed: September 2020).
- [71] "SunEarthTools," <https://www.sunearthtools.com> (accessed: September 2020).
- [72] C. Chang, *Advances in Solar Heating and Cooling*, (Eds: R. Z. Wang, T. S. Ge), Elsevier **2016**.
- [73] V. Sumathi, R. Jayapragash, A. Bakshi, P. K. Akella, *Renewable Sustainable Energy Rev.* **2017**, *74*, 130.
- [74] K. Shanks, S. Senthilarasu, T. K. Mallick, *Renewable Sustainable Energy Rev.* **2016**, *60*, 394.
- [75] S. Karella, T. C. Roumpedakis, in *Solar Hydrogen Production* (Eds: F. Calise, M. D'Accadia, M. Santarelli, A. Lanzini, D. Ferrero), Academic Press (Elsevier), London **2019**, pp. 179–235.
- [76] J. C. Miñano, P. Benítez, P. Zamora, M. Buljan, R. Mohedano, A. Santamaría, *Opt. Express* **2013**, *21*, A494.
- [77] P. Benítez, J. C. Miñano, P. Zamora, R. Mohedano, A. Cvetkovic, M. Buljan, J. Chaves, M. Hernández, *Opt. Express* **2010**, *18*, A25.
- [78] K.-T. Lee, Y. Yao, J. He, B. Fisher, X. Sheng, M. Lumb, L. Xu, M. A. Anderson, D. Scheiman, S. Han, Y. Kang, A. Gumus, R. R. Bahabry, J. W. Lee, U. Paik, N. D. Bronstein, A. P. Alivisatos, M. Meitl, S. Burroughs, M. M. Hussain, J. C. Lee, R. G. Nuzzo, J. A. Rogers, *Proc. Natl. Acad. Sci. USA* **2016**, *113*, E8210.
- [79] J. J. Michael, S. M. Iqbal, S. Inriyan, R. Goic, *Energy* **2018**, *148*, 605.
- [80] A. Royne, C. J. Dey, D. R. Mills, *Sol. Energy Mater. Sol. Cells* **2005**, *86*, 451.
- [81] L. Micheli, E. F. Fernández, F. Almonacid, T. K. Mallick, G. P. Smestad, *Sol. Energy Mater. Sol. Cells* **2016**, *153*, 164.
- [82] NREL, "Best Research-Cell Efficiency Chart," <https://www.nrel.gov/pv/cell-efficiency.html> (accessed: September 2020).
- [83] M. A. Green, Y. Hishikawa, E. D. Dunlop, D. H. Levi, J. Hohl-Ebinger, M. Yoshita, A. W. Y. Ho-Baillie, *Prog. Photovoltaics* **2019**, *27*, 3.
- [84] N. A. Kelly, T. L. Gibson, D. B. Ouwerkerk, *Int. J. Hydrogen Energy* **2011**, *36*, 15803.
- [85] T. L. Gibson, N. A. Kelly, *Int. J. Hydrogen Energy* **2008**, *33*, 5931.
- [86] N. A. Kelly, T. L. Gibson, D. B. Ouwerkerk, *Int. J. Hydrogen Energy* **2008**, *33*, 2747.
- [87] S. M. Bashir, M. A. Nadeem, M. Al-Oufi, M. Al-Hakami, T. T. Isimjan, H. Idriss, *ACS Omega* **2020**, *5*, 10510.
- [88] S. Muhammad-Bashir, M. Al-Oufi, M. Al-Hakami, M. A. Nadeem, K. Mudiyanselage, H. Idriss, *Sol. Energy* **2020**, *205*, 461.
- [89] T. J. Jacobsson, V. Fjällström, M. Edoff, T. Edvinsson, *Energy Environ. Sci.* **2014**, *7*, 2056.
- [90] A. C. Nielander, M. R. Shaner, K. M. Papadantonakis, S. A. Francis, N. S. Lewis, *Energy Environ. Sci.* **2014**, *8*, 16.
- [91] L. Pan, J. H. Kim, M. T. Mayer, M.-K. Son, A. Ummadisingu, J. S. Lee, A. Hagfeldt, J. Luo, M. Grätzel, *Nat. Catal.* **2018**, *1*, 412.
- [92] T. Takata, J. Jiang, Y. Sakata, M. Nakabayashi, N. Shibata, V. Nandal, K. Seki, T. Hisatomi, K. Domen, *Nature* **2020**, *581*, 411.
- [93] Q. Wang, T. Hisatomi, Y. Suzuki, Z. Pan, J. Seo, M. Katayama, T. Minegishi, H. Nishiyama, T. Takata, K. Seki, A. Kudo, T. Yamada, K. Domen, *J. Am. Chem. Soc.* **2017**, *139*, 1675.
- [94] B. S. Kalanoor, H. Seo, S. S. Kalanur, *Mater. Sci. Energy Technol.* **2018**, *1*, 49.
- [95] I. Y. Ahmet, Y. Ma, J.-W. Jang, T. Henschel, B. Stannowski, T. Lopes, A. Vilanova, A. Mendes, F. F. Abdi, R. van de Krol, *Sustainable Energy Fuels* **2019**, *3*, 2366.
- [96] Y. Pihosh, I. Turkevych, K. Mawatari, J. Uemura, Y. Kazoe, S. Kosar, K. Makita, T. Sugaya, T. Matsui, D. Fujita, M. Tosa, M. Kondo, T. Kitamori, *Sci. Rep.* **2015**, *5*, 11141.
- [97] J. Jia, L. C. Seitz, J. D. Benck, Y. Huo, Y. Chen, J. W. D. Ng, T. Bilir, J. S. Harris, T. F. Jaramillo, *Nat. Commun.* **2016**, *7*, 13237.

- [98] W.-H. Cheng, M. H. Richter, M. M. May, J. Ohlmann, D. Lackner, F. Dirnroth, T. Hannappel, H. A. Atwater, H.-J. Lewerenz, *ACS Energy Lett.* **2018**, 3, 1795.
- [99] K. Maeda, T. Takata, M. Hara, N. Saito, Y. Inoue, H. Kobayashi, K. Domen, *J. Am. Chem. Soc.* **2005**, 127, 8286.
- [100] Q. Wang, T. Hisatomi, Q. Jia, H. Tokudome, M. Zhong, C. Wang, Z. Pan, T. Takata, M. Nakabayashi, N. Shibata, Y. Li, I. D. Sharp, A. Kudo, T. Yamada, K. Domen, *Nat. Mater.* **2016**, 15, 611.
- [101] T. Hisatomi, J. Kubota, K. Domen, *Chem. Soc. Rev.* **2014**, 43, 7520.
- [102] B. A. Pinaud, J. D. Benck, L. C. Seitz, A. J. Forman, Z. Chen, T. G. Deutsch, B. D. James, K. N. Baum, G. N. Baum, S. Ardo, H. Wang, E. Miller, T. F. Jaramillo, *Energy Environ. Sci.* **2013**, 6, 1983.
- [103] Y. Ma, S. R. Pendlebury, A. Reynal, F. L. Formal, J. R. Durrant, *Chem. Sci.* **2014**, 5, 2964.
- [104] C. Zachäus, F. F. Abdi, L. M. Peter, R. van de Krol, *Chem. Sci.* **2017**, 8, 3712.
- [105] J. Luo, J.-H. Im, M. T. Mayer, M. Schreier, M. K. Nazeeruddin, N.-G. Park, S. D. Tilley, H. J. Fan, M. Grätzel, *Science* **2014**, 345, 1593.
- [106] R. Abe, C. M. Aitchison, V. Andrei, M. Beller, D. Cheung, C. E. Creissen, V. A. de la Peña O'Shea, J. R. Durrant, M. Grätzel, L. Hammarström, S. Haussener, S.-I. In, E. Kalamaras, A. Kudo, M. F. Kuehnel, P. P. Kunturu, Y.-H. Lai, C.-Y. Lee, M. Maneiro, E. E. Moore, H. C. Nguyen, A. R. Paris, C. Pornrungraj, J. N. H. Reek, E. Reisner, M. Schreck, W. A. Smith, H. S. Soo, R. S. Sprick, A. Venugopal, Q. Wang, D. Wieland, M. A. Zwijnenburg, *Faraday Discuss.* **2019**, 215, 345.
- [107] J. Tournet, Y. Lee, S. K. Karuturi, H. H. Tan, C. Jagadish, *ACS Energy Lett.* **2020**, 5, 611.
- [108] K. Sivula, R. van de Krol, *Nat. Rev. Mater.* **2016**, 1, 15010.
- [109] T. Hisatomi, K. Domen, *Nat. Catal.* **2019**, 2, 387.
- [110] F. F. Abdi, R. R. G. Perez, S. Haussener, *Sustainable Energy Fuels* **2020**, 4, 2734.
- [111] A. J. Bard, *J. Photochem.* **1979**, 10, 59.
- [112] R. E. Rocheleau, E. L. Miller, A. Misra, *Energy Fuels* **1998**, 12, 3.
- [113] D. G. Nocera, *Acc. Chem. Res.* **2012**, 45, 767.
- [114] N. S. Lewis, D. G. Nocera, *Proc. Natl. Acad. Sci. USA* **2006**, 103, 15729.
- [115] M. W. Kanan, Y. Surendranath, D. G. Nocera, *Chem. Soc. Rev.* **2008**, 38, 109.
- [116] Y. Ma, A. Kafizas, S. R. Pendlebury, F. Formal, J. R. Durrant, *Adv. Funct. Mater.* **2016**, 26, 4951.
- [117] B. Moss, F. S. Hegner, S. Corby, S. Selim, L. Francàs, N. López, S. Giménez, J.-R. Galán-Mascarós, J. R. Durrant, *ACS Energy Lett.* **2018**, 4, 337.
- [118] Q. Wang, J. Warnan, S. Rodríguez-Jiménez, J. J. Leung, S. Kalathil, V. Andrei, K. Domen, E. Reisner, *Nat. Energy* **2020**, 5, 703.
- [119] Q. Wang, Y. Li, T. Hisatomi, M. Nakabayashi, N. Shibata, J. Kubota, K. Domen, *J. Catal.* **2015**, 328, 308.
- [120] Y. Kuang, Q. Jia, G. Ma, T. Hisatomi, T. Minegishi, H. Nishiyama, M. Nakabayashi, N. Shibata, T. Yamada, A. Kudo, K. Domen, *Nat. Energy* **2016**, 2, 16191.
- [121] Q. Wang, S. Okunaka, H. Tokudome, T. Hisatomi, M. Nakabayashi, N. Shibata, T. Yamada, K. Domen, *Joule* **2018**, 2, 2667.
- [122] C. Grimes, in *Light, Water, Hydrogen: The Solar Generation of Hydrogen by Water Photoelectrolysis* (Eds: C. Grimes, O. Varghese, S. Ranjan), Springer US, New York **2008**, pp. 1–144.
- [123] R. Reichert, Z. Jusys, R. J. Behm, *J. Phys. Chem. C* **2015**, 119, 24750.
- [124] K. Sivula, *J. Phys. Chem. Lett.* **2015**, 6, 975.
- [125] U. S. D. of Energy, “DOE Technical Targets for Hydrogen Production from Photoelectrochemical Water Splitting,” <https://www.energy.gov/eere/fuelcells/doe-technical-targets-hydrogen-production-photoelectrochemical-water-splitting> (accessed: September 2020).
- [126] A. Fujishima, K. Honda, *Nature* **1972**, 238, 37.
- [127] “Web of Science [v.5.35] – Web of Science Core Collection Basic Search,” https://apps.webofknowledge.com/WOS_GeneralSearch_input.do?product=WOS&search_mode=GeneralSearch&SID=C6YmthCN8YQjKbXEZw2&preferencesSaved= (accessed: September 2020).
- [128] F. E. Osterloh, *Chem. Mater.* **2008**, 20, 35.
- [129] T. F. Jaramillo, S.-H. Baeck, A. Kleiman-Shwarsstein, K.-S. Choi, G. D. Stucky, E. W. McFarland, *J. Comb. Chem.* **2005**, 7, 264.
- [130] J. M. Gregoire, C. Xiang, X. Liu, M. Marcin, J. Jin, *Rev. Sci. Instrum.* **2013**, 84, 024102.
- [131] J. E. Katz, T. R. Gingrich, E. A. Santori, N. S. Lewis, *Energy Environ. Sci.* **2009**, 2, 103.
- [132] J. C. Hill, K.-S. Choi, *J. Phys. Chem. C* **2012**, 116, 7612.
- [133] A. B. Murphy, P. R. F. Barnes, L. K. Randeniya, I. C. Plumb, I. E. Grey, M. D. Horne, J. A. Glasscock, *Int. J. Hydrogen Energy* **2006**, 31, 1999.
- [134] A. Hankin, F. E. Bedoya-Lora, C. K. Ong, J. C. Alexander, F. Petter, G. H. Kelsall, *Energy Environ. Sci.* **2016**, 10, 346.
- [135] R. H. Coridan, A. C. Nielander, S. A. Francis, M. T. McDowell, V. Dix, S. M. Chatman, N. S. Lewis, *Energy Environ. Sci.* **2015**, 8, 2886.
- [136] A. Kafizas, X. Xing, S. Selim, C. A. Mesa, Y. Ma, C. Burgess, M. A. McLachlan, J. R. Durrant, *Catal. Today* **2019**, 321, 59.
- [137] M. R. Shaner, H. A. Atwater, N. S. Lewis, E. W. McFarland, *Energy Environ. Sci.* **2016**, 9, 2354.
- [138] Z. Chen, T. F. Jaramillo, T. G. Deutsch, A. Kleiman-Shwarsstein, A. J. Forman, N. Gaillard, R. Garland, K. Takanabe, C. Heske, M. Sunkara, E. W. McFarland, K. Domen, E. L. Miller, J. A. Turner, H. N. Dinh, *J. Mater. Res.* **2010**, 25, 3.
- [139] J. R. Bolton, S. J. Strickler, J. S. Connolly, *Nature* **1985**, 316, 495.
- [140] L. C. Seitz, Z. Chen, A. J. Forman, B. A. Pinaud, J. D. Benck, T. F. Jaramillo, *ChemSusChem* **2014**, 7, 1372.
- [141] S. J. A. Moniz, S. A. Shevlin, D. J. Martin, Z.-X. Guo, J. Tang, *Energy Environ. Sci.* **2015**, 8, 731.
- [142] L. M. Peter, K. G. U. Wijayantha, *ChemPhysChem* **2014**, 15, 1983.
- [143] G. Zheng, J. Wang, H. Liu, V. Murugadoss, G. Zu, H. Che, C. Lai, H. Li, T. Ding, Q. Gao, Z. Guo, *Nanoscale* **2019**, 11, 18968.
- [144] A. Fujishima, X. Zhang, D. A. Tryk, *Surf. Sci. Rep.* **2008**, 63, 515.
- [145] P. S. Bassi, Gurudayal, L. H. Wong, J. Barber, *Phys. Chem. Chem. Phys.* **2014**, 16, 11834.
- [146] I. V. Bagal, N. R. Chodankar, M. A. Hassan, A. Waseem, M. A. Johar, D.-H. Kim, S.-W. Ryu, *Int. J. Hydrogen Energy* **2019**, 44, 21351.
- [147] M. Imada, A. Fujimori, Y. Tokura, *Rev. Mod. Phys.* **1998**, 70, 1039.
- [148] E. Pastor, J.-S. Park, L. Steier, S. Kim, M. Grätzel, J. R. Durrant, A. Walsh, A. A. Bakulin, *Nat. Commun.* **2019**, 10, 3962.
- [149] S. R. Pendlebury, X. Wang, F. L. Formal, M. Cornuz, A. Kafizas, S. D. Tilley, M. Grätzel, J. R. Durrant, *J. Am. Chem. Soc.* **2014**, 136, 9854.
- [150] F. L. Formal, S. R. Pendlebury, M. Cornuz, S. D. Tilley, M. Grätzel, J. R. Durrant, *J. Am. Chem. Soc.* **2014**, 136, 2564.
- [151] A. Hankin, F. E. Bedoya-Lora, J. C. Alexander, A. Regoutz, G. H. Kelsall, *J. Mater. Chem. A* **2019**, 7, 26162.
- [152] M. G. Walter, E. L. Warren, J. R. McKone, S. W. Boettcher, Q. Mi, E. A. Santori, N. S. Lewis, *Chem. Rev.* **2010**, 110, 6446.
- [153] Y. Wang, A. Vogel, M. Sachs, R. S. Sprick, L. Wilbraham, S. J. A. Moniz, R. Godin, M. A. Zwijnenburg, J. R. Durrant, A. I. Cooper, J. Tang, *Nat. Energy* **2019**, 4, 746.
- [154] W. Shockley, H. J. Queisser, *J. Appl. Phys.* **1961**, 32, 510.
- [155] R. Liu, Z. Zheng, J. Spurgeon, X. Yang, *Energy Environ. Sci.* **2014**, 7, 2504.
- [156] J. W. Ager, M. R. Shaner, K. A. Walczak, I. D. Sharp, S. Ardo, *Energy Environ. Sci.* **2015**, 8, 2811.
- [157] H. Kobayashi, N. Sato, M. Orita, Y. Kuang, H. Kaneko, T. Minegishi, T. Yamada, K. Domen, *Energy Environ. Sci.* **2018**, 11, 3003.
- [158] M. Wang, Y.-S. Chang, C.-W. Tsao, M.-J. Fang, Y.-J. Hsu, K.-L. Choy, *Chem. Commun.* **2019**, 55, 2465.

- [159] O. Khaselev, J. A. Turner, *Science* **1998**, 280, 425.
- [160] J. L. Young, M. A. Steiner, H. Dösscher, R. M. France, J. A. Turner, T. G. Deutsch, *Nat. Energy* **2017**, 2, 17028.
- [161] M. A. Khan, I. Al-Shankiti, A. Ziani, N. Wehbe, H. Idriss, *Angew. Chem., Int. Ed.* **2020**, 59, 14802.
- [162] A. Ziani, I. Al-Shankiti, M. A. Khan, H. Idriss, *Energy Fuels* **2020**, 34, 13179.
- [163] J. Liu, Y. Yao, S. Xiao, X. Gu, *J. Phys. D: Appl. Phys.* **2018**, 51, 123001.
- [164] Z. Luo, T. Wang, J. Gong, *Chem. Soc. Rev.* **2019**, 48, 2158.
- [165] S. Y. Reece, J. A. Hamel, K. Sung, T. D. Jarvi, A. J. Esswein, J. J. H. Pijpers, D. G. Nocera, *Science* **2011**, 334, 645.
- [166] I. A. Moreno-Hernandez, B. S. Brunschwig, N. S. Lewis, *Adv. Energy Mater.* **2018**, 8, 1801155.
- [167] F. Urbain, V. Smirnov, J.-P. Becker, U. Rau, J. Ziegler, B. Kaiser, W. Jaegermann, F. Finger, *Sol. Energy Mater. Sol. Cells* **2015**, 140, 275.
- [168] E. L. Warren, J. R. McKone, H. A. Atwater, H. B. Gray, N. S. Lewis, *Energy Environ. Sci.* **2012**, 5, 9653.
- [169] J. D. Benck, S. C. Lee, K. D. Fong, J. Kibsgaard, R. Sinclair, T. F. Jaramillo, *Adv. Energy Mater.* **2014**, 4, 1400739.
- [170] H.-P. Wang, K. Sun, S. Y. Noh, A. Kargar, M.-L. Tsai, M.-Y. Huang, D. Wang, J.-H. He, *Nano Lett.* **2015**, 15, 2817.
- [171] F. Urbain, V. Smirnov, J.-P. Becker, A. Lambertz, F. Yang, J. Ziegler, B. Kaiser, W. Jaegermann, U. Rau, F. Finger, *Energy Environ. Sci.* **2015**, 9, 145.
- [172] Y. Yang, S. Niu, D. Han, T. Liu, G. Wang, Y. Li, *Adv. Energy Mater.* **2017**, 7, 1700555.
- [173] S. Krment, F. Riboni, S. Pausova, L. Wang, L. Wang, H. Han, Z. Hubicka, J. Krysa, P. Schmuki, R. Zboril, *Chem. Soc. Rev.* **2017**, 46, 3716.
- [174] K. Sivula, F. Le Formal, M. Grätzel, *ChemSusChem* **2011**, 4, 432.
- [175] Y. Park, K. J. McDonald, K. S. Choi, *Chem. Soc. Rev.* **2013**, 42, 2321.
- [176] B. Weng, C. R. Grice, J. Ge, T. Poudel, X. Deng, Y. Yan, *Adv. Energy Mater.* **2018**, 8, 1701655.
- [177] W.-J. Yin, B. Weng, J. Ge, Q. Sun, Z. Li, Y. Yan, *Energy Environ. Sci.* **2018**, 12, 442.
- [178] J. Ge, W.-J. Yin, Y. Yan, *Chem. Mater.* **2018**, 30, 1017.
- [179] Y. Xu, M. A. A. Schoonen, *Am. Mineral.* **2000**, 85, 543.
- [180] S. Chen, L.-W. Wang, *Chem. Mater.* **2012**, 24, 3659.
- [181] A. Mills, S. L. Hunte, *J. Photochem. Photobiol., A* **1997**, 108, 1.
- [182] S. Banerjee, D. D. Dionysiou, S. C. Pillai, *Appl. Catal., B* **2015**, 176, 396.
- [183] L.-J. Guo, J.-W. Luo, T. He, S.-H. Wei, S.-S. Li, *Phys. Rev. Appl.* **2018**, 10, 064059.
- [184] J. Liu, X. Yu, Q. Liu, R. Liu, X. Shang, S. Zhang, W. Li, W. Zheng, G. Zhang, H. Cao, Z. Gu, *Appl. Catal., B* **2014**, 158, 296.
- [185] P. Roy, C. Das, K. Lee, R. Hahn, T. Ruff, M. Moll, P. Schmuki, *J. Am. Chem. Soc.* **2011**, 133, 5629.
- [186] M. Liu, N. de Leon Snapp, H. Park, *Chem. Sci.* **2010**, 2, 80.
- [187] A. G. Tamirat, J. Rick, A. A. Dubale, W.-N. Su, B.-J. Hwang, *Nanoscale Horiz.* **2016**, 1, 243.
- [188] C. Du, X. Yang, M. T. Mayer, H. Hoyt, J. Xie, G. McMahon, G. Bischoff, D. Wang, *Angew. Chem., Int. Ed.* **2013**, 52, 12692.
- [189] A. Kay, I. Cesar, M. Grätzel, *J. Am. Chem. Soc.* **2006**, 128, 15714.
- [190] S. D. Tilley, M. Cornuz, K. Sivula, M. Grätzel, *Angew. Chem., Int. Ed.* **2010**, 49, 6405.
- [191] J. Y. Kim, G. Magesh, D. H. Youn, J.-W. Jang, J. Kubota, K. Domen, J. S. Lee, *Sci. Rep.* **2013**, 3, 2681.
- [192] A. Vilanova, T. Lopes, C. Spenke, M. Wullenkord, A. Mendes, *Energy Storage Mater.* **2018**, 13, 175.
- [193] A. Vilanova, P. Dias, J. Azevedo, M. Wullenkord, C. Spenke, T. Lopes, A. Mendes, *J. Power Sources* **2020**, 454, 227890.
- [194] X. Liu, F. Wang, Q. Wang, *Phys. Chem. Chem. Phys.* **2012**, 14, 7894.
- [195] S. S. Kalanur, L. T. Duy, H. Seo, *Top. Catal.* **2018**, 61, 1043.
- [196] C. A. Mesa, L. Francàs, K. R. Yang, P. Garrido-Barros, E. Pastor, Y. Ma, A. Kafizas, T. E. Rosser, M. T. Mayer, E. Reisner, M. Grätzel, V. S. Batista, J. R. Durrant, *Nat. Chem.* **2020**, 12, 82.
- [197] S. Corby, L. Francàs, S. Selim, M. Sachs, C. Blackman, A. Kafizas, J. R. Durrant, *J. Am. Chem. Soc.* **2018**, 140, 16168.
- [198] C. Fàbrega, S. Murcia-López, D. Monllor-Satoca, J. D. Prades, M. D. Hernández-Alonso, G. Penelas, J. R. Morante, T. Andreu, *Appl. Catal., B* **2016**, 189, 133.
- [199] S. Wang, H. Chen, G. Gao, T. Butburee, M. Lyu, S. Thaweesak, J.-H. Yun, A. Du, G. Liu, L. Wang, *Nano Energy* **2016**, 24, 94.
- [200] J. Brillet, J.-H. Yum, M. Cornuz, T. Hisatomi, R. Solarska, J. Augustynski, M. Graetzel, K. Sivula, *Nat. Photonics* **2012**, 6, 824.
- [201] W. J. Lee, P. S. Shinde, G. H. Go, E. Ramasamy, *Int. J. Hydrogen Energy* **2011**, 36, 5262.
- [202] B. Beverskog, I. Puigdomenech, *J. Electrochem. Soc.* **1997**, 144, 3476.
- [203] R. W. Johnson, A. Hultqvist, S. F. Bent, *Mater. Today* **2014**, 17, 236.
- [204] M. Ritala, J. Niinistö, *ECS Trans.* **2019**, 25, 641.
- [205] P. Dai, W. Li, J. Xie, Y. He, J. Thorne, G. McMahon, J. Zhan, D. Wang, *Angew. Chem., Int. Ed.* **2014**, 53, 13493.
- [206] A. Paracchino, V. Laporte, K. Sivula, M. Grätzel, E. Thimsen, *Nat. Mater.* **2011**, 10, 456.
- [207] S. D. Tilley, M. Schreier, J. Azevedo, M. Stefk, M. Graetzel, *Adv. Funct. Mater.* **2014**, 24, 303.
- [208] C. G. Morales-Guio, S. D. Tilley, H. Vrubel, M. Grätzel, X. Hu, *Nat. Commun.* **2014**, 5, 3059.
- [209] J. Luo, L. Steier, M.-K. Son, M. Schreier, M. T. Mayer, M. Grätzel, *Nano Lett.* **2016**, 16, 1848.
- [210] D. Chua, S. B. Kim, R. Gordon, *AIP Adv.* **2019**, 9, 055203.
- [211] Y. Park, K. J. McDonald, K.-S. Choi, *Chem. Soc. Rev.* **2012**, 42, 2321.
- [212] J. H. Kim, Y. H. Jo, J. H. Kim, J. S. Lee, *Nanoscale* **2016**, 8, 17623.
- [213] D. K. Lee, K.-S. Choi, *Nat. Energy* **2018**, 3, 53.
- [214] Y. Qiu, W. Liu, W. Chen, W. Chen, G. Zhou, P.-C. Hsu, R. Zhang, Z. Liang, S. Fan, Y. Zhang, Y. Cui, *Sci. Adv.* **2016**, 2, e1501764.
- [215] J. H. Baek, B. J. Kim, G. S. Han, S. W. Hwang, D. R. Kim, I. S. Cho, H. S. Jung, *ACS Appl. Mater. Interfaces* **2017**, 9, 1479.
- [216] S. Wang, P. Chen, Y. Bai, J. Yun, G. Liu, L. Wang, *Adv. Mater.* **2018**, 30, 1800486.
- [217] F. F. Abdi, L. Han, A. H. M. Smets, M. Zeman, B. Dam, R. van de Krol, *Nat. Commun.* **2013**, 4, 2195.
- [218] J. H. Kim, Y. Jo, J. H. Kim, J. W. Jang, H. J. Kang, Y. H. Lee, D. S. Kim, Y. Jun, J. S. Lee, *ACS Nano* **2015**, 9, 11820.
- [219] L. Han, F. F. Abdi, R. van de Krol, R. Liu, Z. Huang, H. Lewerenz, B. Dam, M. Zeman, A. H. M. Smets, *ChemSusChem* **2014**, 7, 2832.
- [220] K. Rajeshwar, M. K. Hossain, R. T. Macaluso, C. Janáky, A. Varga, P. J. Kulesza, *J. Electrochem. Soc.* **2018**, 165, H3192.
- [221] J. H. Kim, H. E. Kim, J. H. Kim, J. S. Lee, *J. Mater. Chem. A* **2020**, 8, 9447.
- [222] P. Kanhere, Z. Chen, *Molecules* **2014**, 19, 19995.
- [223] J. Ke, M. A. Younis, Y. Kong, H. Zhou, J. Liu, L. Lei, Y. Hou, *Nano-Micro Lett.* **2018**, 10, 69.
- [224] A. Hassan, T. Iqbal, M. B. Tahir, S. Afsheen, *Int. J. Energy Res.* **2019**, 43, 9.
- [225] Q. Liu, J. He, T. Yao, Z. Sun, W. Cheng, S. He, Y. Xie, Y. Peng, H. Cheng, Y. Sun, Y. Jiang, F. Hu, Z. Xie, W. Yan, Z. Pan, Z. Wu, S. Wei, *Nat. Commun.* **2014**, 5, 5122.
- [226] X. Zhu, N. Guijarro, Y. Liu, P. Schouwink, R. A. Wells, F. Formal, S. Sun, C. Gao, K. Sivula, *Adv. Mater.* **2018**, 30, 1801612.
- [227] M. S. Prévôt, N. Guijarro, K. Sivula, *ChemSusChem* **2015**, 8, 1359.
- [228] F. Wang, W. Septina, A. Chemseddine, F. F. Abdi, D. Friedrich, P. Bogdanoff, R. van de Krol, S. D. Tilley, S. P. Berglund, *J. Am. Chem. Soc.* **2017**, 139, 15094.
- [229] Z.-H. Cui, H. Jiang, *J. Phys. Chem. C* **2017**, 121, 3241.
- [230] C. M. Fang, E. Orhan, G. A. de Wijs, H. T. Hintzen, R. A. de Groot, R. Marchand, J.-Y. Saillard, G. de With, *J. Mater. Chem.* **2001**, 11, 1248.
- [231] E. Nurlaela, M. Harb, S. del Gobbo, M. Vashishta, K. Takanabe, *J. Solid State Chem.* **2015**, 229, 219.

- [232] Z. Wang, Y. Inoue, T. Hisatomi, R. Ishikawa, Q. Wang, T. Takata, S. Chen, N. Shibata, Y. Ikuhara, K. Domen, *Nat. Catal.* **2018**, *1*, 756.
- [233] T. Jing, Y. Dai, X. Ma, W. Wei, B. Huang, *RSC Adv.* **2015**, *5*, 59390.
- [234] T. Higashi, H. Nishiyama, Y. Suzuki, Y. Sasaki, T. Hisatomi, M. Katayama, T. Minegishi, K. Seki, T. Yamada, K. Domen, *Angew. Chem., Int. Ed.* **2019**, *58*, 2300.
- [235] Y. Li, T. Takata, D. Cha, K. Takanabe, T. Minegishi, J. Kubota, K. Domen, *Adv. Mater.* **2013**, *25*, 125.
- [236] R. Chen, C. Zhen, Y. Yang, X. Sun, J. T. S. Irvine, L. Wang, G. Liu, H.-M. Cheng, *Nano Energy* **2019**, *59*, 683.
- [237] G. Liu, S. Ye, P. Yan, F. Xiong, P. Fu, Z. Wang, Z. Chen, J. Shi, C. Li, *Energy Environ. Sci.* **2016**, *9*, 1327.
- [238] Y. He, J. E. Thorne, C. H. Wu, P. Ma, C. Du, Q. Dong, J. Guo, D. Wang, *Chem* **2016**, *1*, 640.
- [239] J. Fu, F. Wang, Y. Xiao, Y. Yao, C. Feng, L. Chang, C.-M. Jiang, V. F. Kunzelmann, Z. M. Wang, A. O. Govorov, I. D. Sharp, Y. Li, *ACS Catal.* **2020**, *10*, 10316.
- [240] T. Minegishi, N. Nishimura, J. Kubota, K. Domen, *Chem. Sci.* **2012**, *4*, 1120.
- [241] R. Abe, M. Higashi, K. Domen, *J. Am. Chem. Soc.* **2010**, *132*, 11828.
- [242] M. Higashi, K. Domen, R. Abe, *J. Am. Chem. Soc.* **2012**, *134*, 6968.
- [243] S. Akiyama, M. Nakabayashi, N. Shibata, T. Minegishi, Y. Asakura, M. Abdulla-Al-Mamun, T. Hisatomi, H. Nishiyama, M. Katayama, T. Yamada, K. Domen, *Small* **2016**, *12*, 5468.
- [244] A. J. Gardecka, C. Bishop, D. Lee, S. Corby, I. P. Parkin, A. Kafizas, S. Krumdieck, *Appl. Catal., B* **2018**, *224*, 904.
- [245] Y. Qiu, S.-F. Leung, Q. Zhang, B. Hua, Q. Lin, Z. Wei, K.-H. Tsui, Y. Zhang, S. Yang, Z. Fan, *Nano Lett.* **2014**, *14*, 2123.
- [246] T. W. Kim, K. S. Choi, *Science* **2014**, *343*, 990.
- [247] D. K. Lee, D. Lee, M. A. Lumley, K.-S. Choi, *Chem. Soc. Rev.* **2018**, *48*, 2126.
- [248] Y. W. Phuan, W.-J. Ong, M. N. Chong, J. D. Ocon, *J. Photochem. Photobiol., C* **2017**, *33*, 54.
- [249] A. J. E. Rettie, H. C. Lee, L. G. Marshall, J.-F. Lin, C. Capan, J. Lindemuth, J. S. McCloy, J. Zhou, A. J. Bard, C. B. Mullins, *J. Am. Chem. Soc.* **2013**, *135*, 11389.
- [250] Y. Mi, Y. Weng, *Sci. Rep.* **2015**, *5*, 11482.
- [251] A. Pu, J. Deng, M. Li, J. Gao, H. Zhang, Y. Hao, J. Zhong, X. Sun, *J. Mater. Chem. A* **2013**, *2*, 2491.
- [252] L. Chen, F. M. Toma, J. K. Cooper, A. Lyon, Y. Lin, I. D. Sharp, J. W. Ager, *ChemSusChem* **2015**, *8*, 1066.
- [253] C. S. Enache, J. Schoonman, R. V. Krol, *J. Electroceram.* **2004**, *13*, 177.
- [254] A. K. Ghosh, H. P. Maruska, *J. Electrochem. Soc.* **1977**, *124*, 1516.
- [255] I. Watanabe, Y. Matsumoto, E.-I. Sato, *J. Electroanal. Chem. Interfacial Electrochem.* **1982**, *133*, 359.
- [256] R. Medhi, M. D. Marquez, T. R. Lee, *ACS Appl. Nano Mater.* **2020**, *3*, 6156.
- [257] W. Li, *Phys. Status Solidi RRL* **2015**, *9*, 10.
- [258] S. A. Ansari, M. M. Khan, M. O. Ansari, M. H. Cho, *New J. Chem.* **2016**, *40*, 3000.
- [259] N. Serpone, *J. Phys. Chem. B* **2006**, *110*, 24287.
- [260] G. Torres, T. Lindgren, J. Lu, C.-G. Granqvist, S.-E. Lindquist, *J. Phys. Chem. B* **2004**, *108*, 5995.
- [261] J. Tang, A. J. Cowan, J. R. Durrant, D. R. Klug, *J. Phys. Chem. C* **2011**, *115*, 3143.
- [262] J. Balbuena, M. Cruz-Yusta, L. Sánchez, *J. Nanosci. Nanotechnol.* **2015**, *15*, 6373.
- [263] N. P. Chadwick, A. Kafizas, R. Quesada-Cabrera, C. Sotelo-Vazquez, S. M. Bawaked, M. Mokhtar, S. A. A. Thabaiti, A. Y. Obaid, S. N. Basahel, J. R. Durrant, C. J. Carmalt, I. P. Parkin, *ACS Catal.* **2017**, *7*, 1485.
- [264] S. Kawasaki, K. Akagi, K. Nakatsuji, S. Yamamoto, I. Matsuda, Y. Harada, J. Yoshinobu, F. Komori, R. Takahashi, M. Lippmaa, C. Sakai, H. Niwa, M. Oshima, K. Iwashina, A. Kudo, *J. Phys. Chem. C* **2012**, *116*, 24445.
- [265] E. N. K. Glover, S. G. Ellington, G. Sankar, R. G. Palgrave, *J. Mater. Chem. A* **2016**, *4*, 6946.
- [266] R. Niishiro, R. Konta, H. Kato, W. J. Chun, K. Asakura, A. Kudo, *J. Phys. Chem. C* **2007**, *111*, 17420.
- [267] D. H. K. Murthy, H. Matsuzaki, Q. Wang, Y. Suzuki, K. Seki, T. Hisatomi, T. Yamada, A. Kudo, K. Domen, A. Furube, *Sustainable Energy Fuels* **2018**, *3*, 208.
- [268] Q. Wang, T. Hisatomi, S. S. K. Ma, Y. Li, K. Domen, *Chem. Mater.* **2014**, *26*, 4144.
- [269] B. A. D. Williamson, J. Buckeridge, N. P. Chadwick, S. Sathasivam, C. J. Carmalt, I. P. Parkin, D. O. Scanlon, *Chem. Mater.* **2019**, *31*, 2577.
- [270] K. Iwashina, A. Kudo, *J. Am. Chem. Soc.* **2011**, *133*, 13272.
- [271] B. Modak, S. K. Ghosh, *J. Phys. Chem. B* **2015**, *119*, 11089.
- [272] J. Prakash, U. Prasad, X. Shi, X. Peng, B. Azeredo, A. M. Kannan, *J. Power Sources* **2019**, *448*, 227418.
- [273] C. Zhou, Z. Sanders-Bellis, T. J. Smart, W. Zhang, L. Zhang, Y. Ping, M. Liu, *Chem. Mater.* **2020**, *32*, 6401.
- [274] H. Chen, S. Yang, *Nanoscale Horiz.* **2015**, *1*, 96.
- [275] G. Wang, Y. Ling, H. Wang, L. Xihong, Y. Li, *J. Photochem. Photobiol., C* **2014**, *19*, 35.
- [276] F. E. Osterloh, *Chem. Soc. Rev.* **2012**, *42*, 2294.
- [277] C. Battaglia, A. Cuevas, S. D. Wolf, *Energy Environ. Sci.* **2016**, *9*, 1552.
- [278] J. Nelson, *Mater. Today* **2011**, *14*, 462.
- [279] A. J. Cowan, J. R. Durrant, *Chem. Soc. Rev.* **2012**, *42*, 2281.
- [280] R. Godin, A. Kafizas, J. R. Durrant, *Curr. Opin. Electrochem.* **2017**, *2*, 136.
- [281] T. Cardona, A. Sedoud, N. Cox, A. W. Rutherford, *Biochim. Biophys. Acta, Bioenerg.* **2012**, *1817*, 26.
- [282] S. Selim, L. Francas, M. Garcia-Tecedor, S. Corby, C. GarBlackman, S. Gimenez, J. R. Durrant, A. Kafizas, *Chem. Sci.* **2019**, *10*, 2643.
- [283] C. Ràfols i Bellés, S. Selim, N. M. Harrison, E. A. Ahmad, A. Kafizas, *Sustainable Energy Fuels* **2018**, *3*, 264.
- [284] E. Pastor, F. Formal, M. T. Mayer, D. S. Tilley, L. Francàs, C. A. Mesa, M. Grätzel, J. R. Durrant, *Nat. Commun.* **2017**, *8*, 14280.
- [285] S. K. Pilli, T. E. Furtak, L. D. Brown, T. G. Deutsch, J. A. Turner, A. M. Herring, *Energy Environ. Sci.* **2011**, *4*, 5028.
- [286] S. D. Watson, K. J. Lomas, R. A. Buswell, *Energy Policy* **2019**, *126*, 533.
- [287] P. Rowley, G. Wilson, R. Taylor, Challenges for the Decarbonisation of Heat: Local Gas Demand vs Electricity Supply Winter 2017/2018, **2018**.
- [288] H21, "Could the 21st Century be dominated by hydrogen?," <https://www.h21.green/could-the-21st-century-be-dominated-by-hydrogen/> (accessed:).
- [289] Ofgem(C), "Data Portal Overview," <https://www.ofgem.gov.uk/data-portal/overview> (accessed: September 2020).
- [290] M. A. Sayegh, P. Jadwiszczak, B. P. Axcell, E. Niemierka, K. Bryś, H. Jouhara, *Energy Build.* **2018**, *166*, 122.
- [291] N. Sunny, N. Mac Dowell, N. Shah, *Energy Environ. Sci.* **2020**, *13*, 4204.
- [292] National Grid UK, "Calorific value (CV)," <https://www.nationalgrid.com/uk/gas-transmission/data-and-operations/calorific-value-cv#:~:text=CV%20enquiries&text=The%20CV%20of%20gas%2C%20which,m3%20to%2043.0%20MJ%2Fm3.> (accessed: September 2020).
- [293] P. E. Dodds, S. Demoulin, *Int. J. Hydrogen Energy* **2013**, *38*, 7189.
- [294] J. R. Durrant, L. Hammarström, *Mission Innovation Challenge "Converting Sunlight"*, <http://mission-innovation.net/wp-content/uploads/2019/11/IIC5-Cambridge-2019-Draft-1.pdf> (accessed: September 2020).
- [295] NASA, "NASA POWER | Prediction Of Worldwide Energy Resources," <https://power.larc.nasa.gov/data-access-viewer/> (accessed: September 2020).

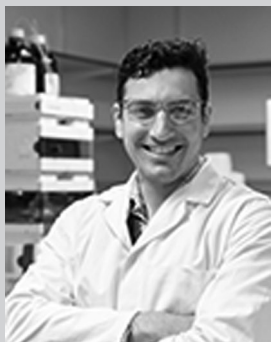
- [296] Nuclear Decommissioning Authority, "Guidance on Technology Readiness Levels," <https://www.gov.uk/government/news/guidance-on-technology-readiness-levels> (accessed: September 2020).
- [297] C. Ros, T. Andreu, J. R. Morante, *J. Mater. Chem. A* **2020**, *8*, 10625.
- [298] A. Kafizas, I. P. Parkin, in (Eds: T. M. Letcher, J. L. Scott), **2012**, <https://pubs.rsc.org/en/content/ebook/9781849734073>.
- [299] J. H. Kim, D. Hansora, P. Sharma, J.-W. Jang, J. S. Lee, *Chem. Soc. Rev.* **2019**, *48*, 1908.
- [300] X. Yin, Q. Liu, Y. Yang, Y. Liu, K. Wang, Y. Li, D. Li, X. Qiu, W. Li, J. Li, *Int. J. Hydrogen Energy* **2018**, *44*, 594.
- [301] P. Bornoz, F. F. Abdi, S. D. Tilley, B. Dam, R. van de Krol, M. Graetzel, K. Sivula, *J. Phys. Chem. C* **2014**, *118*, 16959.
- [302] J.-P. Becker, B. Turan, V. Smirnov, K. Welter, F. Urbain, J. Wolff, S. Haas, F. Finger, *J. Mater. Chem. A* **2017**, *5*, 4818.
- [303] A. Landman, R. Halabi, P. Dias, H. Dotan, A. Mehlmann, G. E. Shter, M. Halabi, O. Naseraldeen, A. Mendes, G. S. Grader, A. Rothschild, *Joule* **2020**, *4*, 448.
- [304] I. Holmes-Gentle, F. Alhersh, F. Bedoya-Lora, K. Hellgardt, in *Photoelectrochemical Solar Cells* (Eds: N. D. Sankir, M. Sankir), John Wiley & Sons, Inc., Hoboken, NJ **2018**, p. 1.
- [305] C. Carver, Z. Ulli, C. K. Ong, S. Dennison, G. H. Kelsall, K. Hellgardt, *Int. J. Hydrogen Energy* **2012**, *37*, 2911.
- [306] T. Lopes, P. Dias, L. Andrade, A. Mendes, *Sol. Energy Mater. Sol. Cells* **2014**, *128*, 399.
- [307] Y. Li, H. Yu, W. Song, G. Li, B. Yi, Z. Shao, *Int. J. Hydrogen Energy* **2011**, *36*, 14374.
- [308] M. Graetzel, J. Augustynski, *US6936143B1*, **2005**.
- [309] Q. Fan, M. Onischak, W. E. Liss, *US7241950B2*, **2007**.
- [310] E. Verlage, S. Hu, R. Liu, R. J. R. Jones, K. Sun, C. Xiang, N. S. Lewis, H. A. Atwater, *Energy Environ. Sci.* **2015**, *8*, 3166.
- [311] E. Sell, G. L. Chiarello, E. Quararone, P. Mustarelli, I. Rossetti, L. Forni, *Chem. Commun.* **2007**, 5022.
- [312] E. L. Miller, R. E. Rocheleau, X. M. Deng, *Int. J. Hydrogen Energy* **2003**, *28*, 615.
- [313] F. E. Bedoya-Lora, A. Hankin, G. H. Kelsall, *J. Mater. Chem. A* **2017**, *5*, 22683.
- [314] S. Haussener, C. Xiang, J. M. Spurgeon, S. Ardo, N. S. Lewis, A. Z. Weber, *Energy Environ. Sci.* **2012**, *5*, 9922.
- [315] T. Bosserez, L. Geerts, J. Rongé, F. Ceyssens, S. Haussener, R. Puers, J. A. Martens, *J. Phys. Chem. C* **2016**, *120*, 21242.
- [316] K. Walczak, Y. Chen, C. Karp, J. W. Beeman, M. Shaner, J. Spurgeon, I. D. Sharp, X. Amashukeli, W. West, J. Jin, N. S. Lewis, C. Xiang, *ChemSusChem* **2015**, *8*, 544.
- [317] X. Deng, L. Xu, *US7750234B2*, **2010**.
- [318] B. Turan, J.-P. Becker, F. Urbain, F. Finger, U. Rau, S. Haas, *Nat. Commun.* **2016**, *7*, 12681.
- [319] A. Landman, H. Dotan, G. E. Shter, M. Wullenkord, A. Houaijia, A. Maljusch, G. S. Grader, A. Rothschild, *Nat. Mater.* **2017**, *16*, 646.
- [320] N. A. Kelly, T. L. Gibson, *Int. J. Hydrogen Energy* **2008**, *33*, 6420.
- [321] S. Tembharne, S. Haussener, *J. Electrochem. Soc.* **2016**, *163*, H988.
- [322] S. Tembharne, F. Nandjou, S. Haussener, *Nat. Energy* **2019**, *4*, 399.
- [323] I. Holmes-Gentle, F. Hoffmann, C. A. Mesa, K. Hellgardt, *Sustainable Energy Fuels* **2017**, *1*, 1184.
- [324] A. Vilanova, T. Lopes, A. Mendes, *J. Power Sources* **2018**, *398*, 224.
- [325] K. T. Fountaine, H. J. Lewerenz, H. A. Atwater, *Nat. Commun.* **2016**, *7*, 13706.
- [326] M. A. Modestino, S. M. H. Hashemi, S. Haussener, *Energy Environ. Sci.* **2016**, *9*, 1533.
- [327] M. E. Orazem, J. Newman, *J. Electrochem. Soc.* **1984**, *131*, 2857.
- [328] C. Trompoukis, A. Abass, J.-W. Schüttauf, T. Bosserez, J. Rongé, J. Lauwaert, J. A. Martens, R. Baets, *Sol. Energy Mater. Sol. Cells* **2018**, *182*, 196.
- [329] I. Holmes-Gentle, H. Agarwal, F. Alhersh, K. Hellgardt, *Phys. Chem. Chem. Phys.* **2018**, *20*, 12422.
- [330] A. Angulo, P. van der Linde, H. Gardeniers, M. Modestino, D. F. Rivas, *Joule* **2020**, *4*, 555.
- [331] I. Holmes-Gentle, F. Bedoya-Lora, F. Alhersh, K. Hellgardt, *J. Phys. Chem. C* **2018**, *123*, 17.
- [332] A. E. Dorfi, A. C. West, D. V. Esposito, *J. Phys. Chem. C* **2017**, *121*, 26587.
- [333] H. Vogt, R. J. Balzer, *Electrochim. Acta* **2005**, *50*, 2073.
- [334] K. Brinkert, M. H. Richter, Ö. Akay, J. Liedtke, M. Giersig, K. T. Fountaine, H.-J. Lewerenz, *Nat. Commun.* **2018**, *9*, 2527.
- [335] P. A. Kempler, R. H. Coridan, N. S. Lewis, *Energy Environ. Sci.* **2020**, *13*, 1808.
- [336] S. Hernández, G. Barbero, G. Saracco, A. L. Alexe-Ionescu, *J. Phys. Chem. C* **2015**, *119*, 9916.
- [337] J. Dukovic, C. W. Tobias, *J. Electrochem. Soc.* **1987**, *134*, 331.
- [338] F. Nandjou, S. Haussener, *J. Phys. D: Appl. Phys.* **2017**, *50*, 124002.
- [339] D. P. Sutija, C. W. Tobias, *J. Electrochem. Soc.* **1994**, *141*, 2599.
- [340] A. Alexiadis, M. P. Dudukovic, P. Ramachandran, A. Cornell, J. Wanngård, A. Bokkers, *Chem. Eng. Sci.* **2011**, *66*, 2252.
- [341] J. O. Bockris, *Modern Electrochemistry 2A: Fundamentals of Electrodics*, Kluwer Academic/Plenum Publishers, New York **2000**.
- [342] R. Hreiz, L. Abdelouahed, D. Fünfschilling, F. Lapicque, *Chem. Eng. Res. Des.* **2015**, *100*, 268.
- [343] H. Rusche, R. I. Rusche, The Effect of Voidage on the Drag Force on Particles, Droplets and Bubbles in Dispersed Two-Phase Flow, Japanese European Two-Phase Flow Meeting, Tshkuba, Japan, **2000**, pp. 1–8.
- [344] P. Dias, A. Mendes, in *Encyclopedia of Sustainability Science and Technology* (Ed: R. A. Meyers), Springer, New York **2017**, pp. 1–52.
- [345] G. Levêque, R. Bader, W. Lipiński, S. Haussener, *Opt. Express* **2016**, *24*, A1360.
- [346] S. Tembharne, S. Haussener, H2 International, **2020**.
- [347] S. Caron, M. Röger, M. Wullenkord, *Energies* **2020**, *13*, 5196.
- [348] D. V. Esposito, *Joule* **2017**, *1*, 651.
- [349] J. C. Bui, J. T. Davis, D. V. Esposito, *Sustainable Energy Fuels* **2019**, *4*, 213.
- [350] A. Berger, J. Newman, *J. Electrochem. Soc.* **2014**, *161*, E3328.
- [351] A. Berger, R. A. Segalman, J. Newman, *Energy Environ. Sci.* **2014**, *7*, 1468.
- [352] H. Zhang, H. Wang, J. Xuan, *J. Power Sources* **2020**, *462*, 228113.
- [353] P. Cendula, P. P. Sahoo, G. Cibira, P. Simon, *J. Phys. Chem. C* **2019**, *124*, 1269.
- [354] A. Iqbal, K. H. Bevan, *J. Phys. Chem. C* **2017**, *122*, 30.
- [355] A. Iqbal, M. D. S. Hossain, K. H. Bevan, *Phys. Chem. Chem. Phys.* **2016**, *18*, 29466.
- [356] K. Ronaszegi, E. S. Fraga, J. Darr, P. R. Shearing, D. J. L. Brett, *Molecules* **2019**, *25*, 123.
- [357] M. Dumortier, S. Tembharne, S. Haussener, *Energy Environ. Sci.* **2015**, *8*, 3614.
- [358] A. Christensen, *Assessment of Hydrogen Production Costs from Electrolysis: United States and Europe*, International Council on Clean Transportation, Berlin **2020**.
- [359] G. Glenk, S. Reichelstein, *Nat. Energy* **2019**, *4*, 216.
- [360] J. Friedmann, Z. Fan, K. Tang, *Low-Carbon Heat Solutions for Heavy Industry: Sources, Options, and Costs Today*, Columbia University SIPA, New York **2019**.
- [361] A. Grimm, W. A. de Jong, G. J. Kramer, *Int. J. Hydrogen Energy* **2020**, *45*, 22545.
- [362] A. Nakamura, Y. Ota, K. Koike, Y. Hidaka, K. Nishioka, M. Sugiyama, K. Fujii, *Appl. Phys. Express* **2015**, *8*, 107101.
- [363] P. Zhai, S. Haussener, J. Ager, R. Sathre, K. Walczak, J. Greenblatt, T. McKone, *Energy Environ. Sci.* **2013**, *6*, 2380.
- [364] J. Newman, P. G. Hoertz, C. A. Bonino, J. A. Trainham, *J. Electrochem. Soc.* **2012**, *159*, A1722.
- [365] R. Sathre, J. B. Greenblatt, K. Walczak, I. D. Sharp, J. C. Stevens, J. W. Ager, F. A. Houle, *Energy Environ. Sci.* **2016**, *9*, 803.
- [366] A. Mills, S. Elouali, *J. Photochem. Photobiol. A* **2015**, *305*, 29.
- [367] O. Babacan, S. D. Causmaecker, A. Gambhir, M. Fajard, A. W. Rutherford, A. Fantuzzi, J. Nelson, *Nat. Energy* **2020**, *5*, 720.



Benjamin Moss is a postdoctoral research associate in the Durrant group at Imperial College London. He holds a B.Sc. in Chemistry (2014) from the University of Edinburgh, a MRes in Green Chemistry (2015), and a Ph.D. (2020) from Imperial College London. Ben's research focuses on *in situ* time resolved optical and X-ray studies of low-cost oxide and nitride materials for use in energy conversion technologies, in particular, solar fuel devices.



Oytun Babacan is a Research Fellow at the Grantham Institute, Imperial College London. He completed his graduate studies in Mechanical Engineering at the University of Illinois Urbana-Champaign (M.Sc., 2012) and the University of California San Diego (Ph.D., 2017). His research revolves around the integration of energy storage, electric vehicles, and renewables into urban and rural city infrastructures. He also investigates carbon mitigation pathways with a focus on energy and climate impacts of emerging technologies such as decarbonized liquid fuels.



Andreas Kafizas is a Lecturer (Assistant Professor) at the Grantham Institute, Imperial College London. Andreas completed his M.Sc. (2007) and Ph.D. (2011) in Chemistry at the University College London. Andreas now leads the Solar Coatings group, whose focus is to develop scalable synthetic routes to leading photocatalysts, and prototypes, for applications in solar fuels and environmental remediation.



Anna Hankin is a Lecturer (Assistant Professor) in the Department of Chemical Engineering at Imperial College London. Anna has a Master's degree in Physics (2007) and a Ph.D. in Electrochemical Engineering (2012) from the same university. She leads the Electrochemical Systems Laboratory, conducting research on the science and engineering of electrochemical energy conversion, solar fuel production, and a variety of separation processes for industrial effluent treatment and material recycling. Research strategies comprise experimental and modeling components to facilitate the eventual up-scale of electrochemical reactors.